Macromolecular and cytological changes in fission yeast G0 nuclei

Zhi Yang Tan[1†], Shujun Cai (蔡舒君)[1,2†], Saayli A. Paithankar[1], Xin Nie[1,3], Jian Shi[1] and Lu Gan (甘露)[1,*]

[1] Department of Biological Sciences and Centre for BioImaging Sciences, National University of Singapore, Singapore 117543
[2] Present address: School of Life Sciences, Southern University of Science and Technology, Nanshan, Shenzhen, Guangdong Province, China, 518055
[3] Present address: Thermo Fisher Scientific, The Capricorn, Singapore Science Park II, Singapore 117528

† Equal contribution
* Correspondence: lu@anaphase.org

Abbreviations

G0: the quiescent state
CTD-S2P: RNA polymerase II large-subunit C-terminal domain phospho-serine 2
CTD-S5P: RNA polymerase II large-subunit C-terminal domain phospho-serine 5
5-EU: 5-ethynyl-uridine
TSA: Trichostatin A
cryo-ET: electron cryotomography / cryo-electron tomography
Megacomplex: multi-megadalton globular complexes
Keywords: nucleus, chromatin, transcription, quiescence, yeast, cryo-ET

Running title

S. pombe G0 nucleus analysis

Summary

We use multiple cell-biological techniques to compare proliferating and quiescent G0 fission yeast cell nucleus transcription, histone acetylation, macromolecular packing.

ABSTRACT

When starved of nitrogen, fission yeast *Schizosaccharomyces pombe* cells enter a quiescent “G0” state with smaller nuclei and transcriptional repression. The genomics of *S. pombe* G0 cells has been well studied, but much of its nuclear cell biology remains unknown. Here we use confocal microscopy, immunoblots, and electron cryotomography to investigate the cytological, biochemical, and ultrastructural differences between *S. pombe* proliferating, G1-arrested, and G0 cell nuclei, with an emphasis on the histone acetylation, RNA polymerase II fates, and macromolecular complex packing. Compared to proliferating cells, G0 cells have lower levels of histone acetylation, nuclear RNA polymerase II, and active transcription. The G0 nucleus has similar macromolecular crowding yet fewer chromatin-associated multi-megadalton globular complexes. Induced histone hyperacetylation in G0 results in cells that have larger nuclei and therefore less compact chromatin. However, these histone-hyperacetylated G0 cells remain transcriptionally repressed with similar nuclear crowding. Canonical nucleosomes – those that resemble the crystal structure – are rare in proliferating, G1-arrested, and G0 cells. Our study therefore shows that extreme changes in nucleus physiology are possible without extreme reorganisation at the macromolecular level.

INTRODUCTION

Eukaryotic cells can adopt states that vary greatly in nuclear morphology and chromatin biochemistry and structure. Coordinated phenotypic changes in the nucleus are believed to regulate essential functions like transcription, replication, DNA repair, and stress response. The fission yeast *Schizosaccharomyces pombe* is an excellent model organism for nucleus cell biology because the cells can be enriched in different cell-cycle states, each with distinctive changes in chromosome compaction (Hiraoka et al., 1984; Nurse et al., 1976). When starved of nitrogen for 24 hours, *S. pombe* cells enter a non-dividing state called G0 quiescence (Su et al., 1996) (herein called G0) (**Figure 1A**). G0 cells are shorter and more thermotolerant than proliferating cells (Su et al., 1996). Furthermore, G0 cells have only ~30% of the mRNA and ~20% of the rRNA content of proliferating cells (Marguerat et al., 2012), suggesting that transcription is globally repressed.

Even though *S. pombe* G0 cells have been studied for nearly three decades, many of their cell-biological differences with proliferating cells are unknown; these differences include histone post-translational modifications (histone marks), RNA polymerase localisation and abundance, active-transcription status, and nuclear macromolecular packing. Chromatin is one of the most abundant nuclear components and it controls many of the cell's essential functions. The basic unit of chromatin is the nucleosome, consisting of approximately 147 bp of DNA wrapped around a histone octamer (Kornberg, 1974; Luger et al., 1997). Nucleosomes resemble ~10 nm wide, 6 nm thick

cylinders and are the most abundant macromolecular complexes in the nucleus. Biochemical factors like histone post-translational modifications control nucleosome packing, which may in turn either inhibit or enable the access of nuclear macromolecular machinery (Luger et al., 2012; Maeshima et al., 2019). Consistent with this idea, repressive and activating histone marks are associated with more compact and open chromatin, respectively (Maeshima et al., 2019; Oomen and Dekker, 2017).

Electron cryotomography (cryo-ET) is a popular form of cryo-EM used to study macromolecular complexes *in situ* in a life-like frozen-hydrated state (Bauerlein and Baumeister, 2021; Bohning and Bharat, 2021; Hylton and Swulius, 2021; Ng and Gan, 2020; Schur, 2019). In a cryo-ET experiment, cells are rapidly frozen, thinned, and then imaged in a way to produce a 3-D image called a cryotomogram. We previously used cryo-ET to study *S. pombe* mitotic chromosomes, which have less conspicuous chromatin compaction than what was seen by fluorescence microscopy: with no well-defined boundary between compacted chromatin and nucleoplasm because the nucleus is crowded with macromolecular complexes (Cai et al., 2018b). We also found that prometaphase cells have fewer chromatin-associated multi-megadalton globular complexes (herein called megacomplexes) than interphase cells. The open *in situ* chromatin organisation in *S. pombe* cell nuclei is consistent with mitotic transcription, indicated by the presence of conserved active RNA polymerase II post-translational markers.

In addition to nuclear macromolecular packing, nucleosome structure itself may have a role in transcriptional regulation *in situ*. Recently, we used cryo focused-ion beam (cryo-FIB) milled cellular cryolamellae samples, an energy-filtered electron-counting camera, and 3-D subtomogram classification to do a cryo-ET study of budding yeast *Saccharomyces cerevisiae* nucleosome structure *in situ*. We found that canonical nucleosomes (those that resemble the crystal structure) account for less than 10% of the expected total in *S. cerevisiae* nuclei (Tan et al., 2023). This result contrasts with our findings in human chromatin structure *in situ*, which has abundant and densely packed canonical nucleosomes in both interphase and mitotic cells (Cai et al., 2018a; Chen et al., 2023). Our previous analysis of *S. pombe* cryosections led us to conclude that these cells may not have abundant canonical nucleosomes; this hypothesis has not been rigorously tested using improved sample-preparation techniques (cryo-FIB-milled lamellae) and better cameras. The large differences between yeast and human chromatin could potentially be explained by large differences in transcription levels. Therefore, combined analysis of nucleus cytology, biochemistry, and ultrastructure may provide clues about how extremely different cell states are regulated.

Here we characterise *S. pombe* cell nuclei in multiple states: G1-arrested cells and proliferating cells as controls compared to G0 cells with and without hyperacetylated histones. To fill in several knowledge gaps about G0 nuclear cell biology, we analyse *S. pombe* using complementary methods: fluorescence microscopy, RNA labelling, immunoblots, and *in situ* cryo-ET. Our study correlates histone acetylation, thermotolerance, transcription, nucleus size, nuclear macromolecular packing, and

nucleosome structure. We find that G0 histones can be made hyperacetylated, which inhibits nucleus shrinkage, but does not affect thermotolerance or transcriptional repression. Furthermore, neither hypoacetylation nor hyperacetylation affect large-scale nuclear macromolecular packing or the abundance of canonical nucleosomes. Overall, we conclude that G0 transcriptional repression is robust to perturbations in histone acetylation and nuclear morphology and does not lead to a massive upregulation of canonical nucleosomes.

RESULTS

S. pombe strains and cell-cycle states

We have analysed how nuclear morphology, histone acetylation, transcription, and nuclear macromolecular complex distribution differ in proliferating and G0 *S. pombe* cells. This study therefore required cells of different strains, cell-cycle states, or combinations thereof (**Table S1)**. Strain MBY99 (herein called wild-type) was used as wild-type and for the generation of new strains that have eGFP fusions to genes at their endogenous loci (described later). Wild-type cells were used to generate asynchronous proliferative cells (herein called proliferating) and G0 cells both without and with hyperacetylated histones. Some experiments were done with the mutant strain *cdc10-129*, which arrests in G1 at elevated temperature. For nascent-RNA labelling experiments, we used the strain yFS240 (Sivakumar et al., 2004), which can incorporate exogenous uridine and its analogues (Hodson et al., 2003). For some cryo-ET controls, we used temperature-sensitive *cdc10-129* cells arrested in G1 phase (Aves et al., 1985) because G1 and G0 cells both have a 1N nuclear DNA content and cells enter G0 from a G1-like state (Mochida and Yanagida, 2006). We also used proliferating cells, which are mostly in G2, the longest cell-cycle phase (Forsburg, 1999). We did not use the strain *cdc10-129* for studies of G0 because when these cells were transferred to EMM−N, they did not have G0 phenotypes (see below).

Preparation of G0 and TSA-G0 cells

To prepare G0 *S. pombe* cells (**Figure 1A**), we starved proliferating cells of nitrogen by incubating them in Edinburgh Minimal Media without nitrogen (EMM−N) for 24 hours

(Costello et al., 1986; Su et al., 1996). G0 cells were prepared from wild-type (972 h-) cells, yFS240 cells, and new strains that express either an eGFP-tagged RNA polymerase II subunit or an eGFP-tagged nuclear pore subunit (details in later sections). To enable the study of histone-hyperacetylation effects, we prepared G0 cells by adding Trichostatin A (TSA) to the EMM−N. TSA is a histone-deacetylase inhibitor (Rundlett et al., 1996) that increases histone acetylation levels in proliferating *S. pombe* cells (Kimata et al., 2008) and induces chromatin decompaction *in situ* in human cells (Toth et al., 2004). To determine if TSA treatment affects G0 chromatin and if these changes depend on the timing of TSA treatment, we subjected *S. pombe* cells to two different regimens. In the TSA-G0 regimen, we incubated proliferating cells in EMM−N plus TSA for 24 hours. In the G0-TSA regimen, we first incubated proliferating cells in EMM−N for 24 hours, then we incubated the cells in EMM−N plus TSA for another 24 hours.

Differential interference contrast microscopy showed that following 24 hours of nitrogen starvation, wild-type G0 cells became shorter (**Figure 1B**) as reported earlier (Su et al., 1996), while fluorescence microscopy of DNA stained with 4′,6-diamidino-2-phenylindole (DAPI) showed that G0 chromosomes did not individualise like in prometaphase-arrested *nda3-KM311* cells (Hiraoka et al., 1984). TSA treatment leads to diverse cell morphologies depending on the genetic background. TSA-G0 wild-type cells were longer than G0 cells but shorter than proliferating cells. G0-TSA cells were shorter like untreated G0 cells (**Figure 1B**). Owing to their simpler preparation, most of our analyses of TSA-treated G0 cells were done with TSA-G0 cells, for which TSA

171 treatment and nitrogen starvation are concurrent during G0 entry. G0 and TSA-G0 cells
172 were less sensitive to 48°C heat stress than proliferating cells (**Figure 1C**), meaning
173 that TSA-treated G0 cells retain an important G0 phenotype. In contrast, *cdc10-129*
174 cells that were transferred to EMM−N were less resistant to heat shock than wild-type
175 G0 cells (**Figure 1D**). Other strains, including yFS240, an Rpb1-eGFP strain, and a
176 Nup97-eGFP strain were all resistant to heat shock and had cell-to-cell heterogeneity
177 after TSA-G0 treatment, with cells longer than TSA-G0 wild-type cells (details in the
178 relevant sections below). To keep the number of phenotypes manageable, we limited
179 the analysis of TSA-G0 treatment to wild-type cells.
180
181 **G0 chromatin is hypoacetylated, but can be reversibly hyperacetylated**
182 Histone marks are correlated with chromatin structure and function in yeasts (Millar and
183 Grunstein, 2006; Sinha et al., 2006) and has been characterised in only a few extreme
184 cell states. *S. cerevisiae* G0 cells has altered levels of several histone marks compared
185 to proliferating cells (McKnight et al., 2015; Mews et al., 2014) and also globally
186 repressed transcription (Allen et al., 2006; McKnight et al., 2015). Notably, *S. cerevisiae*
187 G0 cells have lower histone acetylation, which is correlated with oligonucleosome
188 condensation (Robinson et al., 2008; Shogren-Knaak et al., 2006; Tse et al., 1998). We
189 performed immunoblot analysis of *S. pombe* histone acetylation and found that
190 compared to proliferating and G1 cells, the G0 cells had lower levels of H3 acetylated at
191 multiple N-terminal lysines (H3-Ac), but not H4 acetylated at multiple N-terminal lysines
192 (H4-Ac) or at K16 (H4K16ac) (**Figure 2A**). TSA treatment with either the TSA-G0 or G0-
193 TSA regime induced hyperacetylation of H3-Ac, H4-Ac, and H4K16ac at levels equal to

or greater than in G0 and even greater than in G1 and proliferating cells. This TSA-induced G0 histone hyperacetylation was reversed after TSA washout from TSA-G0 cells (**Figure 2A**).

We next performed immunofluorescence to check if there is gross cell-to-cell variability i.e., if a subset of G0 cells had much-more histone acetylation than the others. We found that nearly all G0 cells had lower levels of H3-Ac than the typical proliferating cell (**Figure 2B**; compare short vs long cells in the +DMSO rows). In contrast, neither H4-Ac nor H4K16ac levels decreased noticeably in G0 cells (**Figure 2, C and D**; +DMSO rows). Both the immunoblot and immunofluorescence experiments showed that overall histone acetylation decreased in G0. In contrast, both immunoblots and immunofluorescence microscopy (**Figure 2, B – D**; +TSA rows) showed that both TSA-G0 and G0-TSA cells had equal or greater H3 and H4 acetylation than either untreated G0 cells or proliferating cells.

Transcription is repressed in G0 cells with and without histone hyperacetylation

An early study used RNA-seq to show that G0 cells have fewer transcripts than proliferating cells (Marguerat et al., 2012). To further assess the differences in transcription phenotypes between interphase and G0 cells, we analysed the abundance of RNA polymerase II, active RNA polymerase II, and newly synthesised RNA. In *S. pombe*, the *rpb1* gene encodes the largest subunit of the RNA polymerase II complex and exists as a single copy (Kimura et al., 1997). We tracked RNA polymerase II levels and localisation *in vivo* by creating a strain that has the *rpb1* gene tagged at its C-

terminus with eGFP (**Figure S1**). In confocal fluorescence micrographs of living cells, we found that both proliferating and G0 cells had bright Rpb1-eGFP nuclear signals (**Figure 3A**). RNA polymerase II levels are therefore unlikely to be downregulated in G0.

RNA polymerase II activity may also be controlled by interactions with other transcription machinery, resulting in detectable changes to this enzyme's post-translational state. So we next performed immunoblots against the Rpb1 subunit's carboxy-terminal domain (CTD) as well as two post-translational modifications of the Rpb1 CTD, serine 2 (CTD-S2P) and serine 5 (CTD-S5P) phosphorylation. The two phosphorylation marks are conserved markers for transcriptional elongation and transcription initiation respectively (Harlen and Churchman, 2017; Komarnitsky et al., 2000). Immunoblots that were calibrated using total H3 levels showed that G0 cells have less Rpb1 (consistent with the Rpb1-eGFP analysis), CTD-S2P, and CTD-S5P marks than proliferating cells, suggesting that RNA polymerase II initiation and elongation were decreased (**Figure 3B**). Immunoblots that were calibrated to equal CTD levels (using a pan-CTD antibody) showed that G0 cells also had similar levels of both CTD-S2P and CTD-S5P marks per Rpb1 subunit (**Figure 3C**). To characterise G0 RNA polymerase II activity in single cells, we performed immunofluorescence imaging to detect CTD-S2P. To keep the chromatin content comparable, we used *cdc10-129* cells arrested at G1 rather than asynchronous cells. We found that G0 cells had weaker CTD-S2P signals than G1 cells (**Figure 3D**). Therefore, Rpb1 is expressed at lower levels in G0 than in proliferating cells, yet the concentrations of this protein and activity of the enzyme to which it belongs are non-negligible in G0 cell nuclei.

To characterise bulk RNA synthesis in G0 cells, we fluorescently labelled new transcripts in the strain yFS240 (Sivakumar et al., 2004). Strains like yFS240 can incorporate exogenous uridine and its analogues into nascent RNA (Hodson et al., 2003). Newly synthesised RNA molecules that incorporate 5-ethynyl-uridine (5-EU) become detectable after ligation with a fluorescent dye like Alexa Fluor 488 (Jao and Salic, 2008). We therefore treated proliferating yFS240 cells with 5-EU to reveal new transcripts. For negative controls, we incubated wild-type cells with 5-EU, yFS240 cells with 5-EU plus the transcription inhibitor phenanthroline, and yFS240 cells with uridine. All 5-EU and uridine treatments were done for 10 minutes. The chromatin was stained with DAPI. Fluorescence microscopy showed nucleus-localised Alexa Fluor 488 signals above the background only in yFS240 cells that were incubated with 5-EU without transcription inhibitor; no signals were visible in the negative controls (**Figure S2**). In proliferating cells, the newly transcribed RNA appeared more abundant in the hemisphere opposite the DAPI signal (**Figure 3E**). This DAPI-poor (low DNA concentration) region is the *S. pombe* nucleolus (Tanaka and Kanbe, 1986), meaning that the strong 5-EU signal in this hemisphere came from newly synthesised rRNA (**Figure 3E** lower-left cell; and see the nucleolus analysis below). In comparison, 5-EU signal was much weaker in the DAPI-rich (chromatin) hemisphere of the nucleus, where most mRNA is synthesised. Such high levels of rRNA synthesis are consistent with the extremely high levels of ribosome biogenesis in yeasts (Warner, 1999). Compared to proliferating cells, G0 cells had very weak 5-EU signals (**Figure 3E**). To test if 10-minute incubations were too short for sufficient 5-EU-labelled RNA to accumulate in G0 cells,

we increased the 5-EU incorporation to 5 hours. The 5-EU-labelled RNA signal thereafter became detectable, albeit weak, in the G0 nucleus (**Figure 3F**). Furthermore, 5-EU was also present in the cytoplasm, possibly from the exported RNAs (**Figure 3F**).

Next, we tested the effect of TSA treatment on transcription in G0 cells. Like untreated G0 cells, TSA-G0 cells had weak CTD-S2P immunofluorescence signal (**Figure S3A**) and weak nuclear 5-EU signals (**Figure S3B**), meaning that transcription in G0 cells remained repressed even when the histones were hyperacetylated. TSA-G0 ‘s Rbp1-eGFP signal was similar to that of G0 cells and fainter than in proliferating cells (**Figure S3C**). Histone hyperacetylation therefore does not have large effects on either the intranuclear localisation or the concentrations of Rpb1 in G0. In summary, RNA transcription is repressed in G0 cells, even when the cells are forced to have histone marks that are associated with transcriptional activity.

S. pombe **cells do not undergo rapid transcriptional upregulation after G0 exit**

G0 is a reversible state, so G0 exit may reveal clues about the nuclear changes needed to de-repress genes. Many cell types exit G0 when nutrients are restored to the cell culture medium (Marescal and Cheeseman, 2020). Just minutes after G0 *S. cerevisiae* are switched into rich media, they undergo a state called “hypertranscription”, which is detectable as a large increase in transcription markers and nascent RNA (Cucinotta et al., 2021). This finding inspired us to characterise *S. pombe* transcription in G0 exit. We performed immunoblots against the total CTD levels (to account for total RNA polymerase II) and the transcription markers CTD-S2P and CTD-S5P on *S. pombe*

exiting G0, and found that compared to histone H3 levels (to calibrate for cell number), total CTD, CTD-S2P and CTD-S5P all remained low for 2 hours, increased at 4 hours, and continued increasing to the highest signal level at 6 hours **(Figure S4A)**. When we compared CTD-S2P and CTD-S5P to total CTD levels, neither CTD-S2P nor CTD-S5P levels increased substantially over 24 hours, with a very minor increase in CTD-S2P levels at 2 hours (**Figure S4B**). These results suggest that transcription in *S. pombe* does not increase as quickly as in *S. cerevisiae* during G0 exit.

To characterise *S. pombe* G0 exit in single cells, we imaged Rpb1 and the transcription markers by fluorescence microscopy. First, we performed live-cell fluorescence time-lapse imaging of G0 Rpb1-eGFP cells deposited on a YES agar pad, which verified that these cells were exiting G0, elongating, and undergoing nuclear division followed by cell division (**Figure S5A; Movie S1**). Since the growth conditions on an agar pad are different from liquid culture, we also analysed Rpb1-eGFP G0 cells suspended in liquid YES medium and collected freshly at different time points. Cells exiting G0 became visibly longer 2 hours after resuspension in rich medium and resembled proliferating cells within 24 hours. The Rpb1-eGFP signal had a very small fluorescence-intensity increase over 6 hours after the rich-media switch (**Figure S5B**). We then subjected yFS240 cells exiting G0 to 5-EU incorporation analysis. Nascent (albeit weak) nuclear RNA signals became visible above background starting at 6 hours after resuspension in rich media (**Figure S6**). In wild-type cells that were exiting G0, levels of the transcription-elongation marker CTD-S2P were weak until 6 hours after the rich-media switch (**Figure S7**). Cells exiting G0 showed weak immunofluorescence signals for the

transcription-initiation marker CTD-S5P until 4 hours after the rich-media switch (**Figure S8**) and weak CTD levels until 6 hours after the rich-media switch (**Figure S9**). These combined results indicate the *S. pombe* does not undergo hypertranscription during G0 exit and that transcription markers become non-negligible approximately when cell division restarts.

G0 nucleus shrinkage is inhibited by TSA treatment

A popular hypothesis of transcriptional regulation is that nuclear macromolecular crowding sterically inhibits the transcription machinery. TSA-treated G0 cells have repressed transcription despite their increased histone acetylation, raising the question: do TSA-G0 cells have less crowded nuclei? The confocal microscopy images above show hints that the larger TSA-G0 cells have bigger nuclei, whose spaciousness may allow for less macromolecular crowding. However, it is difficult to estimate nuclear volume using fluorescence microscopy of DAPI signals because the nuclear boundary is ambiguous. A better strategy is to image a strain that expresses a fluorescent nuclear-envelope protein, measure the nucleus diameter, and then calculate the nuclear volume (Heun et al., 2001; Neumann and Nurse, 2007; Varberg et al., 2022). We therefore created an *S. pombe* strain in the wild-type background in which the nuclear-pore protein Nup97 is tagged with eGFP at its endogenous locus (**Figure S10**). We did not use the *cdc10-129* background because live-cell imaging allows for the selection of G1 cells in a wild-type background – specifically, G1 cells are those that have just finished nucleokinesis. Fluorescence microscopy analysis of Nup97-eGFP-expressing G0 cells confirmed that their nuclei were smaller, with approximately half the nuclear

volume of G1 cells (mean volume of G1 nuclei = 5.2 μm^3, n = 52, and G0 nuclei = 2.8 μm^3, n = 114; $p < 0.0001$) (**Figure S11; Movie S2**). We also treated Nup97-eGFP-expressing cells with TSA either during or after entry into G0, then followed up with fluorescence microscopy (**Figure S12, A – C**). TSA-G0 cell nuclei had approximately twice the volume of G0 cell nuclei (mean volume of TSA-G0 nuclei = 5.7 μm^3, n = 90; $p < 0.0001$) (**Figure S12D**). In contrast, when the TSA was added to cells that have already entered G0, the resulting G0-TSA nuclei had ~30% more volume than G0 nuclei (G0-TSA nucleus mean volume = 3.7 μm^3, n = 138; $p < 0.0001$) (**Figure S12E**). These results show that nuclei are enlarged more due to TSA treatment while the cell is entering G0 than after it has already entered G0.

Cryo-ET analysis of *S. pombe* cells

To characterise the ultrastructural details of nuclei in proliferating, G1, G0 and TSA-G0 cells, we used cryo focused-ion-beam milling to prepare cellular cryolamellae (most of which were thinner than 150 nm) and then imaged them by cryo-ET. Defocus phase-contrast cryotomograms of nuclei in G1 and G0 cells revealed crowds of macromolecular complexes (**Figure S13, A and B**), which were previously not visible (Sajiki et al., 2009; Su et al., 1996). The contrast of the G0 nuclear densities in these cryotomograms was lower than in the G1 cells (**Figures S13, C and D**). This contrast difference is likely inherent in the sample and not due to sample preparation because the G0 cell lamella was thinner than the G1 cell lamella (~135 vs ~152 nm) and should therefore have the higher contrast expected of thinner samples. Subtomogram analysis of small complexes like nucleosomes is facilitated when the data are collected with a

Volta phase plate (VPP), which increases the low-resolution contrast (Asano et al., 2015; Fukuda et al., 2015; Tan et al., 2023). Therefore, the cryo-ET data reported below were collected with the VPP.

Canonical nucleosomes are rare in Proliferating, G1, G0 and TSA-G0 cells

Our previous attempts to identify canonical nucleosomes *in situ* in VPP cryotomograms of *S. pombe* cryosections did not reveal canonical class averages (Cai et al., 2018b). However, that study used cryosections, which may have sample-preparation-induced structural artefacts, and previous-generation electron detectors, which have lower signal-to-noise ratios (Ruskin et al., 2013). Because the *S. pombe* lysates did reveal canonical nucleosome class averages, we hypothesised that the nucleosomes in these cells may have partially detached DNA *in situ*. Our recent *in situ* study of wild-type *S. cerevisiae* (Tan et al., 2023), which used cryolamellae, a K3 detector, and a VPP, showed that canonical nucleosomes account for < 10% of the expected total, meaning that non-canonical nucleosomes (whose structures remain unknown) are the majority in budding yeast.

To characterise the prevalence of canonical nucleosomes of *S. pombe*, we performed VPP cryotomography of proliferating, G1, G0, and TSA-G0 cell cryolamellae (**Figures 4, S14 – S23**). We then used a workflow that involves template matching followed by 3D classification to attempt to identify and locate the canonical nucleosomes among the nucleosome-like particles (Tan et al., 2023). In this workflow, we minimised model bias by using a smooth cylindrical reference for both template matching and classification.

Canonical nucleosome class averages were not found *in situ* in proliferating, G1, or TSA-G0 *S. pombe* cell tomograms (**Figures S24, S25, S27**). Note that the absence of canonical nucleosome class averages in the other cell states reflects the rarity – but not the absence – of canonical nucleosomes. Only the G0 cell tomograms had a class average that vaguely resembles the canonical nucleosome (**Figures 5A, S26**). While the refined canonical nucleosome-like class average vaguely resembles the canonical nucleosome crystal structure (White et al., 2001), it has jagged features (**Figure 5, B and C**). These unusual density features suggest that 3-D classification could not resolve all the heterogeneity, meaning that canonical nucleosomes are also rare in G0 (less than ~4% of the expected population). Further advances in classification will be needed to improve the estimation of canonical-nucleosome structure abundance.

G1, G0 and TSA-G0 nuclei have similar macromolecular complex crowding

Our light-microscopy experiments above showed that G0 cells have smaller nuclei than both G1 (**Figure S11**) and TSA-G0 cells (**Figure S12**), even though they all have the same number of chromosomes. We thus expected that G0 cells would show denser nucleoplasmic particle packing than both G1 and TSA-G0 cells, which would reflect differences in chromatin compaction. Previously, we assumed that most nucleosomes were canonical (not detectable due to suspected technical limitations discussed above), so we had used nearest-neighbour density analysis of nucleosome-like particles to assess chromatin packing in nuclei (Cai et al., 2018b). Here our study rectifies both the sample-preparation and data-quality issues and now shows that non-canonical nucleosomes are the majority species *in situ*. Therefore, we cannot use nearest-

401 neighbour-distance analysis to study chromatin packing because we cannot yet identify
402 the non-canonical nucleosomes. Before nucleosome identification *in situ* in cryo-EM and
403 cryo-ET studies was feasible, Fourier analysis was used to characterise the packing
404 density of macromolecular complexes (Chen et al., 2016; Eltsov et al., 2008; Gan et al.,
405 2013; Scheffer et al., 2011). We therefore evaluated the overall packing of nuclear
406 complexes using radially averaged Fourier power spectra (herein power spectra), which
407 is less sensitive to the identities of the nuclear complexes.
408
409 The *S. pombe* nucleus has two major compartments – the nucleolus, which is the site of
410 ribosome biogenesis, and the region outside the nucleolus, which has more chromatin.
411 Nuclear megacomplexes include preribosomes, transcription initiation complexes,
412 spliceosomes, and many other globular complexes that exceed one megadalton
413 molecular weight. We first analysed cryolamella tomograms from the G1 cell cytoplasm
414 as a control (**Figure S14**). Power spectra from the ribosome-regions showed a broad
415 peak at approximately 30 nm spacing (**Figure 6A)**, which reflects the densely packed
416 ribosomes (25 – 28 nm) (Verschoor et al., 1998). To compare the crowding (average
417 centre-to-centre spacing) of all nuclear complexes, we performed Fourier analysis on
418 the G1 (**Figures S15 and S16**), proliferating (**Figures S17 and S18**), G0 (**Figure S19**
419 **and S20**) and TSA-G0 (**Figure S22 and S23**) nucleus cryotomograms. The power
420 spectra showed that the nuclei from all four cell types have a broad peak centred
421 around 20 nm (**Figure 6**). As such, proliferating, G1, G0 and TSA-G0 nuclei have
422 similar macromolecular crowding in the nucleoplasm. Furthermore, when the
423 nucleoplasm (**Figure S20**) and the nucleolus (**Figure S21**) in the same G0 nucleus

were compared, the power spectra were indistinguishable (**Figure S28**), meaning that these two nuclear subcompartments have similar crowdedness.

G0 and TSA-G0 chromatin has fewer megacomplexes than G1

S. pombe cells also undergo large nuclear changes when they enter mitosis. Compared to G2 (interphase) cells, prometaphase *S. pombe* cells have weaker (but still detectable) CTD-S2P signals, compacted chromosomes, and fewer megacomplexes in the chromatin (Cai et al., 2018b). These observations suggest a weak positive correlation between megacomplex abundance and transcription. To further explore the relationship between megacomplexes and transcription states, we sought to estimate the concentration of nucleoplasmic megacomplexes in G1, G0 and TSA-G0 cells. Since megacomplexes are too heterogeneous for 3D classification, we manually annotated globular particles larger than ~15 nm and found that megacomplexes were more abundant in G1 chromatin than in G0 chromatin (mean concentration of G1 = 665 megacomplexes per femtoliter, n = 5; mean concentration of G0 = 179 megacomplexes per femtoliter, n = 10; p = 0.0002) (**Figure 7A**). The G0 nucleoplasmic megacomplex concentration was similar to that of TSA-G0 (mean concentration of G0 = 179 megacomplexes per femtoliter, n = 10; mean concentration of TSA-G0 = 155 megacomplexes per femtoliter, n = 7, p = 0.57) (**Figure 7B**). Therefore, both TSA-G0 and G0 cells have lower concentrations of chromatin megacomplexes than G1 cells.

We next characterised the nucleolus, which can be immunofluorescently localised using the conserved marker fibrillarin (Tollervey et al., 1990). Fibrillarin immunofluorescence

images showed that G0 cells had smaller nucleoli than G1 cells (**Figure 8, A and B**), in line with previous traditional EM data (Su et al., 1996). Some G1 and G0 cryotomograms seemingly included a portion of the nucleolus (**Figure 8, C and D**), in which megacomplexes were more abundant than in the rest of the nucleus (**Figure 8, E – H**). The fact that transcription is repressed in the G0 nucleolus even though megacomplexes are abundant there indicates that megacomplex concentration and transcription may be positively correlated in proliferating cells and uncorrelated in G0 vs G1 cells.

DISCUSSION

When *S. pombe* cells enter G0, nearly every cell becomes shorter, undergoes transcriptional repression, and becomes more thermotolerant (Marguerat et al., 2012; Su et al., 1996). Several phenotype changes remained unknown, namely changes in histone acetylation, abundance of a key polymerase subunit, nucleus volume changes, distribution of nuclear macromolecular complexes, and structural state of the nucleosomes. Our study uses different microscopy and biochemistry techniques to fill in these knowledge gaps, giving a clearer picture of the cell-biological phenotypes of extreme cell states (**Figure 9**).

S. pombe G0 transcription repression shares some features with other extreme states

Transcriptional repression has been studied in a few extreme cell states. Early studies found that chromatin compaction is correlated with near-complete transcriptional shutdown during mitosis (Prescott and Bender, 1962; Taylor, 1960). While mitotic chromatin is believed to sterically exclude transcription machinery (Luger et al., 2012; Maeshima et al., 2019), later studies showed that compacted mammalian mitotic chromatin is accessible enough to be bound by a small amount of the transcription machinery and that low levels of transcription or and even upregulation of some genes (Chen et al., 2005; Hsiung et al., 2015; Liang et al., 2015; Palozola et al., 2017; Teves et al., 2018; Teves et al., 2016). In line with previous studies (Marguerat et al., 2012; Su et al., 1996), we demonstrate here that *S. pombe* cell nuclei have lower active transcription in the G0 state than in the proliferative state. Notably, the lower 5-EU

478 incorporation, lower RNA polymerase II levels, and lower levels of Rpb1 CTD-S2P and
479 CTD-S5P markers seen here are all consistent with transcriptional repression.
480
481 We previously found that mitotic *S. pombe* chromatin contains megacomplexes and
482 nucleosome-free “pockets”, indicating that the chromatin is unevenly packed (Cai et al.,
483 2018b). This nuclear phenotype is conducive to mitotic transcription (Oliva et al., 2005;
484 Peng et al., 2005; Rustici et al., 2004), which was supported by the observation of
485 active Rpb1 CTD-S2P marks in mitotic chromatin (Cai et al., 2018b). While G0
486 transcription is on average repressed, there are some genes that expressed at levels
487 similar to or greater than in proliferating cells (Marguerat et al., 2012; Shimanuki et al.,
488 2007). Here we find that some of the cytological and biochemical phenotypes observed
489 in mitotic *S. pombe* cells also hold for G0 cells. Megacomplexes are rarer within G0
490 chromatin, but abundant in the nucleolus. While the CTD-S2P signal is barely
491 detectable in immunofluorescence images, our immunoblots show that the levels of
492 CTD-S2P and CTD-S5P levels remain the same in G0 when calibrated to total Rpb1.
493 We also find that G0 cells have non-trivial levels of Rpb1-eGFP in the nucleus.
494 Therefore, *S. pombe* G0 cell nuclei also have properties conducive to low levels of
495 transcription.
496
497 When *S. cerevisiae* exits G0, it undergoes a process termed hypertranscription, i.e., a
498 large increase in transcription markers within minutes after G0 exit is triggered
499 (Cucinotta et al., 2021). In contrast, *S. pombe* nascent transcripts (assessed by 5-EU
500 incorporation) and RNA polymerase II activity (assessed by CTD-S2P and CTD-S5P

marks) remain low for several hours after G0 exit is triggered. Interestingly, *S. cerevisiae* and *S. pombe* require 4 hours (Cucinotta et al., 2021) and 6 to 7 hours (Su et al., 1996), respectively, to re-start proliferation. In both organisms, re-entry into the proliferative state takes approximately 2 – 3 times longer than the cell cycle. It remains to be determined what physiological features account for the difference in G0-exit transcription programs.

Histone hyperacetylation leads to complex phenotypes

Acetylation marks make chromatin more negatively charged and potentially change chromatin structure and function. For example, TSA treatment causes histone hyperacetylation and chromatin decompaction in both interphase HeLa (Toth et al., 2004) and G0 B cells (Kieffer-Kwon et al., 2017). In *S. cerevisiae* G0 cells, TSA treatment increases chromatin volume (Swygert et al., 2021) while deletion of the RPD3 lysine deacetylase gene (which also leads to increased histone acetylation) prevents transcriptional repression (McKnight et al., 2015). A recent study found that enzymes help control *S. pombe* G0 entry efficiency and survival (Zahedi et al., 2020). One may expect that perturbation of histone acetylation in *S. pombe* G0 cells may lead to large changes in cellular physiology. Compared to untreated G0 cells, TSA-treated G0 cells had hyperacetylated histone H3, longer cell bodies, and larger nuclei (similar volume to G1 nuclei). In contrast, TSA-induced histone hyperacetylation did not lead to a detectable decrease in thermotolerance or a derepression of transcription. Also, *S. pombe* TSA-G0 cell nuclei have similar macromolecular complex crowding as G0 cells, suggesting that the larger TSA-G0 nuclear volume may be packed with additional

524 complexes, whose identities are unknown. A counter-intuitive histone hyperacetylation
525 phenotype was also found in mitotic human fibroblasts (SK-N-SH cells), where TSA
526 treatment does not inhibit progression through mitosis and leaves chromosomes
527 compacted (Kruhlak et al., 2001). Changes in histone-acetylation therefore does not
528 lead to predictable phenotype differences in cells with repressed transcription.
529
530 **G0 chromatin does not undergo extreme local compaction**
531 In *S. cerevisiae*, the G0 nucleoplasm contains thicker STEM tomography densities than
532 in interphase nucleoplasm, suggesting that its G0 chromatin is more compact (Swygert
533 et al., 2021). Because *S. pombe* G0 nuclei have half the volume of G1 cells, we
534 expected that that the G0 nuclear contents would also show major rearrangements,
535 such as chromatin compacted into the domains in human perinuclear heterochromatin
536 or the chromatids in mitotic human cells (Cai et al., 2018a; Chen et al., 2023). However,
537 we did not see any regions in the G0 nuclei that resemble domains. Instead, our Fourier
538 analysis showed that proliferating, G1, G0, and TSA-G0 nuclei have a similar
539 crowdedness of macromolecular complexes, indicated by a single broad peak centred
540 at approximately 20 nm. A simple explanation of the similar cryo-ET power spectra
541 between different-sized nuclei is that the smaller G0 nuclei have fewer non-nucleosome
542 nuclear complexes. These studies show that transcriptional repression may be achieved
543 in diverse species and cell types that have different chromatin organisation.
544
545 **Canonical nucleosomes are rare in *S. pombe***

We recently found that in proliferating *S. cerevisiae*, less than 10% of the nucleosomes have the canonical structure (Tan et al., 2023). Here, we applied the same *in situ* 3-D classification analysis to *S. pombe* cryotomograms and found one class average in G0 chromatin that resembles the canonical nucleosome, accounting for <4% of the expected nucleosome population. This average had jagged density features, which suggests that misclassified complexes contributed heterogeneity that could not be removed by classification. Therefore, G0 canonical nucleosomes are likely rarer than 4%. No canonical nucleosome class averages were found in the proliferating, G1, and TSA-G0 cells, meaning that canonical nucleosomes are even rarer in these cell types. Note that these classification results mean that canonical nucleosomes are rare, not absent. The rarity of canonical nucleosomes is consistent with earlier findings that *S. pombe* nucleosomes have lower thermal stability and more flexible DNA ends than human nucleosomes *in vitro* (Koyama et al., 2017).

What intracellular factors result in the rarity of canonical nucleosomes inside *S. cerevisiae* and *S. pombe* cells? Canonical nucleosomes are rare in G0 cells even though all three RNA polymerases are repressed (Marguerat et al., 2012), meaning that transcriptional repression does not explain the rarity of canonical nucleosomes in *S. pombe*. Furthermore, the differences in histone acetylation levels in G0, G1, proliferating, and TSA-G0 cells, do not adequately account for the rarity of canonical nucleosomes *in situ*. Further comparative analysis of proliferating and G0 *S. pombe* cells may shortlist the factors that *do not* influence *in situ* canonical nucleosome abundance.

MATERIALS AND METHODS

Cell culture and synchronisation

Proliferating wild-type 972 h- cells (strain MBY99) were grown in Edinburgh Minimal Medium (EMM, USBio, Salem, MA) or in yeast extract with supplements (YES; 5 g/L^{-1} yeast extract, 30 g L^{-1} glucose, 75 mg L^{-1} histidine, 75 mg L^{-1} leucine, 75 mg L^{-1} adenine, 75 mg L^{-1} uracil) at 30°C (shaken at 200 – 250 RPM for all cell culture experiments) to OD_{600} = 0.2. Most cell washes were done by pelleting the cells by centrifugation, followed by resuspension in fresh growth media or buffer. To prepare G0 cells, proliferating cells were washed twice in EMM without nitrogen (EMM−N) and then incubated for 24 hours in EMM−N at 30°C. For experiments with *cdc10-129* (strain MBY165; *leu1-32*) cells, the cultures were grown in YES at 30°C. When the OD_{600} reached 0.2, the cultures were transferred to 36°C and incubated for 4 hours, which arrests the majority of cells in G1 phase. For G0 experiments, wild-type cells, yFS240 cells, or cells of strains that express either eGFP-tagged RNA polymerase II or eGFP-tagged nuclear pore subunits were used. *Cdc10-129* cells were not used for G0-cell analysis because after incubation in EMM−N (with leucine, which this strain requires for survival), they did not become shorter and were less thermotolerant than G0 cells of other strains. We suspect this phenotype is a consequence of the supplements, which may act as a sufficient source of nitrogen that prevents G0 entry.

TSA perturbation

591 TSA (T8552, Sigma, Merck KGaA, Darmstadt, Germany) was prepared as a 20 mg mL^{-1}
592 stock solution in dimethyl sulfoxide (DMSO). Cells growing in YES or EMM−N were
593 pelleted and then TSA was added following two different regimens. For G0-TSA,
594 proliferating cells were first incubated 24 hours in EMM−N, then 20 mg mL^{-1} TSA was
595 added to 20 µg mL^{-1} (66 µM) final concentration. These cells were then incubated in
596 TSA for 24 hours. For TSA-G0, proliferating cells were resuspended in EMM−N, then 20
597 mg mL^{-1} TSA was immediately added to 20 µg mL^{-1} final concentration. These cells
598 were incubated for 24 hours. For the washout control, TSA-G0 cells were washed with
599 fresh EMM−N, then incubated 24 hours before immunoblot processing.
600
601 **DAPI staining (not for immunofluorescence)**
602 For microscopy of DAPI-stained nuclei, cells were grown in EMM because the DAPI
603 signal is harder to see in YES-grown cells. Proliferating cells (0.5 OD_{600} units) were
604 concentrated by pelleting at 5,000 × g for 1 minute and then resuspended in 1 mL EMM.
605 G0 cell cultures started at OD_{600} = 0.2 and sometimes grew to OD_{600} > 0.5 after 24
606 hours of nitrogen starvation. These cultures were diluted to OD_{600} = 0.5 with EMM−N.
607 Cell cultures were fixed by adding 37% formaldehyde (#47608-1L-F, Sigma) to 3.7%
608 final concentration, incubated for 90 minutes (all fixation was done 200 – 250 RPM
609 shaking), then collected by centrifugation at 5,000 × g for 1 minute. Cells were then
610 washed twice in phosphate-buffered saline, pH 7.4 (PBS; Vivantis, Selangor Darul
611 Ehsan, Malaysia) and resuspended in 20 µL of PBS with 1 µg mL^{-1} DAPI for G0 cells
612 and 10 ng mL^{-1} DAPI for proliferating cells. To visualise the nuclei of G0 cells, they
613 needed to be treated with 100-fold higher DAPI concentrations than proliferating cells.

Five µl of this sample was then added to a microscope slide and imaged using an Olympus FV3000 Confocal Laser Scanning Microscope (Olympus, Tokyo, Japan) equipped with a 1.35 NA 60× oil-immersion objective lens. The confocal microscopy details are listed in **Table S2**.

Thermotolerance tests

Cells (OD_{600} range = 0.2 – 1.0 for proliferating, 0.7 for G0, and 0.5 for TSA-G0 – all at 0.01 OD_{600} units per sample) were pelleted at 5,000 × g for 1 minute. The cell pellets were resuspended in 100 µL of 30°C or 48°C YES or EMM−N medium (from 1 mL prewarmed stock) and then immediately placed in either a 30°C shaking incubator or a 48°C heating block, respectively, then incubated for 30 minutes. The 48°C-heated cells were then cooled on ice for 1 minute. Four serial dilutions (10×, 100×, 1,000×, 10,000×) were made for each sample into YES to 45 µL or 50 µL final total volume. The undiluted stock and diluted cultures (5 µL each) were spotted on a dry YES agar plate (2% w/v agar in YES medium). Once the cells were adsorbed onto the agar (~30 minutes), the plates were turned upside down, sealed with Parafilm®, incubated at 30°C for 2 days, and then photographed.

Immunoblots

Immunoblot samples were prepared using trichloroacetic acid (TCA) precipitation. The cell pellet (7 – 21 OD_{600} units, subsequently diluted to obtain equal protein loading) was resuspended in 200 µL of 20% TCA on ice. Approximately 0.4 g of glass beads (425 – 600 µm, Sigma) was added to the mixture. The cells were then vortexed for 1 minute,

637 followed by incubation on ice for 1 minute; this vortex-incubation treatment was done
638 four times in total. The cell lysate was then centrifuged at 2,000 × g for 10 seconds to
639 sediment the glass beads. Next, 500 µL ice-cold 5% TCA was mixed with the lysate.
640 The mixture (without glass beads) was transferred to a new tube. Another 500 µL of 5%
641 ice-cold TCA was mixed with the glass beads and this new mixture (without glass
642 beads) was added to the tube in the previous step. The combined mixture was then
643 placed on ice for 10 minutes to precipitate proteins. Then the precipitated proteins were
644 pelleted at 4°C, 15,000 × g for 20 minutes. The supernatant was removed and the pellet
645 was re-centrifuged (either short-spin for 3 seconds or 15,000 × g for 1 minute), followed
646 by the removal of the residual supernatant. The pellet was resuspended in 212 µL of 1×
647 Laemmli sample buffer, followed by the immediate addition of 26 µL of 1 M Tris pH 8 to
648 neutralise the residual TCA. Then the lysates were heated at 100°C for 5 minutes. The
649 lysates were then centrifuged at 15,000 × g for 10 minutes and the clarified supernatant
650 containing solubilized proteins was transferred to a new tube.
651
652 Protein loading levels were calibrated using immunoblots against both histone H3 and
653 H4 C-termini, or against Rpb1 C-terminal domain. SDS-PAGE was done with Mini-
654 PROTEAN® TGX™ 4-15% Precast Gels (Bio-Rad, Hercules, CA), electrophoresed for
655 90 minutes at 80 volts. Precision Plus Protein™ WesternC™ Standards (Bio-Rad) or
656 Invitrogen™ MagicMark™ XP Western Protein Standard (Thermo Fisher Scientific,
657 TFS, Waltham, MA) (2.5 µL) were loaded as molecular-weight markers. The proteins
658 were then transferred to PVDF membrane (Bio-Rad Immun-Blot®) at 100 volts for 30
659 minutes at 4°C. The membrane was blocked in 2% BSA in 1× Tris-Buffered Saline,

0.1% Tween® 20 Detergent (TBST) for 1 hour at 22°C and then incubated with primary antibody overnight at 22°C. All antibody dilution factors are reported in **Table S3**. Next, the blot was rinsed in TBST for 20 minutes three times at 22°C, and incubated with HRP-conjugated secondary antibody in 2% BSA in TBST for 1 hour at 22°C, with additional StrepTactin-HRP Conjugate (Bio-Rad) if Precision Plus Protein™ WesternC™ Standards ladder was used. The blot was then rinsed in TBST for 10 minutes three times. Finally, the blot was treated with a 50:50 mixture of Clarity Western Peroxide Reagent and Clarity Western Luminol/Enhancer Reagent (Bio-Rad) for 5 minutes before visualisation. The chemiluminescent signals were recorded using an ImageQuant LAS 4000 (Cytiva, Marlborough, MA). Uncropped immunoblots are shown in **Figure S29**.

Immunofluorescence microscopy

Indirect immunofluorescence microscopy was done using a modified version of our previous protocol (Cai et al., 2018b) as follows. Proliferating, G1, and G0 cells were fixed with 3.7% formaldehyde for 90 minutes at 30°C. Cells were collected by centrifugation at 5,000 × g for 5 minutes and were then resuspended in 1 mL PEM (100 mM PIPES, 1 mM EGTA, 1 mM $MgSO_4$, pH 6.9) buffer. The cells were then washed once by centrifugation and resuspension with PEM, followed by resuspension in 1 mL PEMS (1.2 M sorbitol in PEM). Next, the cells were converted to spheroplasts with 25 U/mL Zymolyase (Zymo Research, Irvine, CA) in PEMS and incubated for 75 minutes in a 37°C water bath. All subsequent incubations were done at 10 RPM in a rotator (Invitrogen HulaMixer™). The cells were washed again with PEMS, resuspended in

683 PEMS with 1% Triton X-100 (Sigma) and incubated at 22°C for 5 minutes. Cells were
684 then washed twice with PEM and then incubated in PEMBAL (PEM, 1% bovine serum
685 albumin (BSA), 100 mM l-lysine hydrochloride) for 1 hour at 22°C. The primary and
686 secondary antibodies used for immunostaining are listed, alongside the immunoblot
687 experimental parameters, in **Table S3**. The cells were resuspended in 100 µL of primary
688 antibody diluted in PEMBAL, incubated at 22°C overnight. Next, the cells were washed
689 twice with PEMBAL and resuspended in 100 µL of secondary antibody diluted in
690 PEMBAL, and then incubated at 22°C in the dark overnight. Finally, the cells were
691 washed in PEM, then PBS, then resuspended in 20 µL of DAPI diluted to 1 µg/mL in
692 PBS. Five µl of the sample was then added to a microscope slide and imaged using
693 either an Ultraview Vox spinning-disc confocal microscope (PerkinElmer, Waltham, MA)
694 or an Olympus FV3000 Confocal Laser Scanning Microscope. The images were
695 recorded using either a 60× or a 100× objective lens.
696
697 **Nascent RNA detection**
698 Newly synthesised RNA was detected *in situ* using a 5-EU click-chemistry kit ("Click-
699 iT™" C10329, Thermo Fisher Scientific (TFS), Waltham, MA). As a negative control, the
700 RNA-polymerase inhibitor phenanthroline (20 mg mL^{-1} stock in deionized water, P9375,
701 Sigma) was added to 1 mL cell culture to a final concentration of 350 µg/mL. Five-
702 ethynyl-uridine (100 mM stock in deionized water) was added to the cultures of strain
703 yFS240 or to strain MBY99 (the control strain) to 1 mM final concentration and
704 incubated at 30°C in the dark with shaking at 250 RPM for the various durations
705 indicated in the results. Cells were then fixed with 1 mL of 3.7% formaldehyde in PBS

for 15 minutes at 22°C; all subsequent incubations were done at 10 RPM in a rotator. Next, the cells were washed once by pelleting at 1,500 × g and resuspending in 1 mL of PBS. The cells were permeabilized with 1 mL of 0.5% Triton X-100 in PBS for 15 minutes at 22°C in the dark and then washed in PBS. Then the cells were treated with a reaction cocktail made with 428 µL of Click-iT RNA reaction buffer, 20 µL of 100 mM $CuSO_4$, 1.8 µL of Alexa Fluor® 488 stock solution and 50 µL of Click-iT reaction buffer additive as directed in the Click-iT RNA Alexa Fluor 488 Imaging Kit. This mixture was incubated at 22°C in the dark for 30 minutes. Finally, the labelled cells were washed in Click-iT reaction rinse buffer before they were resuspended in 20 µL of PBS with 1 µg/mL of DAPI.

Plasmid extraction and linearization

The plasmid pFA6a-link-yoEGFP-Kan was a gift from Wendell Lim & Kurt Thorn (Addgene plasmid # 44900 ; https://www.addgene.org/44900 ; RRID:Addgene_44900) (Lee et al., 2013), given in the form of a DH5-Alpha *Escherichia coli* bacterial stab. Five mL of bacteria were cultured in vent cap tubes shaking at 220 RPM at 37°C overnight, then plasmids were extracted with the QIAprep Spin Miniprep Kit (QIAGEN, Hilden, Germany) following the manufacturer's instructions.

Extracted plasmids were linearized by digestion with a reaction containing 1 µg of plasmid DNA, 5 µL of 10× rCutSmart™ Buffer (New England BioLabs, Ipswich, MA), 10 units of restriction enzyme (New England BioLabs) topped up to 50 µL with nuclease-free water. *Sal*I restriction enzyme was used for the template pFA6a-link-yoEGFP-Kan

729 plasmid, *Aat*II was used for confirmation of the Gibson Assembly product plasmid (see
730 below). The reaction mixture was heated at 37°C for 15 minutes to digest the DNA, then
731 80°C for 20 minutes to inactivate the enzymes.
732
733 **Strain construction**
734 The strain details are shown in **Table S1**. Primers were from IDT (Integrated DNA
735 Technologies, Inc., Singapore) and listed in **Table S4**. Q5 PCR Master Mix (New
736 England BioLabs) was used for PCR reactions. MBY99 served as the wild-type strain.
737 The insert and backbone fragments were amplified from pFA6a-link-yoEGFP-Kan
738 plasmids linearized with *Sal*I restriction enzyme. Homology fragments were amplified
739 from genomic DNA extracted from MBY99 with the DNeasy Blood & Tissue Kit
740 (QIAGEN) following the manufacturer's instructions. All PCR reactions contained 1 ng of
741 plasmid template DNA or 100 ng of genomic template DNA plus 0.5 µM of each primer.
742 The PCR program was 98°C for 30 seconds, then 30 cycles of 98°C for 5 seconds,
743 60°C for 10 seconds and 72°C for 1.5 minutes, then 72°C for 5 minutes.
744
745 For *rpb1-EGFP*, a plasmid containing the tagging cassette was created first by Gibson
746 Assembly (Gibson et al., 2009). The fragment containing 1kb of homology to the *rpb1*
747 gene sequence just before the stop codon (5' homology fragment), the EGFP-Kan
748 module fragment, the fragment containing 1kb of homology to the genomic sequence
749 just downstream of the *rpb1* stop codon (3' homology fragment), and the backbone
750 fragment were amplified as described above. For each fragment, the reverse primer
751 contained an overhang sequence matching the start of the next fragment. After their

amplification, the backbone and 5' homology fragments were combined by assembly PCR using the same PCR cycle as above, and the same was done with the EGFP-Kan module and 3' homology fragments. The resulting assembly PCR fragments were purified with the QIAquick PCR Purification Kit (QIAGEN), then assembled into plasmids and cloned into DH5-Alpha *E. coli* with the Gibson Assembly® Cloning Kit (NEB) following the manufacturer's instructions. The tagging cassette (5' homology, EGFP-Kan module, 3' homology) for transformation was then created by extracting the plasmids with the QIAprep Spin Miniprep Kit (QIAGEN) and linearizing the plasmids with *Aat*II restriction enzyme (New England BioLabs) using the digestion reaction as described above. The entire tagging cassette was then amplified using the same PCR cycle as above.

For *nup97-EGFP*, the tagging cassette was created directly through assembly PCR. The *nup97* 5' homology fragment, EGFP-Kan module fragment, and *nup97* 3' homology fragment were created as described above, each with the reverse primer containing an overhang sequence homologous to the start of the next fragment. All three fragments were then combined by assembly PCR using the same PCR cycle as above, and the resulting product was directly used for transformation.

Cells were transformed using the lithium acetate / PEG4000 method reported in (Murray et al., 2016) with modifications. Overnight cell culture in YES was diluted to OD_{600} = 0.2 in 25 mL of YES and grown to an OD_{600} of 0.5. Ten mL of cells were collected, centrifuged at 2,500 × g at 22°C for 5 minutes, and the supernatant was removed. The

775 cells were then washed with 5 mL sterile water with centrifugation at 2,500 × g at 22°C
776 for 3 minutes. The cells were resuspended in 1 mL sterile water, transferred to a new
777 1.5 mL collection tube, centrifuged at 16,000 × g at 22°C for 1 minute, washed in 1 mL
778 of TE/LiAc (10 mM tris, 1 mM ethylenediaminetetraacetic acid (EDTA), 100 mM lithium
779 acetate), with centrifugation at 16,000 × g for 1 minute, and resuspended in 100 µL of
780 the same buffer. One hundred µL of cell suspension was transferred to a new 1.5 mL
781 collection tube containing 10 µL of 2 mg mL^{-1} salmon sperm DNA (Sigma-Aldrich,
782 Burlington, MA) plus 5 µL of PCR-amplified cassette DNA, and incubated for at 22°C for
783 10 min. 260 µL of TE/LiAc/PEG (10 mM tris, 1 mM EDTA, 100 mM lithium acetate, 40%
784 w/v Polyethylene glycol 4000) was added and incubated with shaking at 22°C for 30
785 minutes. Forty-three µL of DMSO was added, the suspension was incubated at 42°C for
786 15 minutes in a water bath, then the suspension was centrifuged at 6,000 x g for 1
787 minute. The supernatant was removed, the cells were resuspended in 1 mL of EMM−N,
788 and the suspension was transferred to a vented-cap tube shaking at 220 RPM at 30°C
789 for 24 hours. Finally, the cells were transferred to a new 1.5 mL collection tube,
790 centrifuged at 16,000 × g for 1 minute, the medium was removed, and the cells were
791 resuspended in 300 µL of 1× TE buffer, pH 8.0 (10 mM tris, 1 mM EDTA). All this cell
792 suspension was plated on a G418 YES selection plate and incubated for several days
793 at 30°C. G418 selection plates were created by adding G418 to the molten YES agar to
794 a concentration of 200 mg L^{-1} before it was poured.
795
796 Newly created strains were authenticated by genomic DNA extraction with the DNeasy
797 Blood & Tissue Kit (QIAGEN) following the manufacturer's instructions, followed by

PCR of integration junctions and Sanger sequencing. Confirmation PCR was performed with a program of 94°C for 2 minutes, 30 cycles of 94°C for 1 minute, 62°C for 1 minute and 72°C for 3.5 minutes, then 72°C for 5 minutes. The PCR products were electrophoresed in a gel containing 2% agarose and FloroSafe DNA Stain in Tris-acetate-EDTA, at 100 Volts for 1 hour, then visualised in a G:Box (Syngene). For sequencing, overlapping PCR fragments were created with the above cycle, purified with the QIAquick PCR Purification Kit (QIAGEN) with water used for the final elution, before the fragments and the sequencing primers were sent for Sanger sequencing (Bio Basic Asia Pacific Pte Ltd, Singapore).

Analysis of cells exiting G0

Wild-type, yFS240, and Rpb1-eGFP cells were prepared as G0 cultures as described above. For the 0-minute G0 exit, 1 mL of wild-type cells was directly subjected to the immunofluorescence-microscopy procedure above; 1 mL of yFS240 cells was directly subjected to the nascent-RNA-detection procedure above; 1 mL of Rpb1-eGFP cells was directly imaged by confocal fluorescence microscopy; and 25 mL of wild-type cells was pelleted in preparation for the immunoblot procedure above, all without changing the culture medium. For 30 minute, 2 hour, 4 hour, and 6 hour G0 exit, either 1 mL or 25 mL of G0 cells was pelleted, then resuspended in an equal volume of YES and incubated for the respective duration at 30°C before being subjected to the above procedures. For the 24-hour G0 exit, either 50 µL of cells was inoculated in 5 mL of YES, then incubated 24 hours at 30°C before 1 mL of this culture was directly imaged or subjected to the immunofluorescence-microscopy or nascent-RNA-detection

821 procedures; or 250 µL of cells was inoculated in 25 mL of YES, then incubated 24 hours
822 at 30°C before all 25 mL of this culture was pelleted in preparation for the immunoblot
823 procedure. All RNA labelling with 5-EU was performed for 10 minutes so that, for
824 example, the “30 minute G0 exit” sample was first incubated for 30 minutes in YES,
825 then an additional 10 minutes in YES plus 5-EU, followed by fixation for treatment with
826 the Click-iT RNA Alexa Fluor 488 Imaging Kit.
827
828 **Fluorescence microscopy of living cells**
829 Cells were first grown to log phase (proliferating) or subjected to nitrogen starvation,
830 with TSA treatment when needed (G0 and TSA-G0). A thin pad agar made from 2% w/v
831 agar in YES (proliferating) or EMM−N (G0 and TSA-G0) medium was prepared and
832 spread on a glass slide before 5 µL of cell culture was applied to the coverslip and
833 pressed against the agar pad, which was trimmed to the size of the coverslip. Samples
834 were imaged with an Olympus FV3000 Confocal Laser Scanning Microscope using a
835 60× objective lens. Images were captured as Z-stacks thick enough to image the GFP
836 signals from all of the nuclei at each stage position. To capture the moment the nuclei
837 have just divided, time-lapse imaging was performed with intervals of 10 minutes for 3
838 hours for nucleus size measurement, and with intervals of 30 minutes for 19 hours for
839 G0 exit. These time-lapse data were captured by collecting Z-stacks with Z-drift
840 compensation at each interval. Time-lapse imaging was not performed on most G0 and
841 TSA-G0 cells for nucleus size measurement because time-lapse-imaging tests did not
842 detect any changes in nucleus morphology in these cells during the 3 hours of time-
843 lapse imaging.

844

845 **Nucleus volume measurement**

846 Z-stacks of Nup97-eGFP cells were analysed in FIJI (Schindelin et al., 2012). To
847 facilitate the estimation of nuclear volume, spherical nuclei were chosen for analysis;
848 elongated and irregularly shaped nuclei were excluded. For each nucleus in the Z-stack,
849 the Z-slice where the nucleus appears the largest was chosen. The oval selection tool
850 was used to select a circular area extending from the centre of the Nup97-eGFP (green
851 channel) signal from one end of the nucleus to the centre of the Nup97-eGFP signal on
852 the opposite end, after which the diameter of the circle was recorded. For proliferating
853 cells, a time-lapse Z-stack was analysed. Nuclei that had just divided were identified as
854 G1 nuclei for nucleus volume analysis as described above. After all nucleus diameters
855 were recorded, their volumes were calculated from the sphere volume formula $4/3 \times \pi \times$
856 $(\text{diameter} / 2)^3$.

857

858 **Cryo FIB milling**

859 Proliferating, G1-arrested, G0 and TSA-G0 cells were first plunge-frozen with a Vitrobot,
860 Mark IV (TFS) operated at the respective growth or arrest temperatures (37°C for G1-
861 arrested cells, 30°C for proliferating, G0 and TSA-G0 cells) with 100% relative humidity.
862 Cells were centrifuged at 5,000 × g, the supernatant was removed, then the cells were
863 resuspended in a small volume of the same medium such that the new OD_{600} was 2.5
864 for proliferating and G1-arrested cells, and 4.0 for G0 and TSA-G0 cells. Four µl of cells
865 at OD_{600} = 2.5 or 4.0 was pipetted onto the carbon side of an electron microscopy grid,
866 manually blotted from the other side of the grid with a filter paper (Whatman, Grade 1)

for 1 – 2 seconds, then plunged into 37% ethane/63% propane cooled by liquid nitrogen (Tivol et al., 2008).

Grids were milled with a FEI Helios dual-beam electron microscope following the protocol of Medeiros and Böck (Medeiros et al., 2018). The samples were inserted into the microscope at −158°C using a PolarPrep 2000 Cryo Transfer System (Quorum Technologies, Laughton, UK), then coated with organoplatinum with a gas injection system. The organoplatinum was warmed to 33.85°C and then “Flow” in the xT microscope control GUI was set to “Open” for 15 or 20 seconds, as in the “cold-deposition” method (Hayles et al., 2007). Cells were located on the grid, then milled to generate a 100 to 150 nm thick, 15 µm wide lamella near the centre of a cell, starting with 2.8 nA beam current rough milling, followed by 0.46 nA intermediate milling, and ending with 48 pA for the final polishing step.

Electron cryotomography

Tilt series of cryolamellae were collected on a Titan Krios (TFS) operated at 300 kV, and equipped with a VPP (TFS), a K3 direct detection camera (AMETEK, Berwyn, PA), and a Gatan imaging filter (AMETEK) operated in zero-loss mode with a slit width of 20 eV. Detailed imaging parameters for lamellae are shown in **Table S5**. Images were captured as super-resolution movie frames at a 1.7 Å pixel size, using SerialEM (Mastronarde, 2005). Movies were aligned with IMOD alignframes (Mastronarde, 1997). The tilt series were automatically coarse aligned using the IMOD program *Etomo* running in batch-tomography mode (Kremer et al., 1996; Mastronarde, 1997;

Mastronarde and Held, 2017). Tilt series alignment was done in eTomo by patch tracking.

Contrast-transfer function compensation was done for the few defocus phase-contrast images, but not for the VPP images. To suppress the high-spatial-frequency noise, the tilt series were binned 4 times and low-pass filtered with Etomo 2-D filter parameters μ = 0.35, and σ = 0.05 for a 6.8 Å pixel size. Cryotomograms were reconstructed by weighted back projection using the default Etomo parameters, then trimmed in 3-D to exclude features outside the field of interest. The additional details of each analysed tilt series are in **Table S6**.

Template matching

Template matching was done using the PEET package (Particle Estimation for Electron Tomography) (Heumann, 2023; Heumann et al., 2011; Nicastro et al., 2006). A rounded 5 nm radius, 6 nm thick cylinder was used as a template. This template was enclosed with a cylindrical mask of 6.1 nm height and 5.4 nm radius, smoothed by convolution with a Gaussian of standard deviation of 0.68 nm. A cubic search grid with a 11 nm spacing was generated with the PEET program *gridInit*. Because this grid extended into the cytoplasm, a nucleus-enclosing boundary model was created within the same grid model file. This boundary model was drawn along the nuclear envelope at the “top” and “bottom” of the cryotomogram. The search points outside the nucleus were excluded with the IMOD command:

```
clipmodel -bound 2 original.mod new.mod
```

Template-matching hits that were within 6 nm of each other were considered as duplicates. One of the duplicates was automatically removed.

Classification analysis of nucleosome-like particles

All scripts prefixed by ot_ are available at https://github.com/anaphaze/ot-tools. Classification was done with RELION 3.0 (REgularised LIkelihood OptimisatioN) (Kimanius et al., 2016; Zivanov et al., 2018), using the subtomogram-analysis routines (Bharat et al., 2015). The nucleosome-like particles' centres of mass were converted from a PEET .mod file to a text file with the IMOD program *model2point*. These positions were then read into RELION to extract subtomograms with a 24.4 nm box size.

Our previous studies showed that some canonical nucleosomes are lost during 2-D classification (Cai et al., 2018a; Tan et al., 2023), so we exclusively used direct 3-D classification here to maximise the number of detected canonical nucleosomes. A rounded 10 nm wide, 6 nm thick cylinder was used as a reference map, and a smooth cylinder of the same dimensions and a cosine-shaped edge was used as a reference mask, both created with *beditimg*, the latter with *relion_mask_create* used as well. All nucleosome-like particles identified in PEET were subjected to 3-D classification with 100 classes, an experimental image mask diameter of 120 Å, a resolution cutoff of 20 Å, and 4 translational search steps.

Fourier power spectrum analysis

Tomographic slices were generated from 18 central slices, then imported into FIJI (Schindelin et al., 2012). A 800 × 800 pixel box of a region of the tomographic slice of the chromatin inside the nucleus (to exclude the nucleolar densities) was selected, then the Fourier Transform was generated using the FFT tool. The Radial Profile Angle plugin (Carl, 2020) was used to generate the rotationally averaged (1-D) power spectrum. The data was analysed and plotted with Excel (Microsoft Inc., Redmond, WA): the x axis has units of inverse nanometers according to the formula 1 / (2 × 0.68 nm) × (radius in pixels) / 512, where 1 / (2 × 0.68 nm) is the Nyquist limited resolution for data that has a pixel size of 0.68 nm.

To compare the nuclear power spectra from different cell types, we first normalised each spectrum by calculating the average of all amplitude values in the spectrum up to a resolution cutoff of 5 nm, then dividing each amplitude value by this average. After normalisation, the power spectra of all analysed tomograms of a given sample type were averaged at each spacing to produce the mean. The error bars represent the standard deviation of the amplitude values at each spacing.

Megacomplex analysis

To facilitate megacomplex picking, cryotomograms were binned twofold in 3-D with the IMOD program *binvol*. Each cryotomogram was opened with the 3dmod *slicer* tool set to ~30 nm thick tomographic slices. Nuclear particles that were (1) larger than 15 nm and (2) outside the nucleolus were manually picked as “scattered” contour points.

To estimate the chromatin volume, a “closed” contour was drawn around the chromatin position at the central slice of the cryotomogram. The area within this contour was calculated using the IMOD command:

imodinfo -F model.mod

This method reports the contour’s “Cylinder Volume”, defined in this case as Area × pixel_size^3, with Area expressed in voxels and pixel_size expressed in nanometers. This area was then multiplied by the tomogram thickness (in voxels) to estimate the volume.

Data sharing

One proliferating cell, G1 cell, G0 cell and TSA-G0 cell lamella cryotomogram each has been deposited as EMDB entry EMD-0875. All the tilt series and cryotomograms presented in this paper were deposited as EMPIAR (Iudin et al., 2016) entry EMPIAR-10339. We focused our efforts on the highest-contrast cryo-ET data that contained nuclear positions, leaving a large number of tilt series unanalysed. These surplus tilt-series and many corresponding cryotomograms will be deposited with our yeast surplus-data (Gan et al., 2019) entry EMPIAR-10227.

Figure preparation and statistics

Image format interconversion and contrast adjustments were applied to the entire field of view using FIJI (Schindelin et al., 2012) or Adobe Photoshop (Adobe Systems, San Jose, CA). Student’s t-tests were done with Google sheets (Alphabet Inc., Mountain View, CA). Plots of the rotationally average power spectra were made with Excel

(Microsoft Inc., Redmond, WA). Gardner-Altman estimation statistics plots (Ho et al., 2019) were made with the Estimation Statistics website (Claridge-Chang and Assam, 2023).

Contributions and Notes

ZYT, SC - project design, experiments, analysis, writing; SAP, XN - project design, experiments; JS - training; LG - project design, experiments, analysis, writing, training.

The authors declare no conflicts of interest.

ACKNOWLEDGEMENTS

We thank the CBIS microscopy staff for support and training. We thank Mohan Balasubramanian for strains MBY99 (972 h-) and MBY165 (*cdc10-129*); Makoto Ohira and Nick Rhind for sharing and advising on the use of the TK-hENT strain yFS240; Duane Loh for advice on Fourier analysis; and Claris Chong and Jon Chen for comments. This work was supported by a Singapore Ministry of Education T2 MOE2019-T2-2-045 and a T1 R-154-000-B42-114 grant.

REFERENCES

Allen, C., Buttner, S., Aragon, A. D., Thomas, J. A., Meirelles, O., Jaetao, J. E., Benn, D., Ruby, S. W., Veenhuis, M., Madeo, F. and Werner-Washburne, M. (2006). Isolation of quiescent and nonquiescent cells from yeast stationary-phase cultures. *J Cell Biol* **174**, 89-100. doi:10.1083/jcb.200604072

Asano, S., Fukuda, Y., Beck, F., Aufderheide, A., Forster, F., Danev, R. and Baumeister, W. (2015). Proteasomes. A molecular census of 26S proteasomes in intact neurons. *Science* **347**, 439-42. doi:10.1126/science.1261197

Aves, S. J., Durkacz, B. W., Carr, A. and Nurse, P. (1985). Cloning, sequencing and transcriptional control of the Schizosaccharomyces pombe cdc10 'start' gene. *EMBO J* **4**, 457-63.

Bauerlein, F. J. B. and Baumeister, W. (2021). Towards Visual Proteomics at High Resolution. *J Mol Biol* **433**, 167187. doi:10.1016/j.jmb.2021.167187

Bharat, T. A., Russo, C. J., Lowe, J., Passmore, L. A. and Scheres, S. H. (2015). Advances in Single-Particle Electron Cryomicroscopy Structure Determination applied to Sub-tomogram Averaging. *Structure* **23**, 1743-53. doi:10.1016/j.str.2015.06.026

Bohning, J. and Bharat, T. A. M. (2021). Towards high-throughput in situ structural biology using electron cryotomography. *Prog Biophys Mol Biol* **160**, 97-103. doi:10.1016/j.pbiomolbio.2020.05.010

Cai, S., Böck, D., Pilhofer, M. and Gan, L. (2018a). The in situ structures of mono-, di-, and trinucleosomes in human heterochromatin. *Mol Biol Cell* **29**, 2450-2457. doi:10.1091/mbc.E18-05-0331

Cai, S., Chen, C., Tan, Z. Y., Huang, Y., Shi, J. and Gan, L. (2018b). Cryo-ET reveals the macromolecular reorganization of S. pombe mitotic chromosomes in vivo. *Proc Natl Acad Sci U S A* **115**, 10977-10982. doi:10.1073/pnas.1720476115

Carl, P. (2020). Radial Profile Extended, vol. 2023.

Chen, C., Lim, H. H., Shi, J., Tamura, S., Maeshima, K., Surana, U. and Gan, L. (2016). Budding yeast chromatin is dispersed in a crowded nucleoplasm in vivo. *Mol Biol Cell* **27**, 3357-3368. doi:10.1091/mbc.E16-07-0506

Chen, D., Dundr, M., Wang, C., Leung, A., Lamond, A., Misteli, T. and Huang, S. (2005). Condensed mitotic chromatin is accessible to transcription factors and chromatin structural proteins. *J Cell Biol* **168**, 41-54. doi:10.1083/jcb.200407182

Chen, J. K., Liu, T., Cai, S., Ruan, W., Ng, C. T., Shi, J., Surana, U. and Gan, L. (2023). Nanoscale analysis of human G1 and metaphase chromatin in situ. *bioRxiv*, 2023.07.31.551204. doi:10.1101/2023.07.31.551204

Claridge-Chang, A. and Assam, P. (2023). ESTIMATION STATISTICS, vol. 2023.

Costello, G., Rodgers, L. and Beach, D. (1986). Fission yeast enters the stationary phase G0 state from either mitotic G1 or G2. *Current genetics* **11**, 119-125.

Cucinotta, C. E., Dell, R. H., Braceros, K. C. and Tsukiyama, T. (2021). RSC primes the quiescent genome for hypertranscription upon cell-cycle re-entry. *Elife* **10**. doi:10.7554/eLife.67033

Eltsov, M., Maclellan, K. M., Maeshima, K., Frangakis, A. S. and Dubochet, J. (2008). Analysis of cryo-electron microscopy images does not support the existence of 30-nm chromatin fibers in mitotic chromosomes in situ. *Proc Natl Acad Sci U S A* **105**, 19732-7. doi:10.1073/pnas.0810057105

Forsburg, S. L. (1999). The best yeast? *Trends Genet* **15**, 340-4.

Fukuda, Y., Laugks, U., Lucic, V., Baumeister, W. and Danev, R. (2015). Electron cryotomography of vitrified cells with a Volta phase plate. *J Struct Biol* **190**, 143-54. doi:10.1016/j.jsb.2015.03.004

Gan, L., Ladinsky, M. S. and Jensen, G. J. (2013). Chromatin in a marine picoeukaryote is a disordered assemblage of nucleosomes. *Chromosoma* **122**, 377-86. doi:10.1007/s00412-013-0423-z

Gan, L., Ng, C. T., Chen, C. and Cai, S. (2019). A collection of yeast cellular electron cryotomography data. *Gigascience* **8**. doi:10.1093/gigascience/giz077

Gibson, D. G., Young, L., Chuang, R. Y., Venter, J. C., Hutchison, C. A., 3rd and Smith, H. O. (2009). Enzymatic assembly of DNA molecules up to several hundred kilobases. *Nat Methods* **6**, 343-5. doi:10.1038/nmeth.1318

Harlen, K. M. and Churchman, L. S. (2017). The code and beyond: transcription regulation by the RNA polymerase II carboxy-terminal domain. *Nat Rev Mol Cell Biol* **18**, 263-273. doi:10.1038/nrm.2017.10

Hayles, M. F., Stokes, D. J., Phifer, D. and Findlay, K. C. (2007). A technique for improved focused ion beam milling of cryo-prepared life science specimens. *J Microsc* **226**, 263-9. doi:10.1111/j.1365-2818.2007.01775.x

Heumann, J. M. (2023). PEET: University of Colorado Boulder.

Heumann, J. M., Hoenger, A. and Mastronarde, D. N. (2011). Clustering and variance maps for cryo-electron tomography using wedge-masked differences. *J Struct Biol* **175**, 288-99. doi:10.1016/j.jsb.2011.05.011

Heun, P., Laroche, T., Shimada, K., Furrer, P. and Gasser, S. M. (2001). Chromosome dynamics in the yeast interphase nucleus. *Science* **294**, 2181-6. doi:10.1126/science.1065366

Hiraoka, Y., Toda, T. and Yanagida, M. (1984). The NDA3 gene of fission yeast encodes beta-tubulin: a cold-sensitive nda3 mutation reversibly blocks spindle formation and chromosome movement in mitosis. *Cell* **39**, 349-58.

Ho, J., Tumkaya, T., Aryal, S., Choi, H. and Claridge-Chang, A. (2019). Moving beyond P values: data analysis with estimation graphics. *Nat Methods* **16**, 565-566. doi:10.1038/s41592-019-0470-3

Hodson, J. A., Bailis, J. M. and Forsburg, S. L. (2003). Efficient labeling of fission yeast Schizosaccharomyces pombe with thymidine and BUdR. *Nucleic Acids Res* **31**, e134.

Hsiung, C. C., Morrissey, C. S., Udugama, M., Frank, C. L., Keller, C. A., Baek, S., Giardine, B., Crawford, G. E., Sung, M. H., Hardison, R. C. and Blobel, G. A. (2015). Genome accessibility is widely preserved and locally modulated during mitosis. *Genome Res* **25**, 213-25. doi:10.1101/gr.180646.114

Hylton, R. K. and Swulius, M. T. (2021). Challenges and triumphs in cryo-electron tomography. *iScience* **24**, 102959. doi:10.1016/j.isci.2021.102959

Iudin, A., Korir, P. K., Salavert-Torres, J., Kleywegt, G. J. and Patwardhan, A. (2016). EMPIAR: a public archive for raw electron microscopy image data. *Nat Methods* **13**, 387-8. doi:10.1038/nmeth.3806

Jao, C. Y. and Salic, A. (2008). Exploring RNA transcription and turnover in vivo by using click chemistry. *Proc Natl Acad Sci U S A* **105**, 15779-84. doi:10.1073/pnas.0808480105

Kieffer-Kwon, K. R., Nimura, K., Rao, S. S. P., Xu, J., Jung, S., Pekowska, A., Dose, M., Stevens, E., Mathe, E., Dong, P. et al. (2017). Myc Regulates Chromatin Decompaction and Nuclear Architecture during B Cell Activation. *Mol Cell* **67**, 566-578 e10. doi:10.1016/j.molcel.2017.07.013

Kimanius, D., Forsberg, B. O., Scheres, S. H. and Lindahl, E. (2016). Accelerated cryo-EM structure determination with parallelisation using GPUs in RELION-2. *Elife* **5**. doi:10.7554/eLife.18722

Kimata, Y., Matsuyama, A., Nagao, K., Furuya, K., Obuse, C., Yoshida, M. and Yanagida, M. (2008). Diminishing HDACs by drugs or mutations promotes normal or abnormal sister chromatid separation by affecting APC/C and adherin. *J Cell Sci* **121**, 1107-18. doi:10.1242/jcs.024224

Kimura, M., Ishiguro, A. and Ishihama, A. (1997). RNA polymerase II subunits 2, 3, and 11 form a core subassembly with DNA binding activity. *J Biol Chem* **272**, 25851-5. doi:10.1074/jbc.272.41.25851

Komarnitsky, P., Cho, E. J. and Buratowski, S. (2000). Different phosphorylated forms of RNA polymerase II and associated mRNA processing factors during transcription. *Genes Dev* **14**, 2452-60.

Kornberg, R. D. (1974). Chromatin structure: a repeating unit of histones and DNA. *Science* **184**, 868-71. doi:10.1126/science.184.4139.868

Koyama, M., Nagakura, W., Tanaka, H., Kujirai, T., Chikashige, Y., Haraguchi, T., Hiraoka, Y. and Kurumizaka, H. (2017). In vitro reconstitution and biochemical analyses of the Schizosaccharomyces pombe nucleosome. *Biochem Biophys Res Commun* **482**, 896-901. doi:10.1016/j.bbrc.2016.11.130

Kremer, J. R., Mastronarde, D. N. and McIntosh, J. R. (1996). Computer visualization of three-dimensional image data using IMOD. *J Struct Biol* **116**, 71-6. doi:10.1006/jsbi.1996.0013

Kruhlak, M. J., Hendzel, M. J., Fischle, W., Bertos, N. R., Hameed, S., Yang, X. J., Verdin, E. and Bazett-Jones, D. P. (2001). Regulation of global acetylation in mitosis through loss of histone acetyltransferases and deacetylases from chromatin. *J Biol Chem* **276**, 38307-19. doi:10.1074/jbc.M100290200

Lee, S., Lim, W. A. and Thorn, K. S. (2013). Improved blue, green, and red fluorescent protein tagging vectors for S. cerevisiae. *PLoS One* **8**, e67902. doi:10.1371/journal.pone.0067902

Liang, K., Woodfin, A. R., Slaughter, B. D., Unruh, J. R., Box, A. C., Rickels, R. A., Gao, X., Haug, J. S., Jaspersen, S. L. and Shilatifard, A. (2015). Mitotic Transcriptional Activation: Clearance of Actively Engaged Pol II via Transcriptional Elongation Control in Mitosis. *Mol Cell* **60**, 435-45. doi:10.1016/j.molcel.2015.09.021

Luger, K., Dechassa, M. L. and Tremethick, D. J. (2012). New insights into nucleosome and chromatin structure: an ordered state or a disordered affair? *Nat Rev Mol Cell Biol* **13**, 436-47. doi:10.1038/nrm3382

Luger, K., Mader, A. W., Richmond, R. K., Sargent, D. F. and Richmond, T. J. (1997). Crystal structure of the nucleosome core particle at 2.8 A resolution. *Nature* **389**, 251-60. doi:10.1038/38444

Maeshima, K., Ide, S. and Babokhov, M. (2019). Dynamic chromatin organization without the 30-nm fiber. *Curr Opin Cell Biol* **58**, 95-104. doi:10.1016/j.ceb.2019.02.003

Marescal, O. and Cheeseman, I. M. (2020). Cellular Mechanisms and Regulation of Quiescence. *Dev Cell* **55**, 259-271. doi:10.1016/j.devcel.2020.09.029

Marguerat, S., Schmidt, A., Codlin, S., Chen, W., Aebersold, R. and Bahler, J. (2012). Quantitative analysis of fission yeast transcriptomes and proteomes in proliferating and quiescent cells. *Cell* **151**, 671-83. doi:10.1016/j.cell.2012.09.019

Mastronarde, D. N. (1997). Dual-axis tomography: an approach with alignment methods that preserve resolution. *J Struct Biol* **120**, 343-52. doi:10.1006/jsbi.1997.3919

Mastronarde, D. N. (2005). Automated electron microscope tomography using robust prediction of specimen movements. *J Struct Biol* **152**, 36-51. doi:10.1016/j.jsb.2005.07.007

Mastronarde, D. N. and Held, S. R. (2017). Automated tilt series alignment and tomographic reconstruction in IMOD. *J Struct Biol* **197**, 102-113. doi:10.1016/j.jsb.2016.07.011

McKnight, J. N., Boerma, J. W., Breeden, L. L. and Tsukiyama, T. (2015). Global Promoter Targeting of a Conserved Lysine Deacetylase for Transcriptional Shutoff during Quiescence Entry. *Mol Cell* **59**, 732-43. doi:10.1016/j.molcel.2015.07.014

Medeiros, J. M., Bock, D., Weiss, G. L., Kooger, R., Wepf, R. A. and Pilhofer, M. (2018). Robust workflow and instrumentation for cryo-focused ion beam milling of samples for electron cryotomography. *Ultramicroscopy* **190**, 1-11. doi:10.1016/j.ultramic.2018.04.002

Mews, P., Zee, B. M., Liu, S., Donahue, G., Garcia, B. A. and Berger, S. L. (2014). Histone methylation has dynamics distinct from those of histone acetylation in cell cycle reentry from quiescence. *Mol Cell Biol* **34**, 3968-80. doi:10.1128/MCB.00763-14

Millar, C. B. and Grunstein, M. (2006). Genome-wide patterns of histone modifications in yeast. *Nat Rev Mol Cell Biol* **7**, 657-66. doi:10.1038/nrm1986

Mochida, S. and Yanagida, M. (2006). Distinct modes of DNA damage response in S. pombe G0 and vegetative cells. *Genes Cells* **11**, 13-27. doi:10.1111/j.1365-2443.2005.00917.x

Murray, J. M., Watson, A. T. and Carr, A. M. (2016). Transformation of Schizosaccharomyces pombe: Lithium Acetate/ Dimethyl Sulfoxide Procedure. *Cold Spring Harb Protoc* **2016**, pdb prot090969. doi:10.1101/pdb.prot090969

Neumann, F. R. and Nurse, P. (2007). Nuclear size control in fission yeast. *J Cell Biol* **179**, 593-600. doi:10.1083/jcb.200708054

Ng, C. T. and Gan, L. (2020). Investigating eukaryotic cells with cryo-ET. *Mol Biol Cell* **31**, 87-100. doi:10.1091/mbc.E18-05-0329

Nicastro, D., Schwartz, C., Pierson, J., Gaudette, R., Porter, M. E. and McIntosh, J. R. (2006). The molecular architecture of axonemes revealed by cryoelectron tomography. *Science* **313**, 944-8. doi:10.1126/science.1128618

Nurse, P., Thuriaux, P. and Nasmyth, K. (1976). Genetic control of the cell division cycle in the fission yeast Schizosaccharomyces pombe. *Mol Gen Genet* **146**, 167-78.

Oliva, A., Rosebrock, A., Ferrezuelo, F., Pyne, S., Chen, H., Skiena, S., Futcher, B. and Leatherwood, J. (2005). The cell cycle-regulated genes of Schizosaccharomyces pombe. *PLoS Biol* **3**, e225. doi:10.1371/journal.pbio.0030225

Oomen, M. E. and Dekker, J. (2017). Epigenetic characteristics of the mitotic chromosome in 1D and 3D. *Crit Rev Biochem Mol Biol* **52**, 185-204. doi:10.1080/10409238.2017.1287160

Palozola, K. C., Donahue, G., Liu, H., Grant, G. R., Becker, J. S., Cote, A., Yu, H., Raj, A. and Zaret, K. S. (2017). Mitotic transcription and waves of gene reactivation during mitotic exit. *Science* **358**, 119-122. doi:10.1126/science.aal4671

Peng, X., Karuturi, R. K., Miller, L. D., Lin, K., Jia, Y., Kondu, P., Wang, L., Wong, L. S., Liu, E. T., Balasubramanian, M. K. and Liu, J. (2005). Identification of cell cycle-regulated genes in fission yeast. *Mol Biol Cell* **16**, 1026-42. doi:10.1091/mbc.E04-04-0299

Prescott, D. M. and Bender, M. A. (1962). Synthesis of RNA and protein during mitosis in mammalian tissue culture cells. *Exp Cell Res* **26**, 260-8.

Robinson, P. J., An, W., Routh, A., Martino, F., Chapman, L., Roeder, R. G. and Rhodes, D. (2008). 30 nm chromatin fibre decompaction requires both H4-K16 acetylation and linker histone eviction. *J Mol Biol* **381**, 816-25. doi:10.1016/j.jmb.2008.04.050

Rundlett, S. E., Carmen, A. A., Kobayashi, R., Bavykin, S., Turner, B. M. and Grunstein, M. (1996). HDA1 and RPD3 are members of distinct yeast histone deacetylase complexes that regulate silencing and transcription. *Proc Natl Acad Sci U S A* **93**, 14503-8.

Ruskin, A. I., Yu, Z. and Grigorieff, N. (2013). Quantitative characterization of electron detectors for transmission electron microscopy. *J Struct Biol* **184**, 385-93. doi:10.1016/j.jsb.2013.10.016

Rustici, G., Mata, J., Kivinen, K., Lio, P., Penkett, C. J., Burns, G., Hayles, J., Brazma, A., Nurse, P. and Bahler, J. (2004). Periodic gene expression program of the fission yeast cell cycle. *Nat Genet* **36**, 809-17. doi:10.1038/ng1377

Sajiki, K., Hatanaka, M., Nakamura, T., Takeda, K., Shimanuki, M., Yoshida, T., Hanyu, Y., Hayashi, T., Nakaseko, Y. and Yanagida, M. (2009). Genetic control of cellular quiescence in S. pombe. *J Cell Sci* **122**, 1418-29. doi:10.1242/jcs.046466

Scheffer, M. P., Eltsov, M. and Frangakis, A. S. (2011). Evidence for short-range helical order in the 30-nm chromatin fibers of erythrocyte nuclei. *Proc Natl Acad Sci U S A* **108**, 16992-7. doi:10.1073/pnas.1108268108

Schindelin, J., Arganda-Carreras, I., Frise, E., Kaynig, V., Longair, M., Pietzsch, T., Preibisch, S., Rueden, C., Saalfeld, S., Schmid, B. et al. (2012). Fiji: an open-source platform for biological-image analysis. *Nat Methods* **9**, 676-82. doi:10.1038/nmeth.2019

Schur, F. K. (2019). Toward high-resolution in situ structural biology with cryo-electron tomography and subtomogram averaging. *Curr Opin Struct Biol* **58**, 1-9. doi:10.1016/j.sbi.2019.03.018

Shimanuki, M., Chung, S. Y., Chikashige, Y., Kawasaki, Y., Uehara, L., Tsutsumi, C., Hatanaka, M., Hiraoka, Y., Nagao, K. and Yanagida, M. (2007). Two-step, extensive alterations in the transcriptome from G0 arrest to cell division in Schizosaccharomyces pombe. *Genes Cells* **12**, 677-92. doi:10.1111/j.1365-2443.2007.01079.x

Shogren-Knaak, M., Ishii, H., Sun, J. M., Pazin, M. J., Davie, J. R. and Peterson, C. L. (2006). Histone H4-K16 acetylation controls chromatin structure and protein interactions. *Science* **311**, 844-7. doi:10.1126/science.1124000

Sinha, I., Wiren, M. and Ekwall, K. (2006). Genome-wide patterns of histone modifications in fission yeast. *Chromosome Res* **14**, 95-105. doi:10.1007/s10577-005-1023-4

Sivakumar, S., Porter-Goff, M., Patel, P. K., Benoit, K. and Rhind, N. (2004). In vivo labeling of fission yeast DNA with thymidine and thymidine analogs. *Methods* **33**, 213-9. doi:10.1016/j.ymeth.2003.11.016

Su, S. S., Tanaka, Y., Samejima, I., Tanaka, K. and Yanagida, M. (1996). A nitrogen starvation-induced dormant G0 state in fission yeast: the establishment from uncommitted G1 state and its delay for return to proliferation. *J Cell Sci* **109 (Pt 6)**, 1347-57.

Swygert, S. G., Lin, D., Portillo-Ledesma, S., Lin, P. Y., Hunt, D. R., Kao, C. F., Schlick, T., Noble, W. S. and Tsukiyama, T. (2021). Local chromatin fiber folding represses transcription and loop extrusion in quiescent cells. *Elife* **10**. doi:10.7554/eLife.72062

Tan, Z. Y., Cai, S., Noble, A. J., Chen, J. K., Shi, J. and Gan, L. (2023). Heterogeneous non-canonical nucleosomes predominate in yeast cells in situ. *Elife* **12**. doi:10.7554/eLife.87672

Tanaka, K. and Kanbe, T. (1986). Mitosis in the fission yeast Schizosaccharomyces pombe as revealed by freeze-substitution electron microscopy. *J Cell Sci* **80**, 253-68.

Taylor, J. H. (1960). Nucleic acid synthesis in relation to the cell division cycle. *Ann N Y Acad Sci* **90**, 409-21.

Teves, S. S., An, L., Bhargava-Shah, A., Xie, L., Darzacq, X. and Tjian, R. (2018). A stable mode of bookmarking by TBP recruits RNA polymerase II to mitotic chromosomes. *Elife* **7**. doi:10.7554/eLife.35621

Teves, S. S., An, L., Hansen, A. S., Xie, L., Darzacq, X. and Tjian, R. (2016). A dynamic mode of mitotic bookmarking by transcription factors. *Elife* **5**. doi:10.7554/eLife.22280

Tivol, W. F., Briegel, A. and Jensen, G. J. (2008). An improved cryogen for plunge freezing. *Microsc Microanal* **14**, 375-9. doi:10.1017/S1431927608080781

Tollervey, D., Tessars, G. and Luhrmann, R. (1990). Immunoprecipitation distinguishes non-overlapping groups of snRNPs in Schizosaccharomyces pombe. *Nucleic Acids Res* **18**, 5207-12. doi:10.1093/nar/18.17.5207

Toth, K. F., Knoch, T. A., Wachsmuth, M., Frank-Stohr, M., Stohr, M., Bacher, C. P., Muller, G. and Rippe, K. (2004). Trichostatin A-induced histone acetylation causes decondensation of interphase chromatin. *J Cell Sci* **117**, 4277-87. doi:10.1242/jcs.01293

Tse, C., Sera, T., Wolffe, A. P. and Hansen, J. C. (1998). Disruption of higher-order folding by core histone acetylation dramatically enhances transcription of nucleosomal arrays by RNA polymerase III. *Mol Cell Biol* **18**, 4629-38.

Varberg, J. M., Unruh, J. R., Bestul, A. J., Khan, A. A. and Jaspersen, S. L. (2022). Quantitative analysis of nuclear pore complex organization in Schizosaccharomyces pombe. *Life Sci Alliance* **5**. doi:10.26508/lsa.202201423

Verschoor, A., Warner, J. R., Srivastava, S., Grassucci, R. A. and Frank, J. (1998). Three-dimensional structure of the yeast ribosome. *Nucleic Acids Res* **26**, 655-61. doi:10.1093/nar/26.2.655

Warner, J. R. (1999). The economics of ribosome biosynthesis in yeast. *Trends Biochem Sci* **24**, 437-40.

White, C. L., Suto, R. K. and Luger, K. (2001). Structure of the yeast nucleosome core particle reveals fundamental changes in internucleosome interactions. *EMBO J* **20**, 5207-18. doi:10.1093/emboj/20.18.5207

Zahedi, Y., Durand-Dubief, M. and Ekwall, K. (2020). High-Throughput Flow Cytometry Combined with Genetic Analysis Brings New Insights into the Understanding of Chromatin Regulation of Cellular Quiescence. *Int J Mol Sci* **21**. doi:10.3390/ijms21239022

Zivanov, J., Nakane, T., Forsberg, B. O., Kimanius, D., Hagen, W. J., Lindahl, E. and Scheres, S. H. (2018). New tools for automated high-resolution cryo-EM structure determination in RELION-3. *Elife* **7**. doi:10.7554/eLife.42166

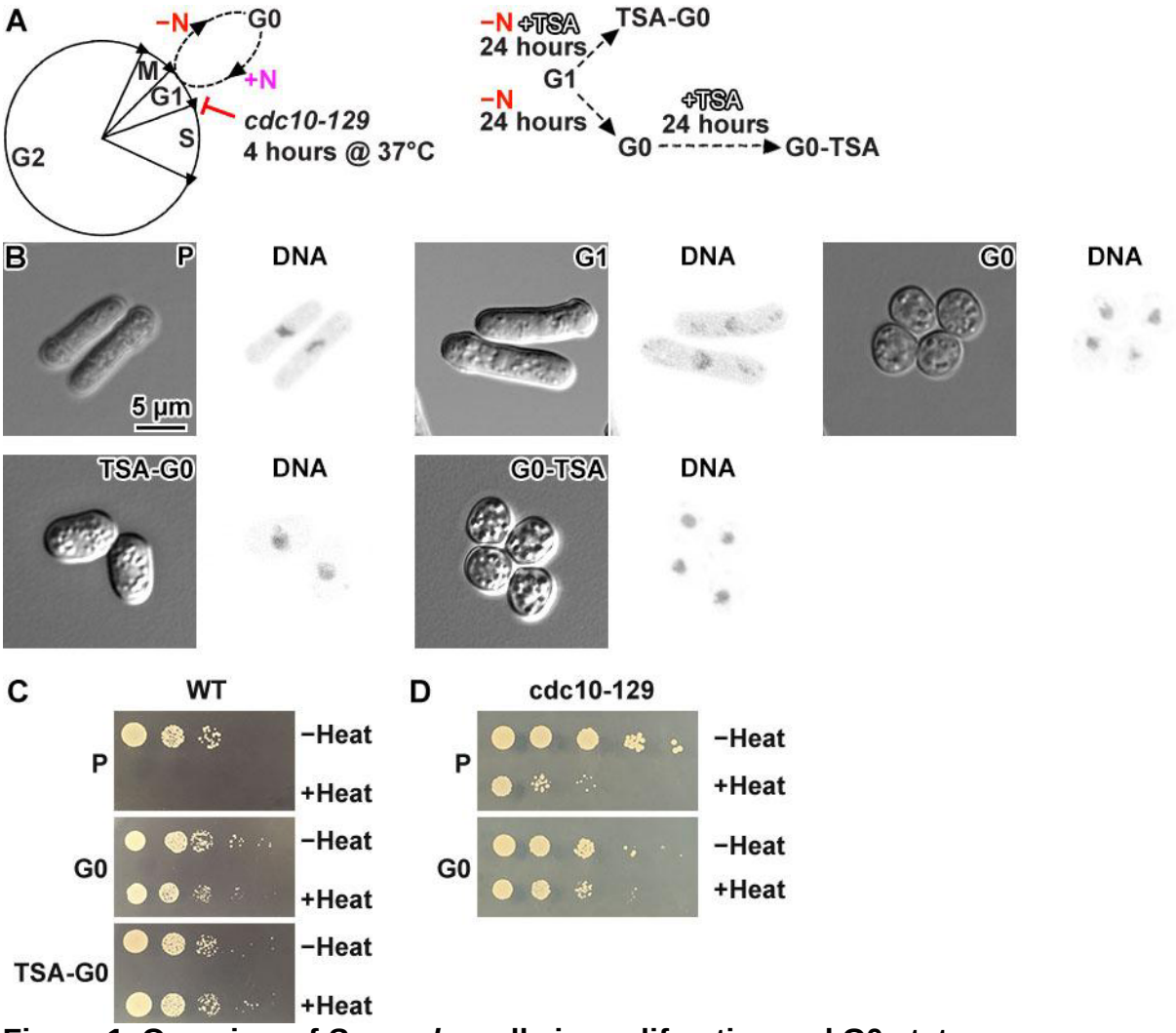

Figure 1. Overview of *S. pombe* cells in proliferative and G0 states

(A) Left: Schematic of the *S. pombe* cell cycle: G1 phase, S phase, G2 phase, and Mitosis (M). Entry to and exit from G0 is shown with the dashed line and depends on the availability of nitrogen (−N / +N). The *cdc10-129* strain arrests in G1 at 37°C. Right: Flowchart illustrating different regimes of TSA treatment. To generate TSA-G0 cells, cells are treated with TSA while they are being starved of nitrogen. To generate G0-TSA cells, G0 cells are treated with TSA. (B) Differential interference contrast (DIC, left) and fluorescence (right, DNA) images of DAPI-stained proliferating (P) cells (most in G2 phase), cells arrested at G1, G0 cells, TSA-treated cells – either treated while they were entering G0 (TSA-G0) or treated after they were already in G0 (G0-TSA). (C) Spot tests of proliferating, G0 and TSA-G0 wild type cells after a 30-minute incubation in their respective growth media (YES for proliferating, EMM−N for G0 and TSA-G0), with and without heat stress. (D) Spot tests of proliferating and G0 *cdc10-129* cells after a 30-minute incubation in their respective growth media (YES for proliferating, EMM−N for G0). The −Heat and +Heat conditions are, respectively, 30°C and 48°C.

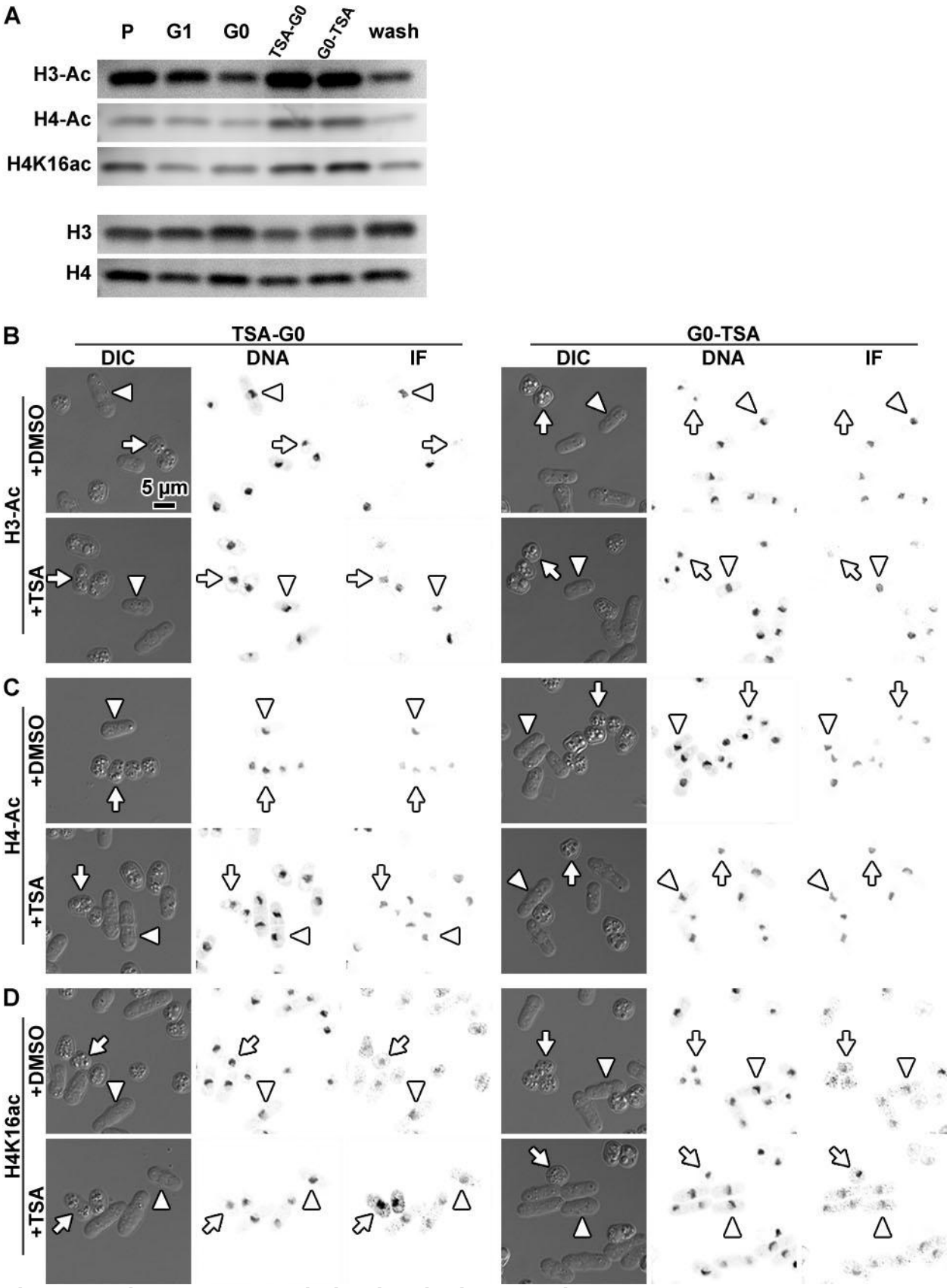

Figure 2. Histone H3 acetylation levels decrease in G0.

(A) Immunoblots of *S. pombe* lysates from wild-type proliferating (P), *cdc10-129* G1, and wild-type G0 cells. The G0 cells were either untreated (G0), incubated with TSA in EMM−N for 24 hours (TSA-G0), incubated 24 hours in EMM−N followed by 24 hours of EMM−N plus TSA (G0-TSA), or treated with EMM−N plus TSA for 24 hours followed by TSA washout and then incubated an additional 24 hours in EMM−N (wash). TSA was used at 20 µg/mL TSA final concentration, with DMSO as the carrier such that the final concentration of DMSO in the culture is 0.1%. Loading controls were done with antibodies against the H3 or H4 C-terminus. The uncropped immunoblots are shown in Figure S29. G0 cells were subjected to immunofluorescence imaging to detect (B) H3-Ac, (C) H4-Ac, and (D) H4K16ac. The G0 cells were treated with DMSO (+DMSO) or TSA (+TSA). “TSA-G0” and “G0-TSA” denote TSA treatment during or 24 hours after G0 entry, respectively, like in the immunoblot experiment. To ensure the cells were processed in similar conditions, the G0 and proliferating cells were first fixed separately, then mixed together for immunofluorescence processing. The proliferating cells serve as a common reference. In each subpanel, a representative G0 cell is indicated by an arrow and a representative proliferating cell is indicated by an arrowhead.

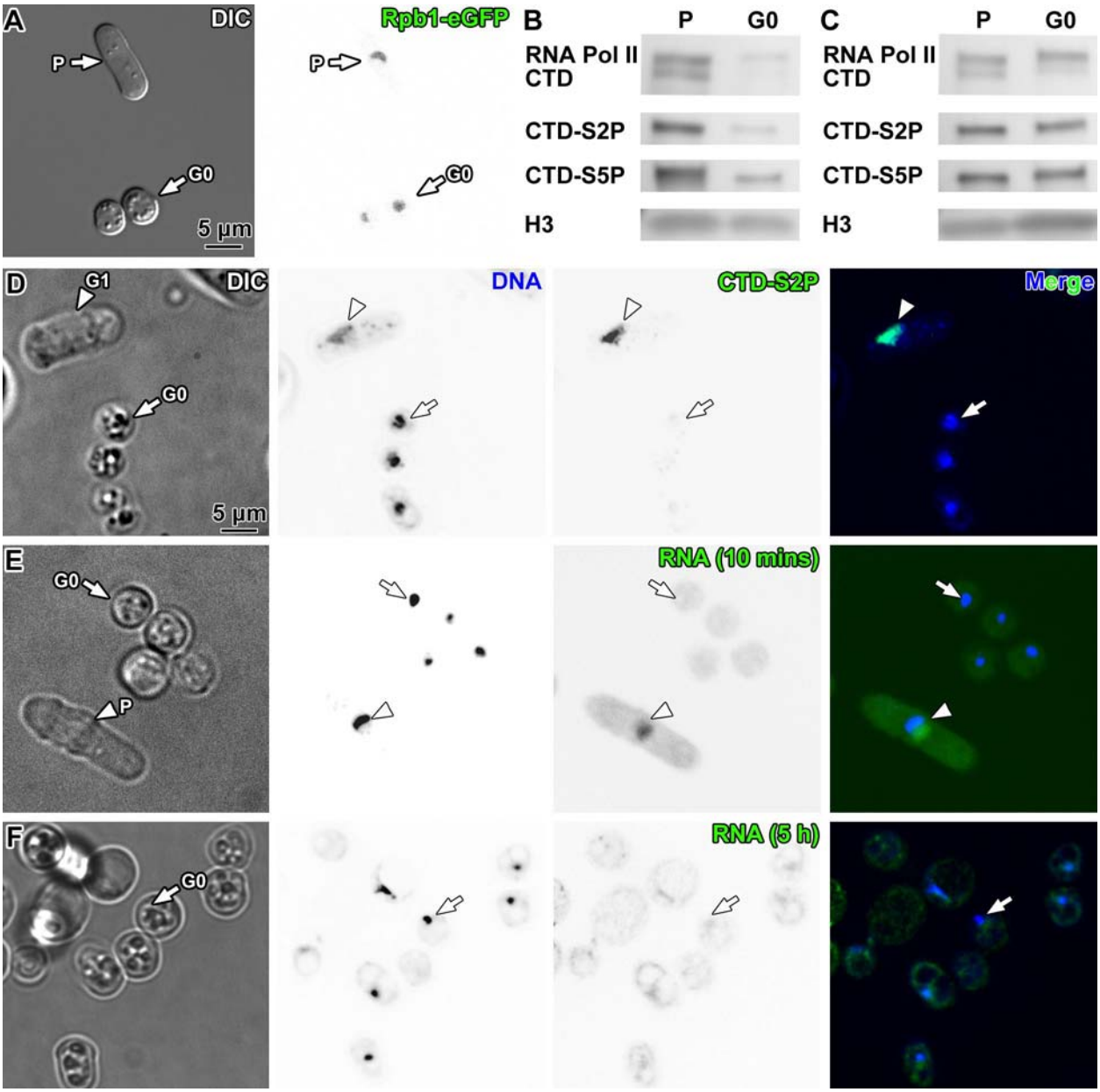

Figure 3. Transcription and RNAPII levels are lower in G0 cells.
Fluorescence microscopy analysis of transcription in interphase and G0 cells. (A) Differential interference contrast (DIC) (left) and eGFP (right) live-cell fluorescence microscopy images of Rpb1-eGFP in proliferating (P) and G0 states, in a strain where the *rpb1* gene is tagged with eGFP. Interphase cells were mixed into G0 cell culture just before imaging. A proliferating cell and a G0 cell are indicated. (B) Immunoblots of lysates from proliferating (P) and G0 wild type cells, using an α-CTD antibody, an α-CTD-S2P antibody and an α-CTD-S5P antibody. Loading controls were done with an antibody against the H3 C-terminus. (C) Immunoblots of the same lysates and antibodies as part B, with loading calibrated to have equal α-CTD signal. Uncropped immunoblots are shown in Figure S29. Columns, left to right for parts D-F: differential interference contrast (DIC), DAPI fluorescence (DNA), Alexa Fluor 488 fluorescence

(CTD, CTD-S2P, and RNA), and merge. (D) Detection of elongating RNA polymerase II with the anti-CTD-S2P antibody. One G1 cell is indicated by an arrowhead and a G0 cell by an arrow. (E) Strain yFS240 G0 and proliferating (P) cells were incubated with 5-EU and subjected to the Click-iT 5-EU-detection assay, which ligates Alexa Fluor 488 to 5-EU. A proliferating cell is indicated by an arrowhead and a G0 cell by an arrow. To increase the visibility of the weak 5-EU signal, the contrast was adjusted for the entire field of view, resulting in a higher apparent background. (F) G0 cells were incubated with 5-EU for 5 hours, then subjected to Click-iT 5-EU detection as in panel E. One G0 cell is indicated by an arrow. The two larger cells in the upper left are probably dead or dying as a result of prolonged 5-EU exposure.

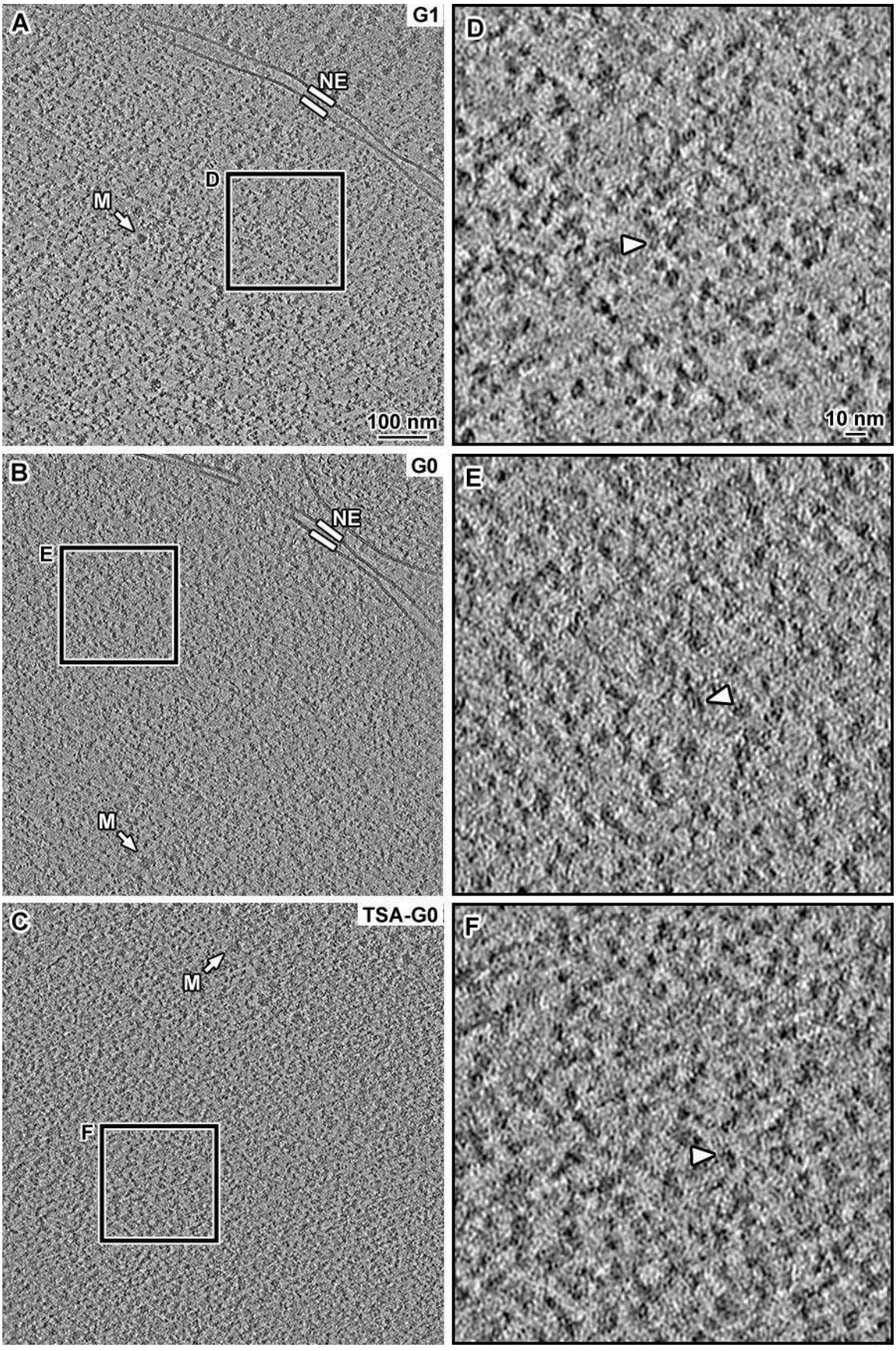

1321

Figure 4. G1, G0 and TSA-G0 cells have dense nucleoplasm.
(A) Volta cryotomographic slice (12 nm) of the nucleus in a G1-arrested *cdc10-129* cell. The nuclear envelope (NE) and a megacomplex (M) are indicated. (B) Volta cryotomographic slice (12 nm) of a nucleus in a wild-type G0 cell treated with 0.1% DMSO during G0 entry. The nuclear envelope (NE) and a megacomplex (M) are indicated. (C) Volta cryotomographic slice (12 nm) of the nucleus in a G0 cell treated with 20 µg/mL TSA during G0 entry. (D, E and F) Four-fold enlargements of the regions boxed in panels A, B and C, respectively. Nucleosome-like densities are indicated by arrowheads. Larger fields of view of G1, G0 and TSA-G0 nuclei are available in supplemental figures S15, S19 and S22 respectively.

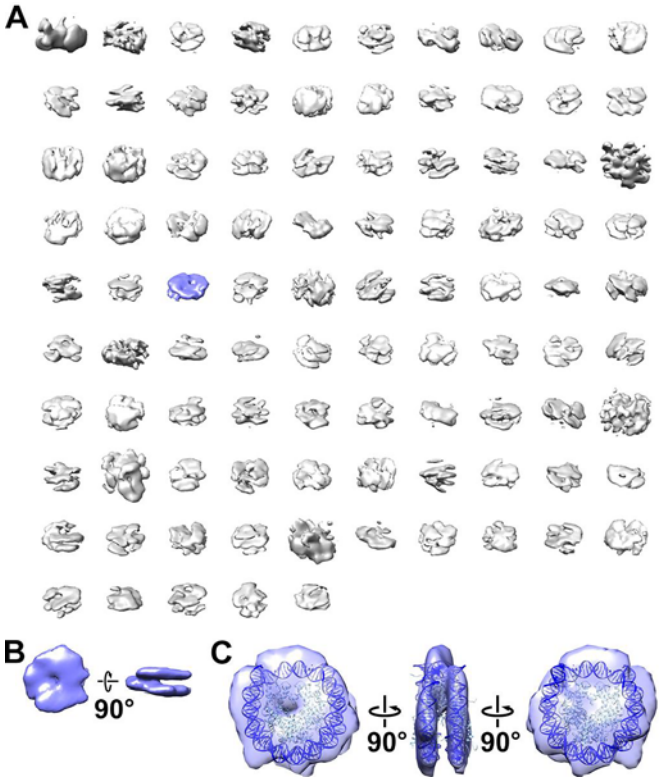

Figure 5. A class average that partially resembles the canonical nucleosome is detected in DMSO-G0 cells *in situ*.

(A) Class averages (3-D) of nucleosome-like particles in Volta phase plate (VPP) cryotomograms of DMSO-G0 cryolamellae. The class shaded blue partially resembles a canonical nucleosome. Five classes have no contributing particles. (B) Refined density of candidate nucleosomes observed in DMSO-G0 cryolamellae. (C) Refined density of the candidate G0 *S. pombe* nucleosome class with the crystal structure of the *Saccharomyces cerevisiae* nucleosome (PDB 1ID3) (White et al., 2001) docked. The histones and DNA are light and dark blue respectively. The *S. cerevisiae* nucleosome was used because the crystal structure of the *S. pombe* nucleosome has not been determined. For more details of the workflow, see Figure S26.

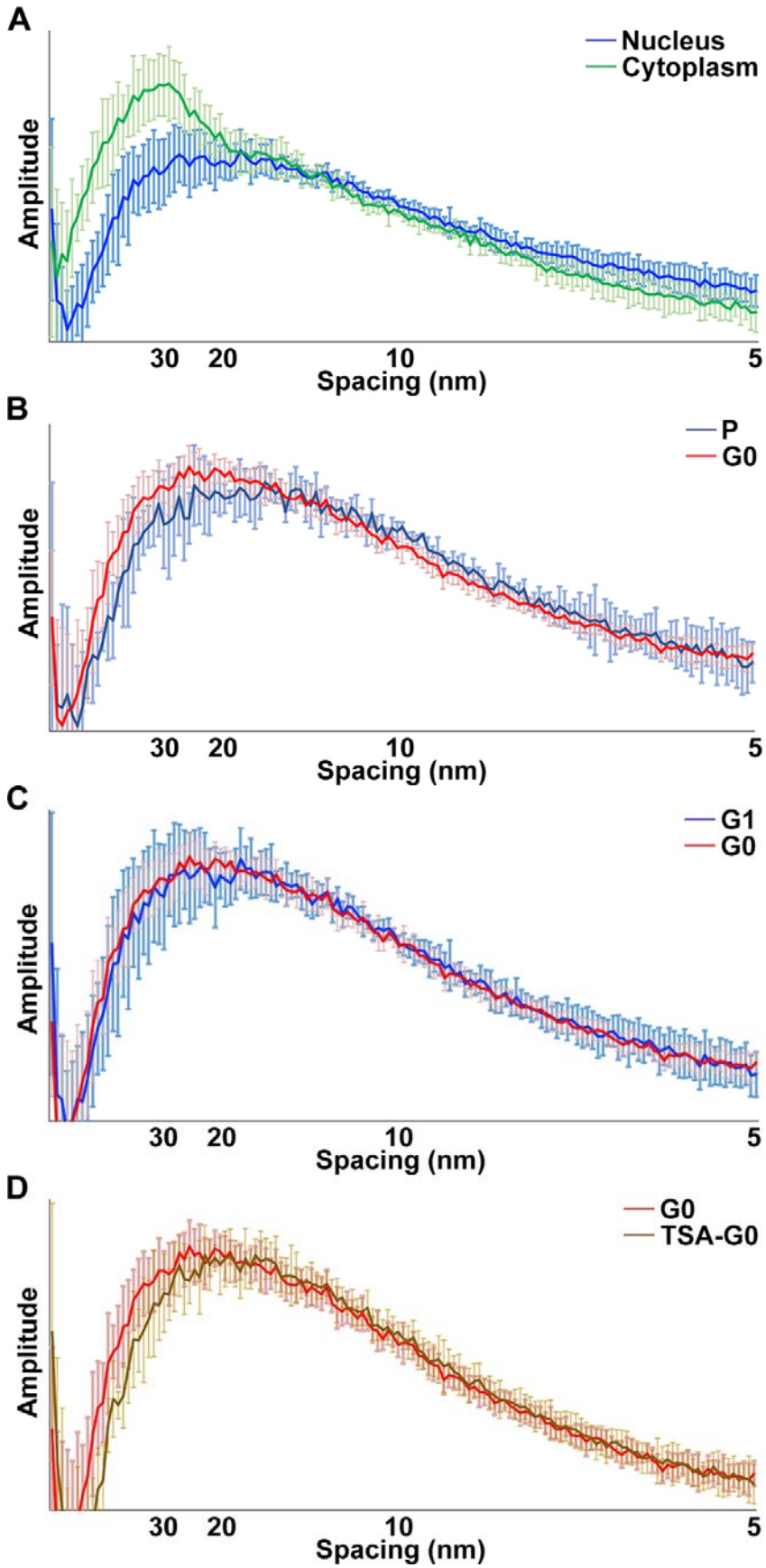

1344

Figure 6. *S. pombe* nuclei do not have large packing differences in various states. Average 1-D Fourier power spectra comparing (A) G1 nuclei (blue) and G1 cytoplasm (green); (B) proliferating (dark blue) and G0 (red) nuclei; (C) G1 (blue) and G0 (red) nuclei; (D) G0 (red) and TSA-G0 (brown) nuclei. For each spacing value, the normalised amplitudes are plotted; see Methods. Error bars indicate the standard deviation at each spacing.

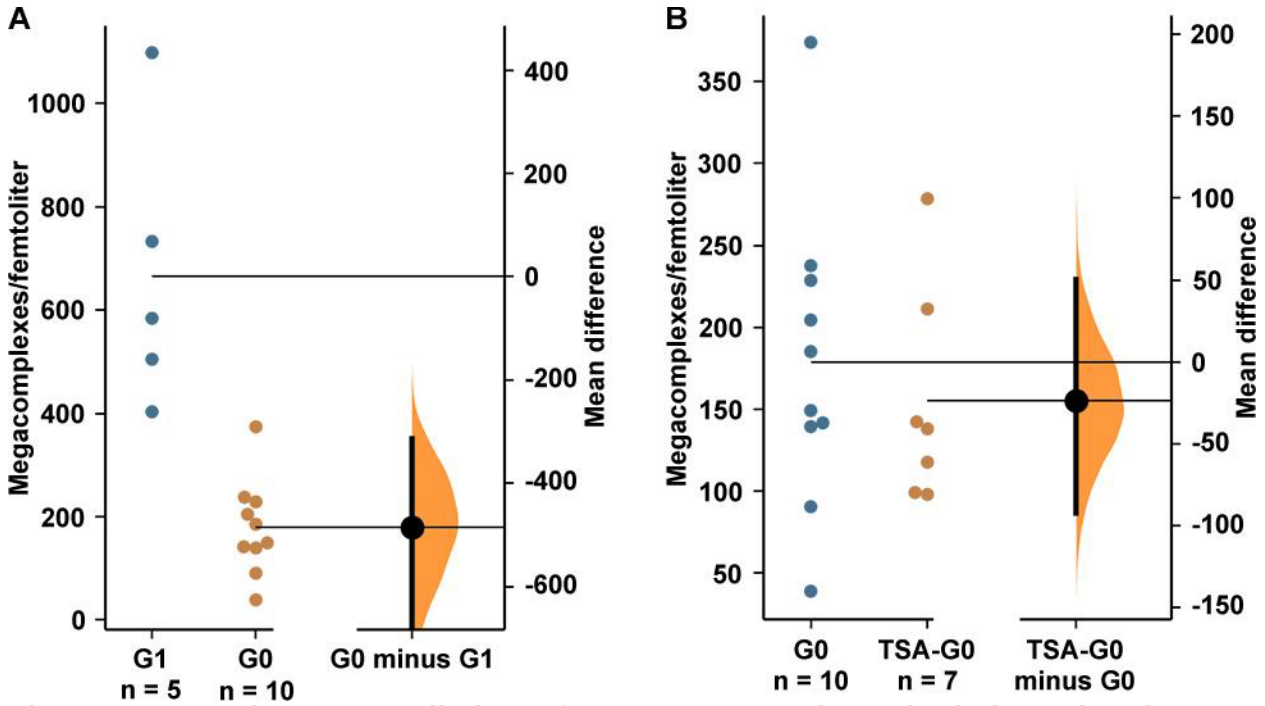

Figure 7. G0 and TSA-G0 cells have fewer megacomplexes in their nucleoplasm than G1.

Gardner-Altman plots of (A) the mean difference between G1 and G0 megacomplex concentrations in the nucleoplasm, and (B) the mean difference between G0 and TSA-G0 megacomplex concentrations in the nucleoplasm. In each plot, both groups of samples are plotted on the left axes; the mean difference is plotted on a floating axis on the right as a bootstrap sampling distribution. The mean difference is depicted as a dot; the 95% confidence interval is indicated by the ends of the vertical error bar (Ho et al., 2019).

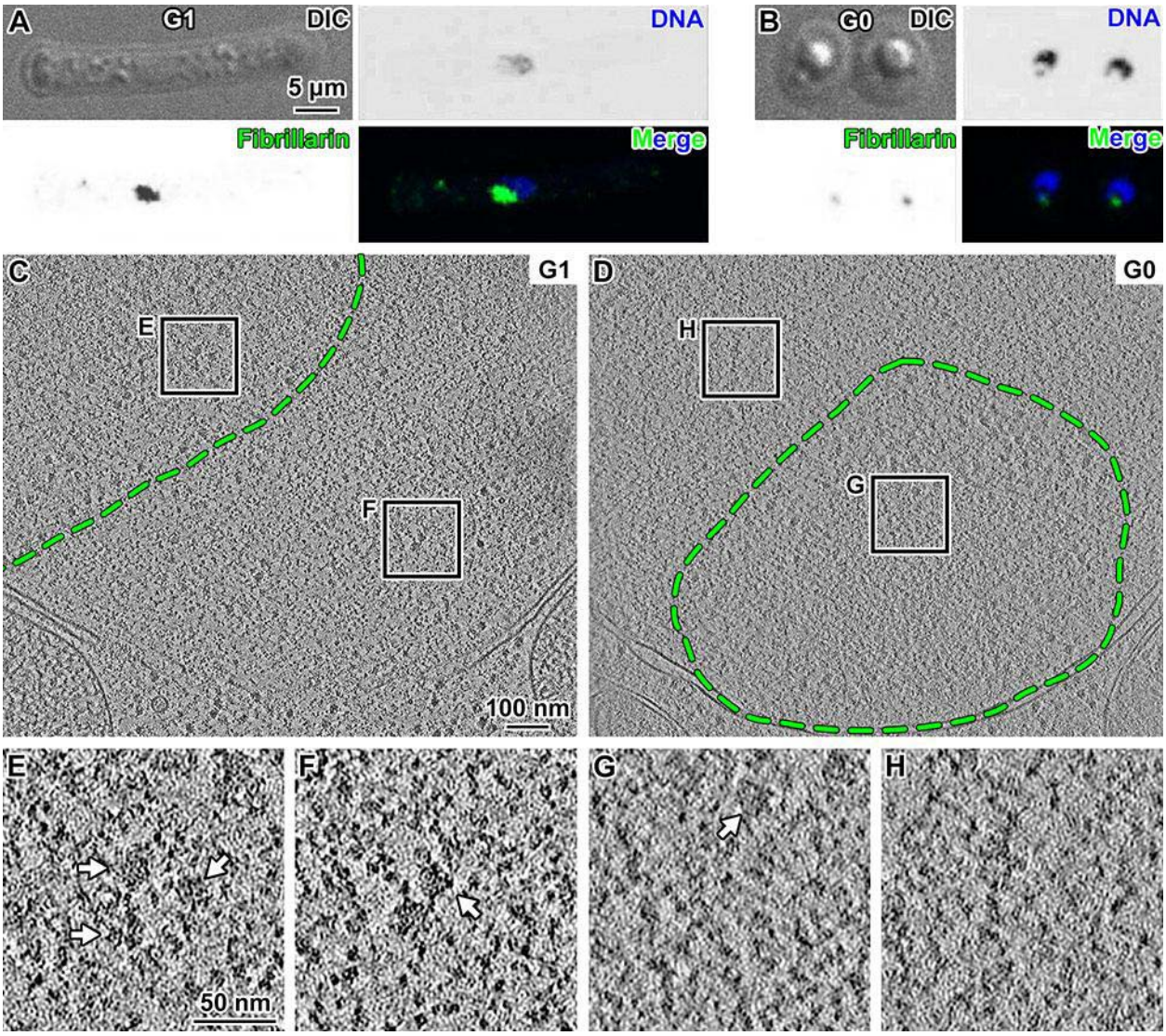

Figure 8. G0 nuclear megacomplexes are predominantly nucleolar.
(A and B) Immunofluorescence detection of nucleoli in G1 and G0 cells. DAPI (blue) marks DNA and anti-fibrillarin antibody (green) marks the nucleolus. It is unknown what the origin of the small gap between the G0 cells' fibrillarin and DNA signals is. (C and D) Volta cryotomographic slices (12 nm) of a G1 and a G0 cell, respectively. The region enclosed by the green dashed line denotes the approximate nucleolar boundary. (E and F) Four-fold enlargements of the G1 nucleolar and chromatin regions boxed in panel C. (G and H) Four-fold enlargements of the G0 nucleolar and chromatin regions boxed in panel G. Example megacomplexes are indicated by arrows in panels E, F, and G.

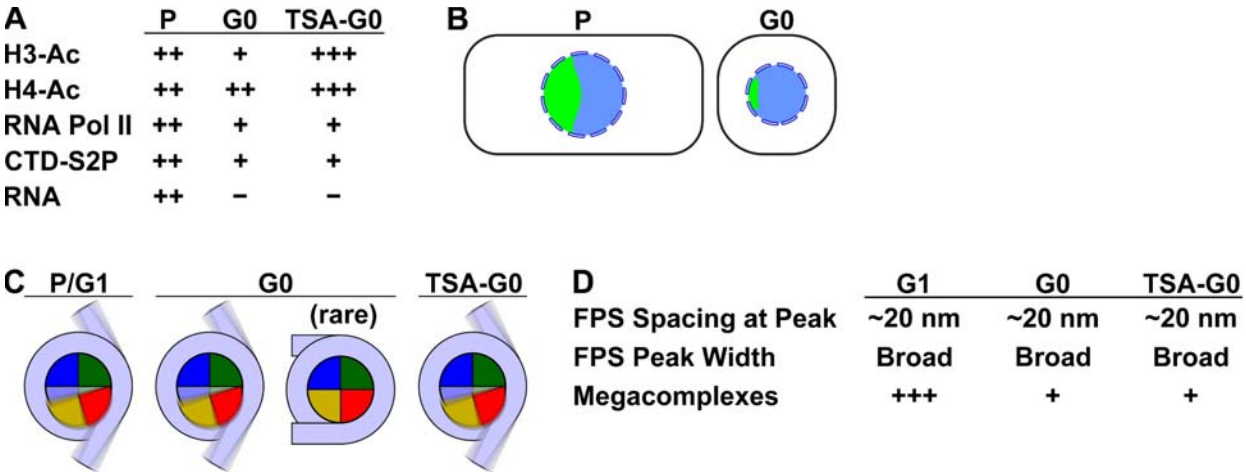

Figure 9: Summary of nuclear phenotypes in G0, G0-like, and proliferative cells. (A) Histone acetylation levels (H3-Ac and H4-Ac) are downregulated in G0 cells compared to proliferating (P) cells and upregulated in G0 cells treated with a histone-deacetylase inhibitor (TSA-G0). RNA Polymerase II levels and activity and transcription levels (RNA) are downregulated in G0 cells compared to proliferating cells and are uncorrelated with changes in G0 histone acetylation. (B) Cartoon of the cytological differences between proliferating (P) and G0 cells. Aside from having a smaller nucleus (blue circle), G0 cells have a disproportionately smaller nucleolus (green). (C) Schematics of DNA (light blue) and histones (shaded pie slices) in the nucleosome disc view. The cartoons only illustrate the 145 – 147 bp of "core" DNA. Majority of nucleosomes in G1, G0 and TSA-G0 are heterogeneous. The blurred appearance represents a large range of positions and orientations that protein and DNA components adopt inside cells, which would result in the absence of a class average resembling a canonical nucleosome; the blurring does not represent molecular motions. Nucleosomes with a structure resembling the canonical nucleosome are a minority conformation in G0, and even then, they have more unwrapped DNA than true canonical nucleosomes. (D) Fourier power spectrum (FPS) peak spacing and width are similar across G1, G0 and TSA-G0 cells. Megacomplex concentrations are higher in G1 cells than in G0 and TSA-G0 cells.

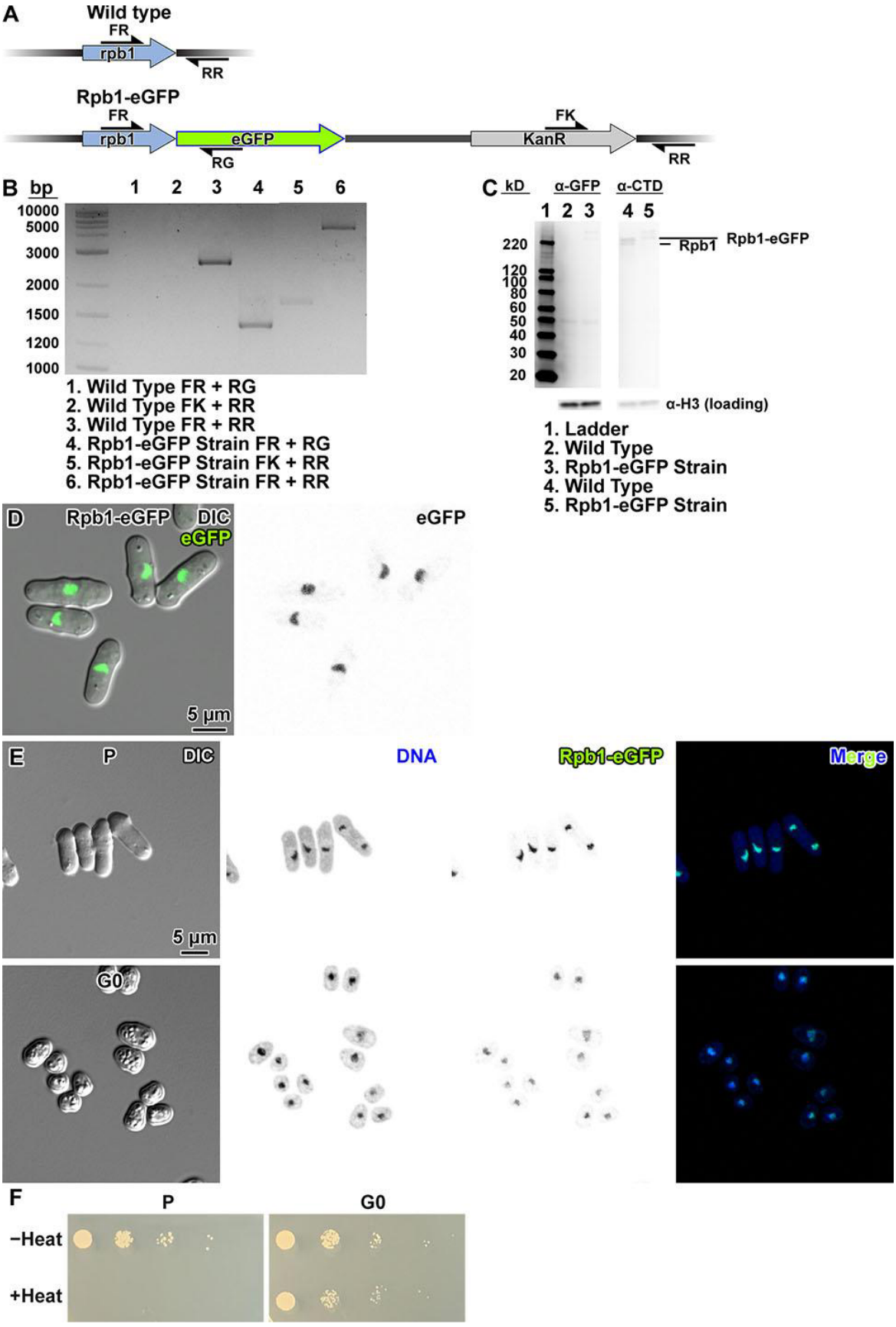

1392

Figure S1. Construction of Rpb1-eGFP strain.
(A) Map of the *rpb1* locus in the parent (wild-type) *S. pombe* strain MBY99 and the Rpb1-eGFP strain (LGSP0001). Primers used for PCR verification are indicated with the half arrow symbols. (B) Agarose gel of PCR amplicons expected from wild-type (control) and from Rpb1-eGFP genomic DNA, in which the *rpb1* locus is tagged with eGFP. (C) Immunoblot analysis of Rpb1-eGFP. The α-eGFP antibody correctly detected the Rpb1-eGFP fusion protein in the newly created strain (lane 3), but not in the wild type (lane 2, negative control) in the uncropped α-eGFP immunoblot. The α-CTD antibody detected the larger Rpb1-eGFP in the Rpb1-eGFP strain (lane 5) and the smaller unfused Rpb1 in the wild type (lane 4) in the α-CTD immunoblot. The H3 loading control is shown for each antibody because each antibody was imaged at a different exposure. Uncropped immunoblots are shown in Figure S29. (D) Differential interference contrast (DIC) and GFP fluorescence confocal microscopy images of Rpb1-eGFP cells. In the left panel, a merge of the DIC channel and the eGFP fluorescence channel is shown. In the right panel, eGFP signals are rendered with inverted contrast. (E) Fluorescence microscopy analysis of Rpb1-eGFP in interphase (P) and G0, in the Rpb1-eGFP strain. Columns, left to right: differential interference contrast (DIC), DAPI fluorescence (DNA) rendered in inverse contrast, eGFP fluorescence (Rpb1-eGFP) rendered in inverse contrast, and merge of the two fluorescence channels. Cells were fixed with formaldehyde. (F) Spot tests of proliferating (P) and G0 cells of the Rpb1-eGFP strain after a 30-minute incubation in YES and EMM−N respectively, with and without heat stress.

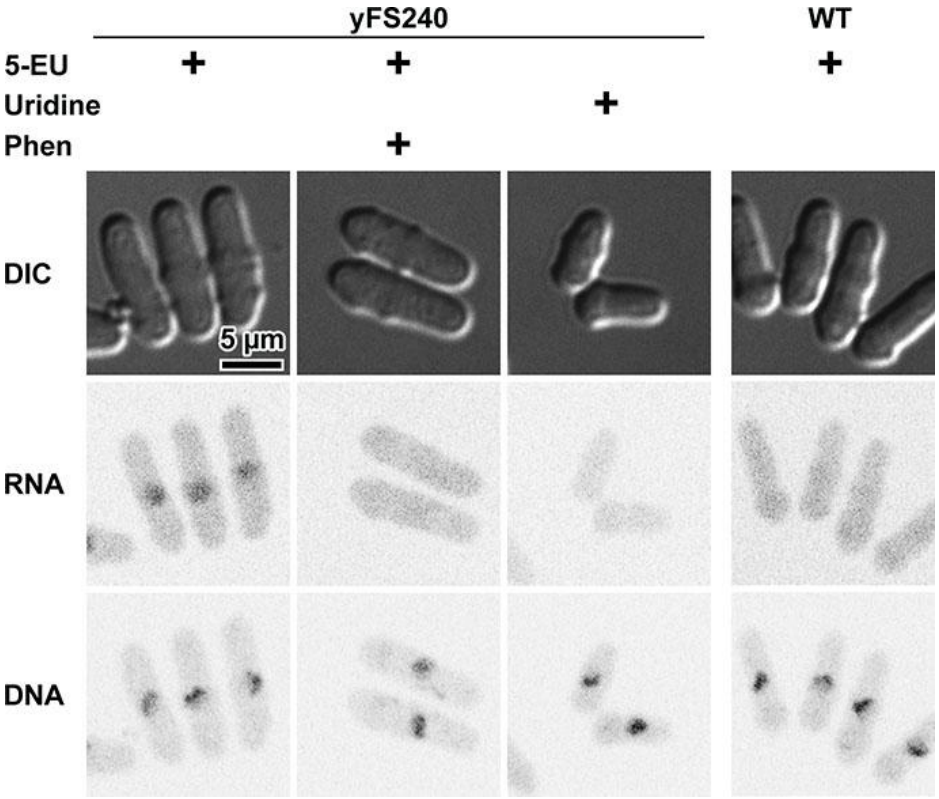

Figure S2. Controls for 5-EU RNA labelling.

1417 Proliferating yFS240 or wild-type cells incubated 10 minutes with 5-EU, uridine, or 5-EU
1418 plus the transcription inhibitor phenanthroline (Phen). The cells were then labelled with
1419 Alexa Fluor 488 and counterstained with DAPI.
1420
1421
1422

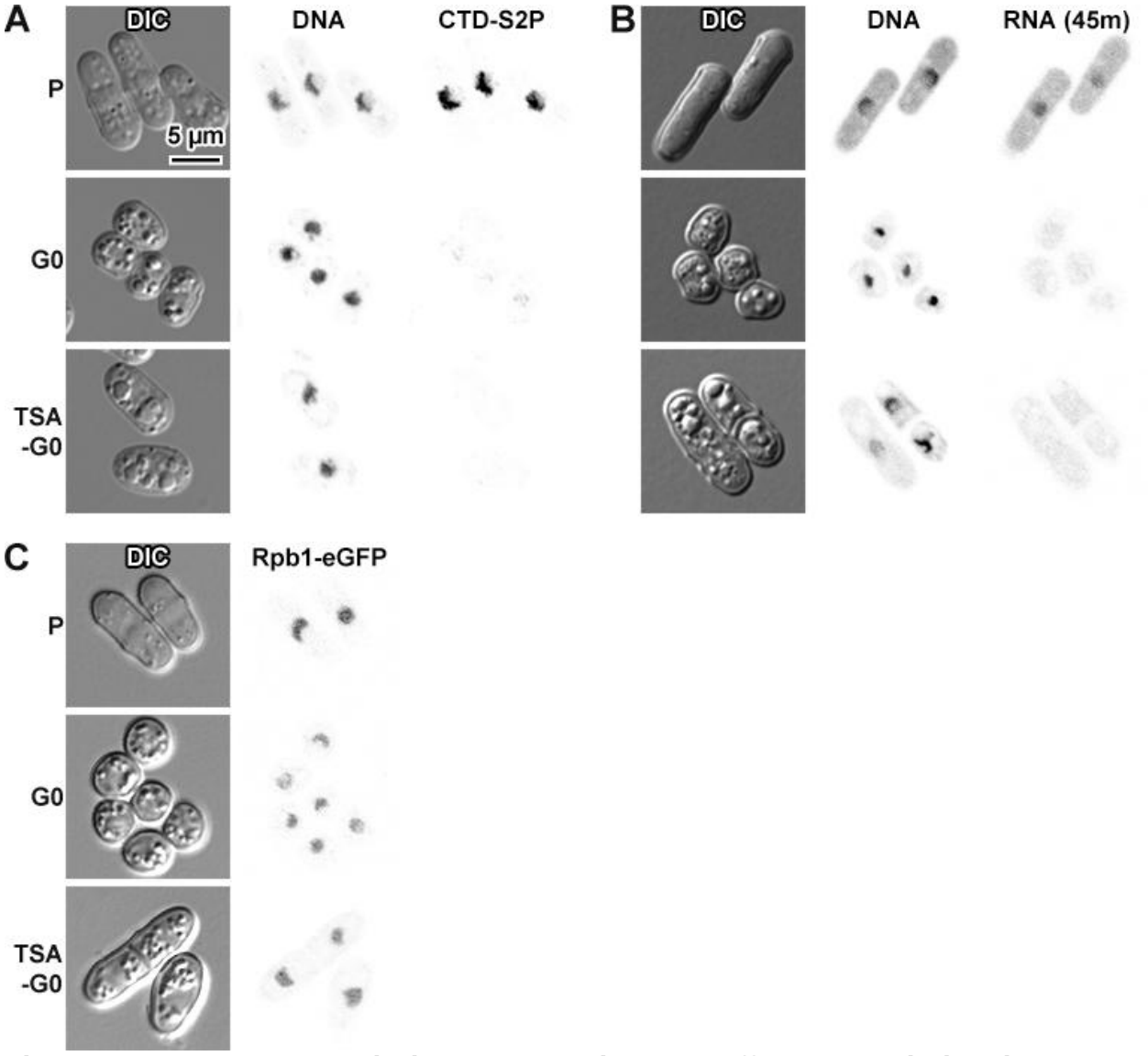

Figure S3. TSA treatment during G0 entry does not affect transcriptional repression.

(A) DIC and fluorescence microscopy of proliferating (P), G0, and TSA-G0 wild-type cells. The cells were stained for DNA with DAPI and immunostained for RNA polymerase II with CTD-S2P. (B) DIC and fluorescence microscopy of proliferating (P), G0, and TSA-G0 yFS240 cells. The cells were incubated with 5-EU for 45 minutes to increase the amount of 5-EU incorporated into RNA. Nascent RNA was then ligated to Alexa Fluor 488 for fluorescence detection. (C) DIC and fluorescence microscopy of proliferating (P), G0 and TSA-G0 Rpb1-eGFP cells. The cells were unfixed and unstained; the fluorescence signal is from cell-expressed Rpb1-eGFP.

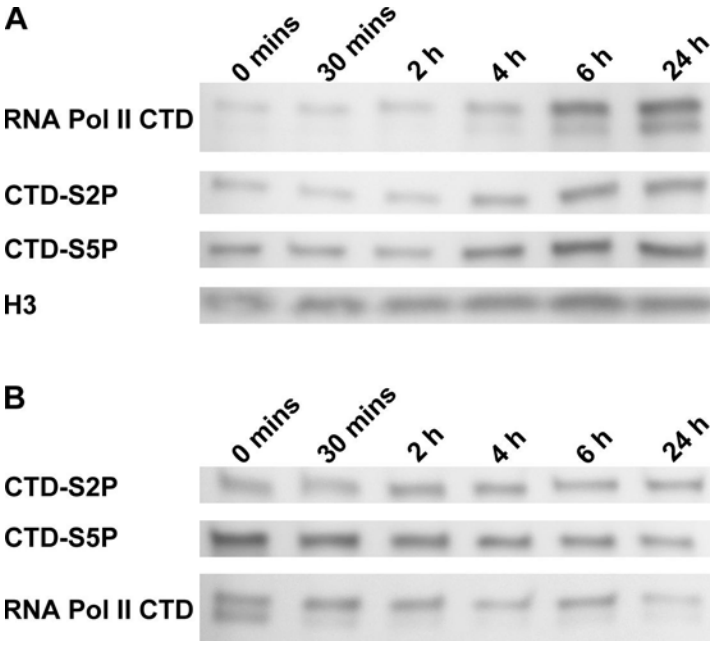

Figure S4. RNAPII-CTD transcription marker levels in whole-cell lysates do not markedly increase after G0 cells are switched to nutrient-rich medium.
(A) Immunoblots of lysates from G0 wild type cells 0 minutes, 30 minutes, 2 hours, 4 hours, 6 hours or 24 hours after being transferred to YES medium, using a pan-CTD antibody, an α-CTD-S2P antibody and an α-CTD-S5P antibody. Loading controls were done with a H3 antibody (lower row). (B) Immunoblots of another batch of lysates from G0 wild type cells 0 minutes, 30 minutes, 2 hours, 4 hours, 6 hours or 24 hours after being transferred to YES medium, using an α-CTD-S2P antibody and an α-CTD-S5P antibody. Loading controls were done with a pan-CTD antibody (lower row). Uncropped immunoblots are shown in Figure S29.

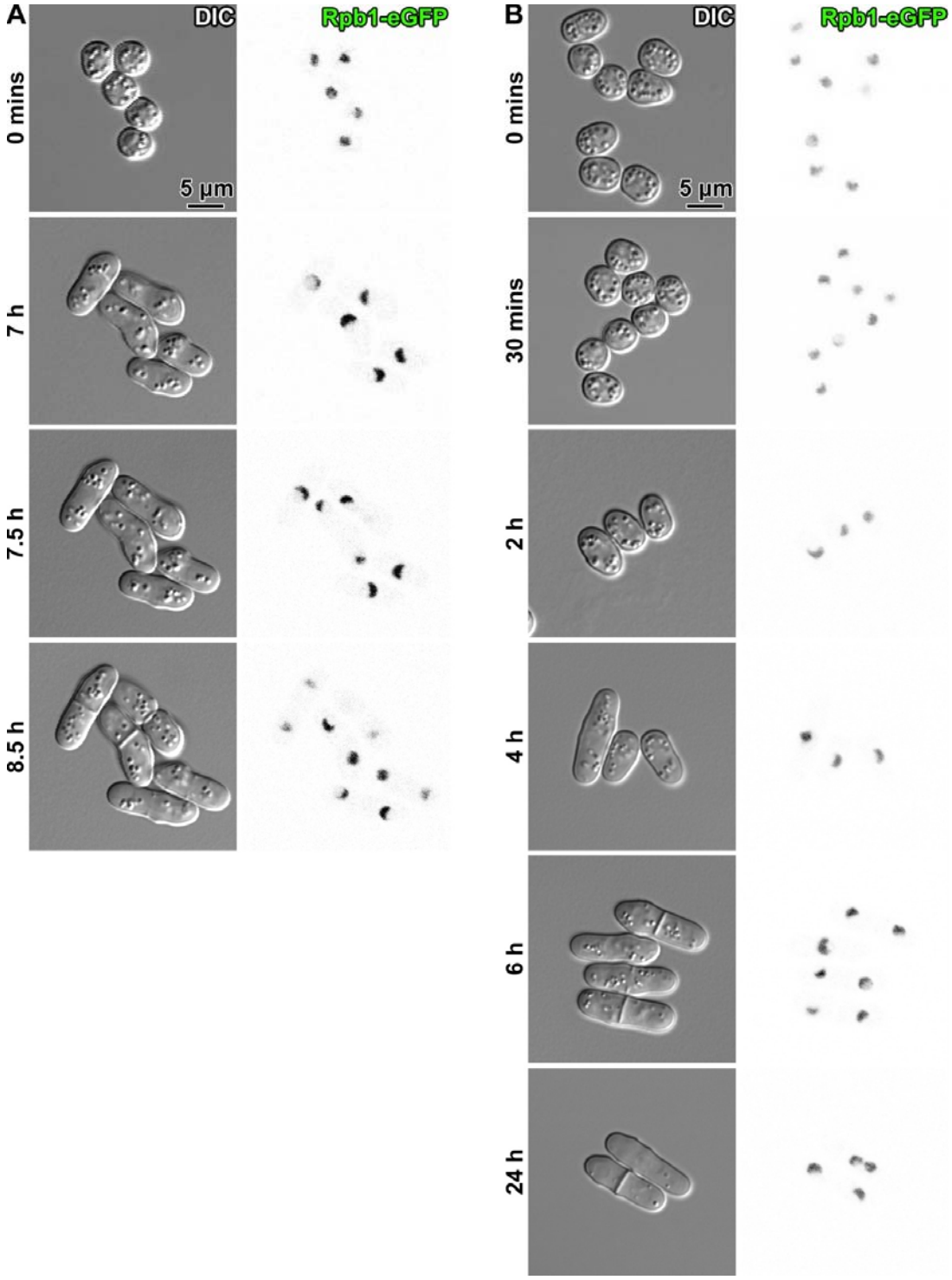

Figure S5. RNAPII does not exhibit observable changes within 6 hours after G0 cells are subjected to nutrient-rich medium.

Fluorescence microscopy analysis of RNAPII content in cells after Rpb1-eGFP G0 cells are exposed to nutrient-rich medium. Columns, left to right: differential interference contrast (DIC) and eGFP fluorescence (Rpb1-eGFP). (A) Select samples from time-lapse images of a single group of cells imaged immediately after deposition on a YES agar pad (0 mins), just before (7 h), and just after (7.5 h) one of the cells finishes

nuclear division, and just after all five of the cells finish nuclear division (8.5 h). See Movie S1 for the full set of time-lapse images. (B) Different groups of cells collected from liquid culture at different time points.

Movie S1. Time-lapse fluorescence microscopy of Rpb1-eGFP cells exiting G0, deposited on an agar pad.
The images on the left are differential interference contrast (DIC), the images on the right are eGFP fluorescence (Rpb1-eGFP). The interval between each frame is 30 minutes.

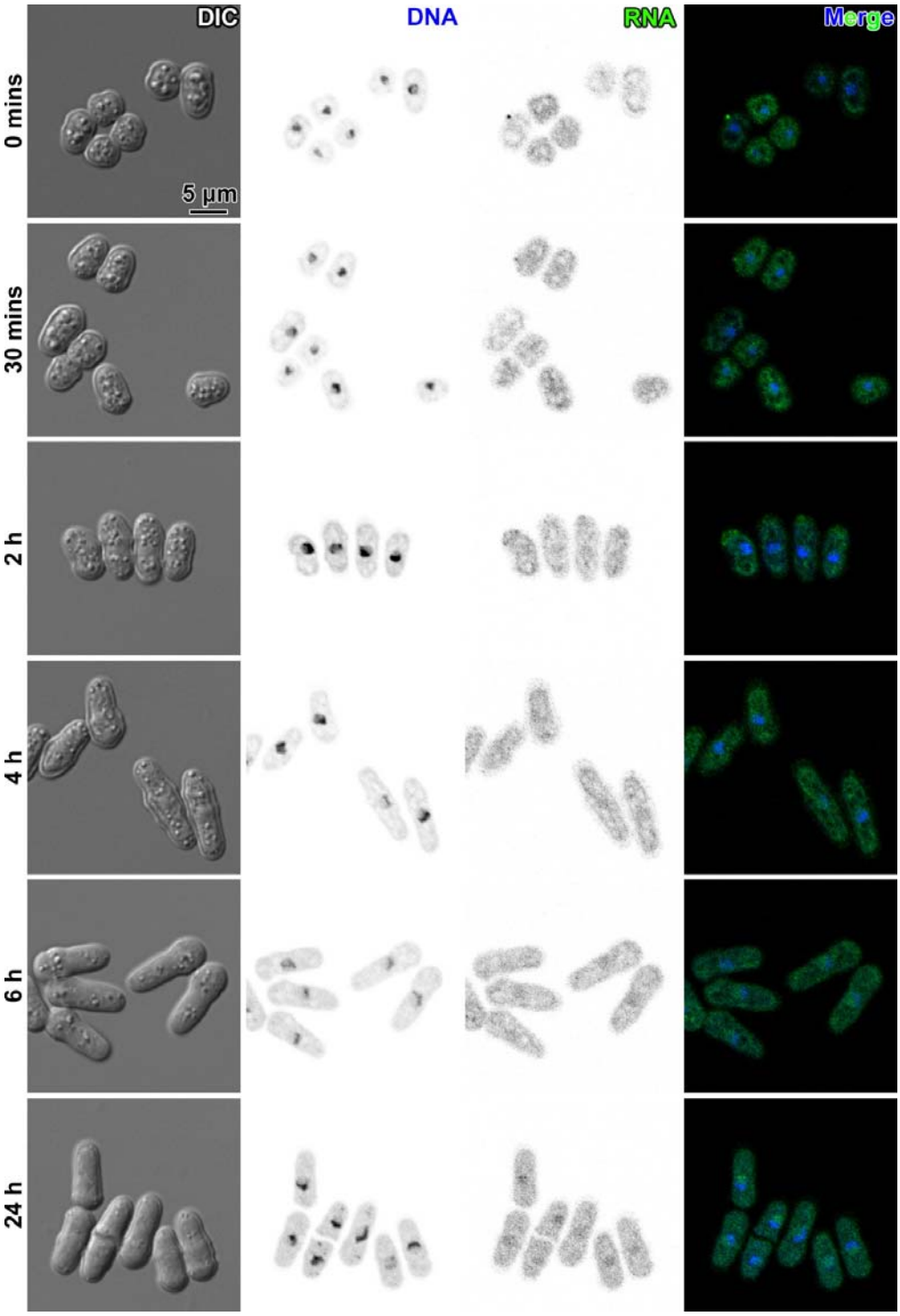

Figure S6. Nascent RNA transcripts are observable 6 hours after G0 cells are subjected to nutrient-rich medium.
Fluorescence microscopy analysis of RNA content in cells after yFS240 G0 cells are exposed to nutrient-rich medium. Columns, left to right: differential interference contrast (DIC), DAPI fluorescence (DNA), Alexa Fluor 488 fluorescence (RNA) and merge.

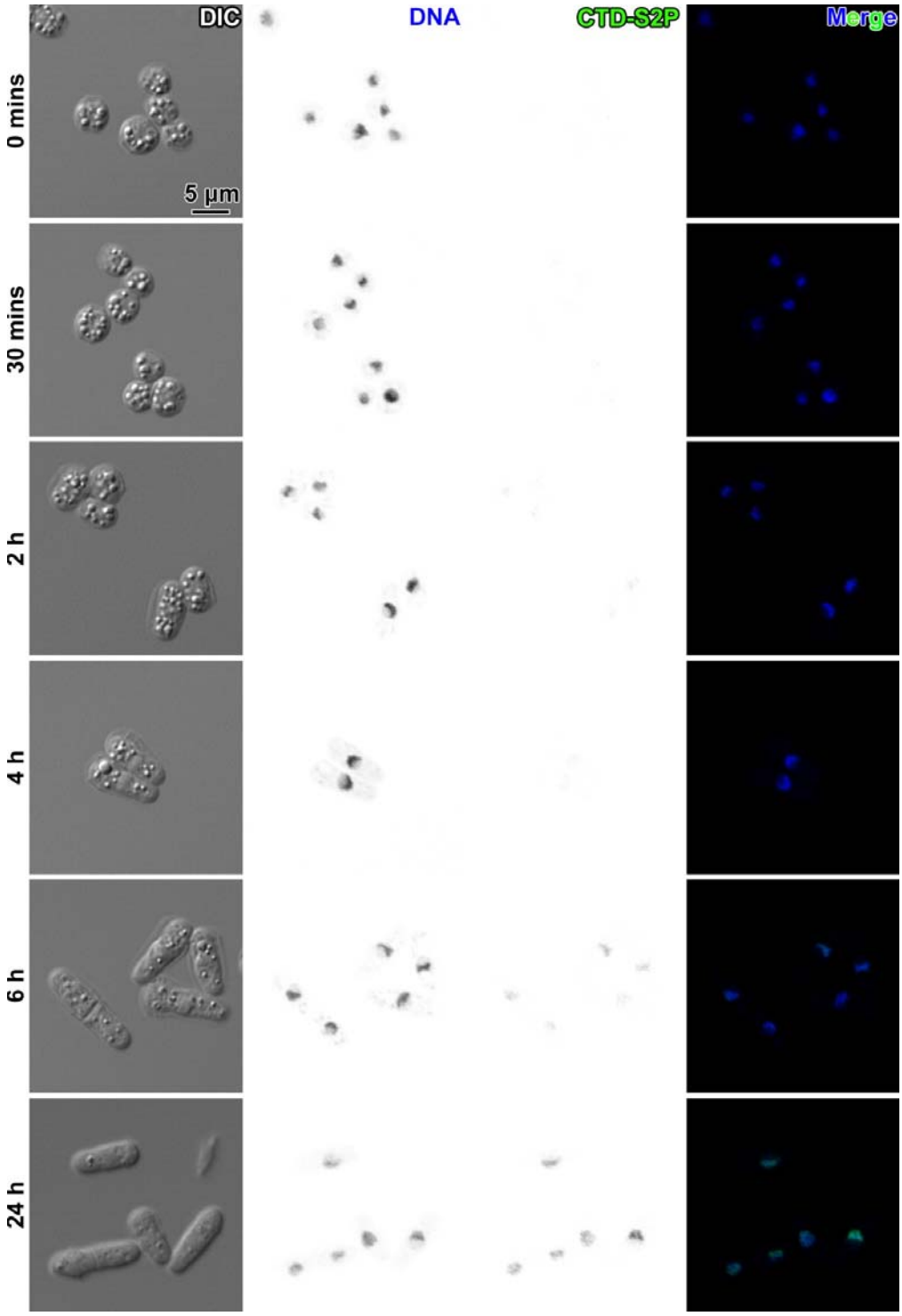

Figure S7. RNAPII-CTD-S2P levels increase 6 hours after G0 cells are subjected to nutrient-rich medium.

Fluorescence microscopy analysis of RNAPII-CTD-S2P content in cells after wild-type G0 cells are exposed to nutrient-rich medium. Columns, left to right: differential interference contrast (DIC), DAPI fluorescence (DNA), Alexa Fluor 488 immunofluorescence (CTD-S2P) and merge.

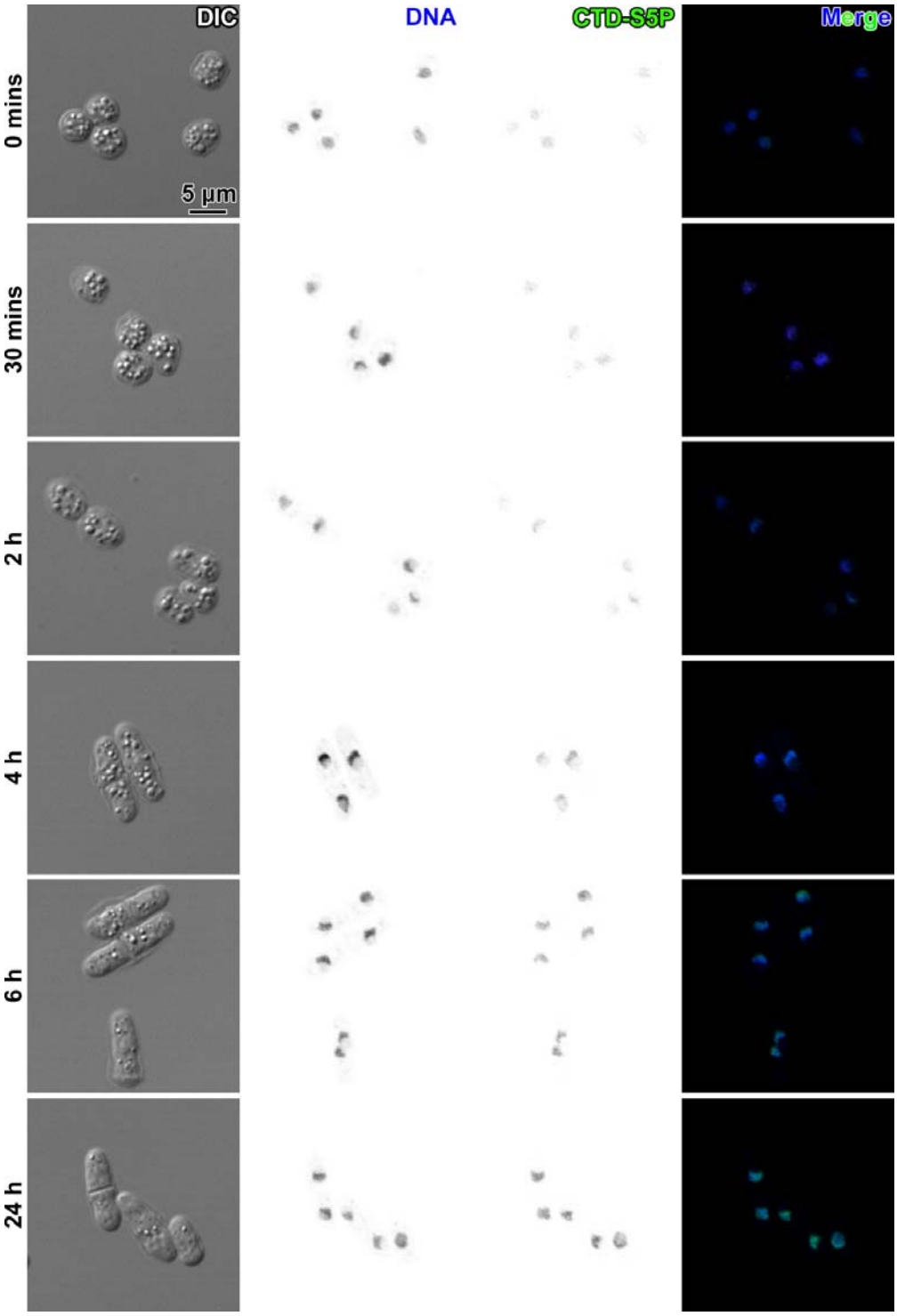

Figure S8. RNAPII-CTD-S5P levels increase 4 hours after G0 cells are changed into nutrient-rich medium.

Fluorescence microscopy analysis of RNAPII-CTD-S5P content in cells after wild-type G0 cells are exposed to nutrient-rich medium. Columns, left to right: differential interference contrast (DIC), DAPI fluorescence (DNA), Alexa Fluor 488 immunofluorescence (CTD-S5P) and merge.

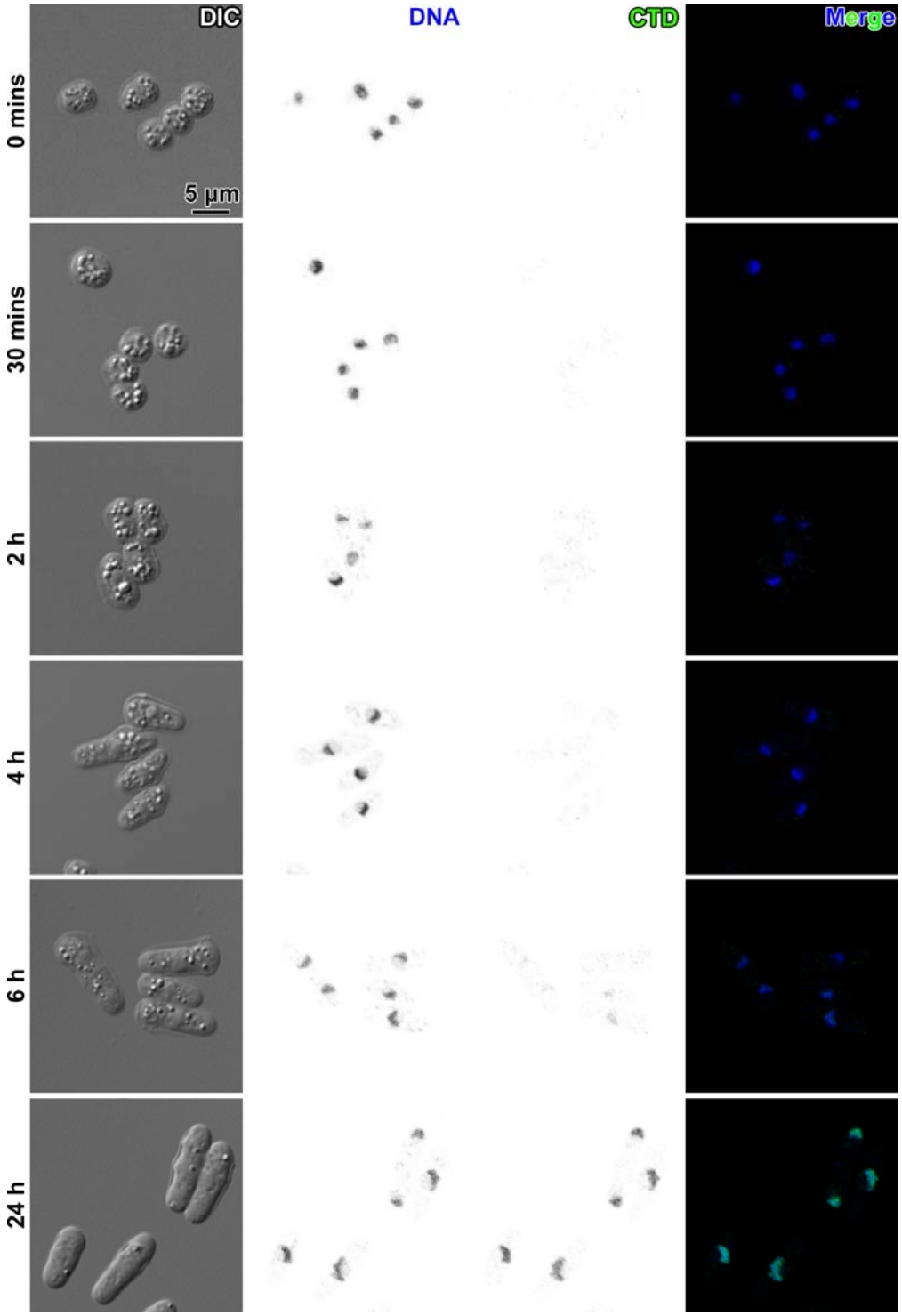

Figure S9. RNAPII CTDs become more detectable 6 hours after G0 cells are changed into nutrient-rich medium.
Fluorescence microscopy analysis of RNAPII content in cells after wild-type G0 cells are exposed to nutrient-rich medium. Columns, left to right: differential interference contrast (DIC), DAPI fluorescence (DNA), Alexa Fluor 488 immunofluorescence (CTD) and merge.

1494

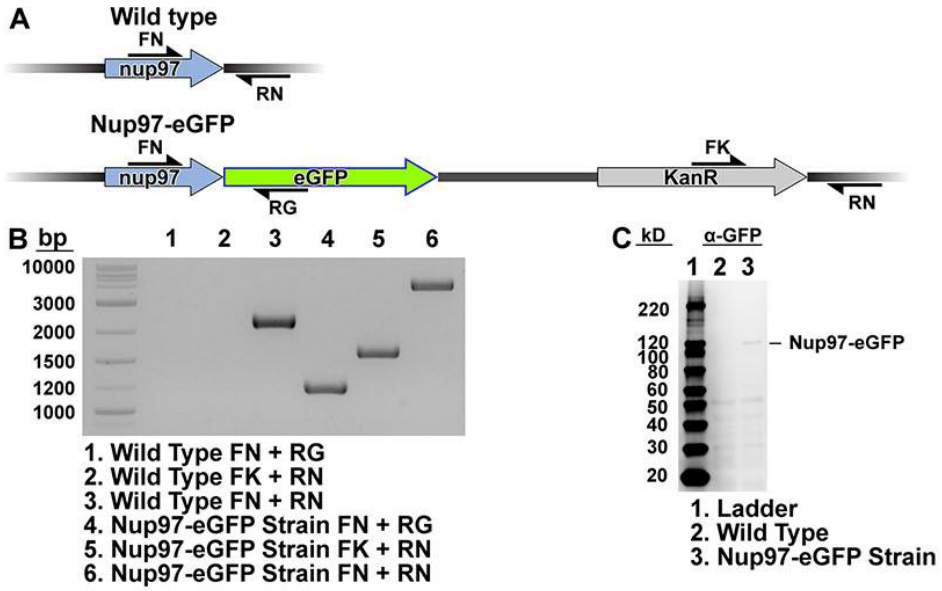

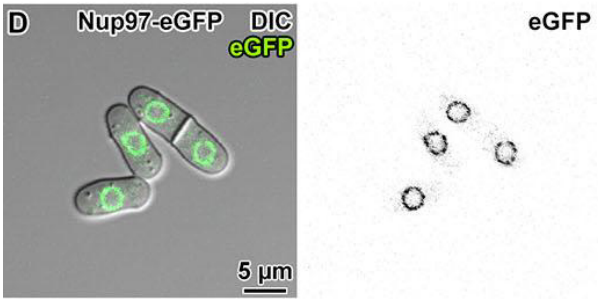

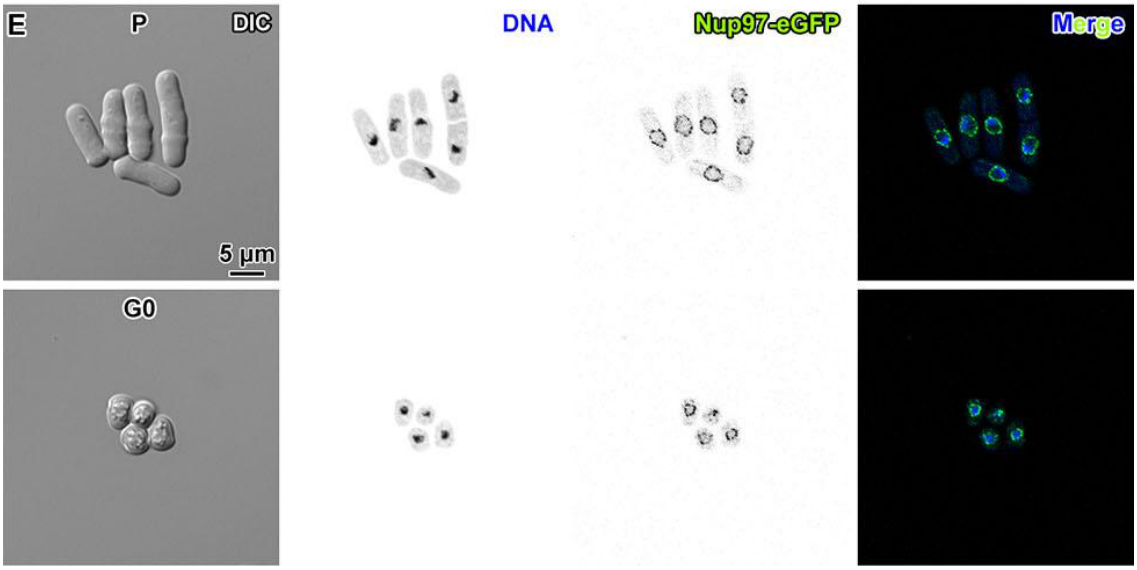

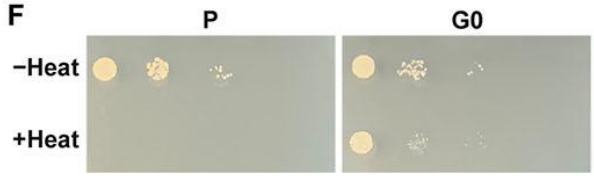

1495

Figure S10. Construction of Nup97-eGFP strain.
(A) Map of the *nup97* locus in the parent (wild-type) *S. pombe* strain MBY99 and the Nup97-eGFP strain LGSP0002. Primers used for PCR verification are indicated with the half arrow symbols. (B) Agarose gel of PCR amplicons expected from wild-type (control) and from Nup1-eGFP genomic DNA, in which the *nup97* locus is tagged with eGFP. (C) Immunoblot analysis of the Nup97-eGFP. The α-eGFP antibody correctly detected the Nup97-eGFP fusion protein in the newly created strain (lane 3), but not in the wild type (lane 2, negative control) in the uncropped α-eGFP immunoblot. (D) Differential interference contrast (DIC) and eGFP fluorescence confocal microscopy images of live Nup97-eGFP cells. In the left panel, a merge of the DIC channel and the eGFP fluorescence channel is shown. In the right panel, eGFP signals are rendered with inverted contrast. (E) Fluorescence microscopy analysis of Nup97-eGFP in interphase (P) and G0, in the Nup97-eGFP strain. Left to right: differential interference contrast (DIC), DAPI fluorescence (DNA) rendered in inverse contrast, eGFP fluorescence (Nup97-eGFP) rendered in inverse contrast, and merge of the two fluorescence channels. Cells were fixed with formaldehyde. (F) Spot tests of proliferating (P) and G0 cells of the Nup97-eGFP strain after a 30-minute incubation in YES and EMM−N respectively, with and without heat stress.

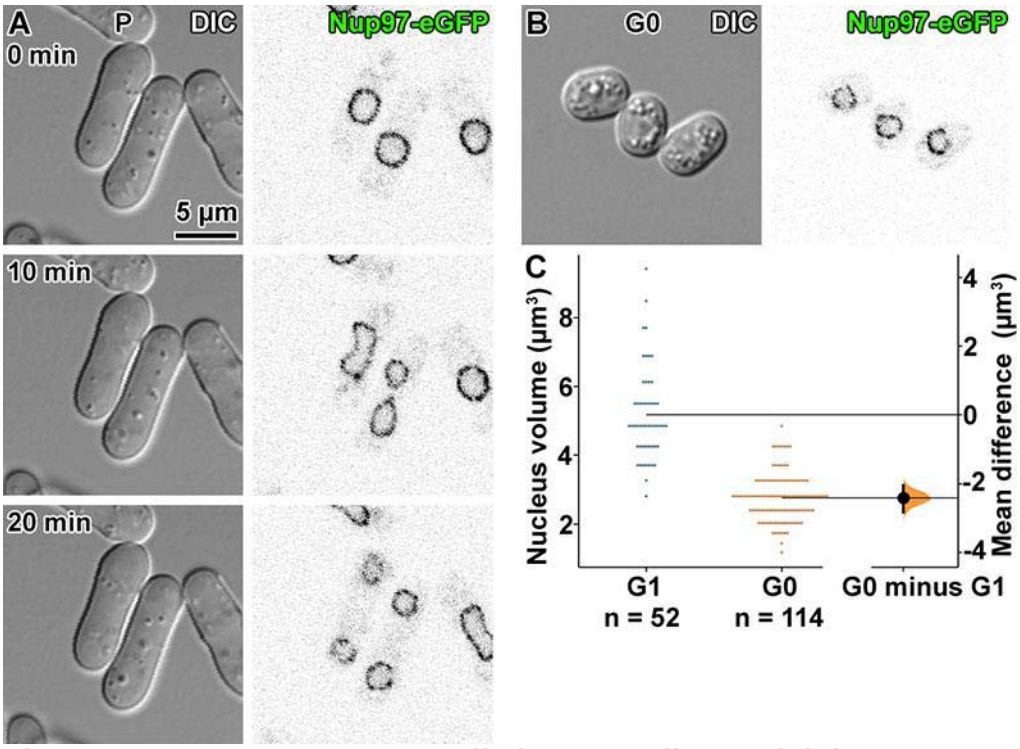

Figure S11. G0 Nup97-eGFP cells have smaller nuclei than G1 Nup97-eGFP cells. (A) Differential interference contrast (DIC) (left) and eGFP fluorescence (right) confocal fluorescence microscopy images of proliferating Nup97-eGFP cells just before (0 minutes), during (10 minutes), and just after (20 minutes) nuclear division. G1 nucleus sizes were determined from the nuclei that had just divided. See Movie S2 for the time-lapse images. (B) DIC and eGFP fluorescence confocal fluorescence microscopy images of G0 Nup97-eGFP cells. (C) Gardner-Altman plot of the mean difference between G1 and G0 nucleus volumes. Both groups are plotted on the left axes; the mean difference is plotted on a floating axis on the right. The mean difference is depicted as a dot; the 95% confidence interval is indicated by the ends of the vertical error bar (Ho et al., 2019).

Movie S2. Time-lapse fluorescence microscopy of proliferating Nup97-eGFP cells, deposited on an agar pad.
The images on the left are differential interference contrast (DIC), the images on the right are eGFP fluorescence (Nup97-eGFP). The interval between each frame is 10 minutes.

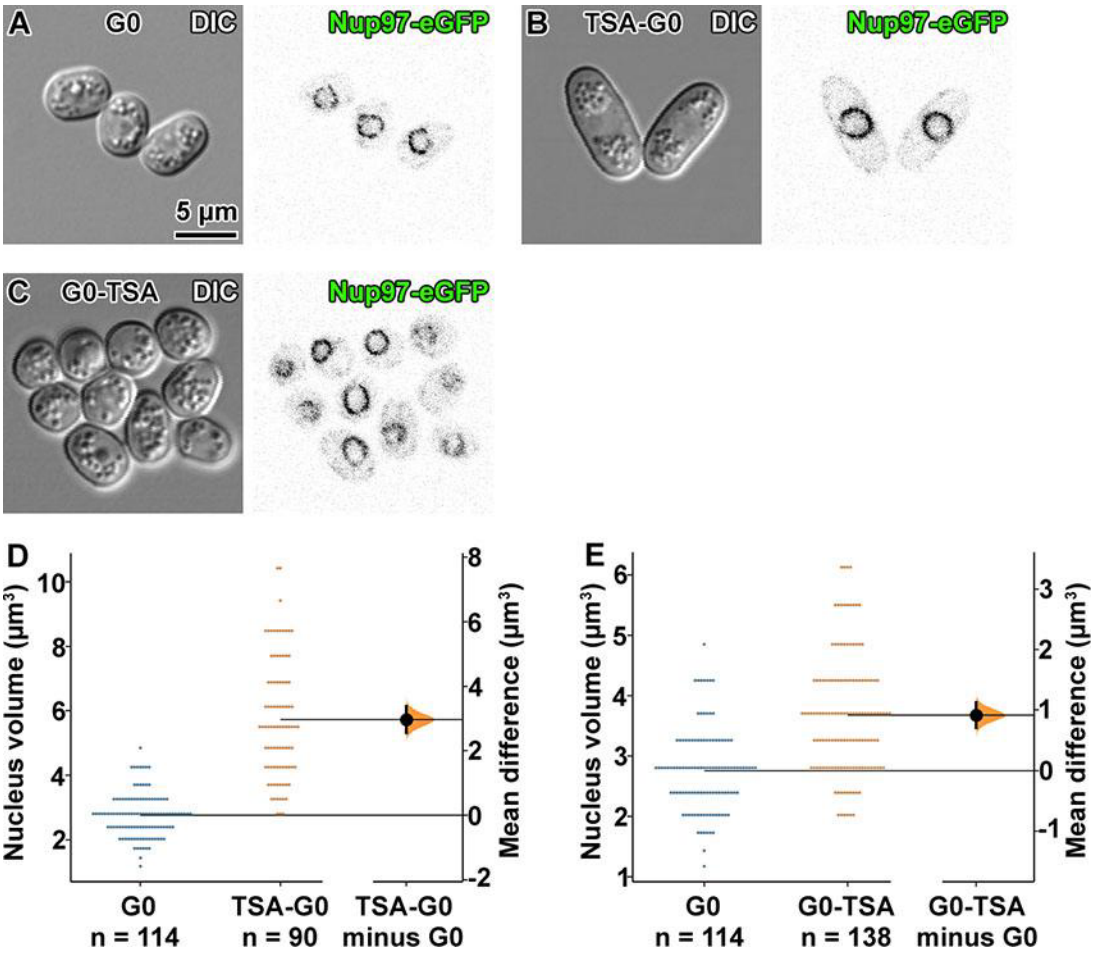

Figure S12. G0 Nup97-eGFP cells treated with TSA have larger nuclei than untreated G0 Nup97-eGFP cells.

(A) Differential interference contrast (DIC) (left) and eGFP fluorescence (right) confocal fluorescence microscopy images of G0 Nup97-eGFP cells. (B) DIC and eGFP fluorescence confocal fluorescence microscopy images of TSA-G0 Nup97-eGFP cells. (C) DIC and eGFP fluorescence confocal fluorescence microscopy images of G0-TSA Nup97-eGFP cells. Gardner-Altman plot of (D) the mean difference between G0 and TSA-G0 nucleus volumes, and (E) the mean difference between G0 and G0-TSA nucleus volumes. In each plot, both groups are plotted on the left axes; the mean difference is plotted on a floating axis on the right. The mean difference is depicted as a dot; the 95% confidence interval is indicated by the ends of the vertical error bar (Ho et al., 2019).

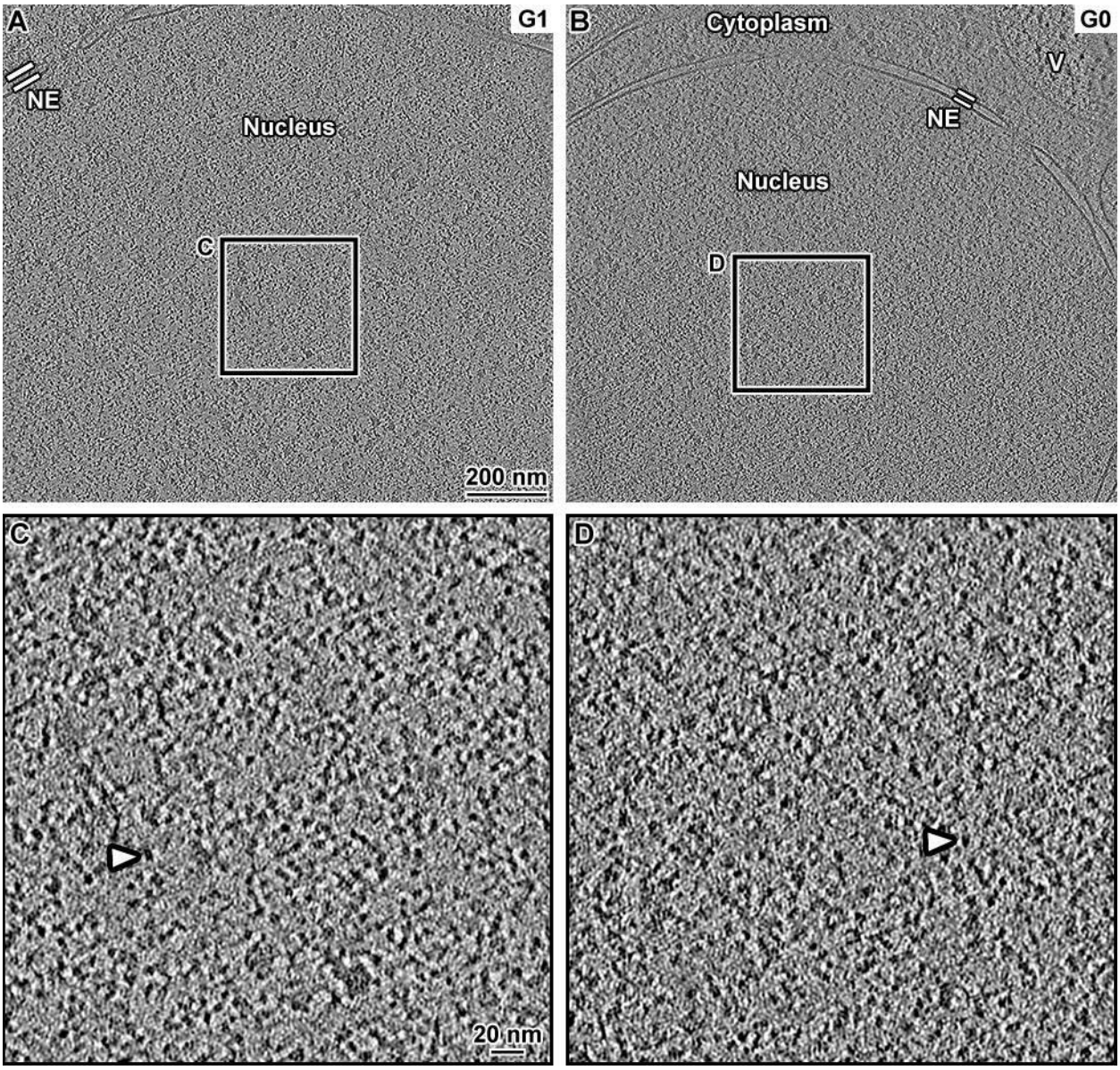

Figure S13. G0 cells have a denser nucleoplasm than G1 cells.
Defocus phase-contrast cryotomographic slices (12 nm) of a G1-arrested (A) and a G0 (B) cell, imaged with defocus contrast. NE: nuclear envelope. (C and D) Four-fold enlargements of the regions boxed in panels A and B, respectively. Nucleosome-like densities are indicated by arrowheads.

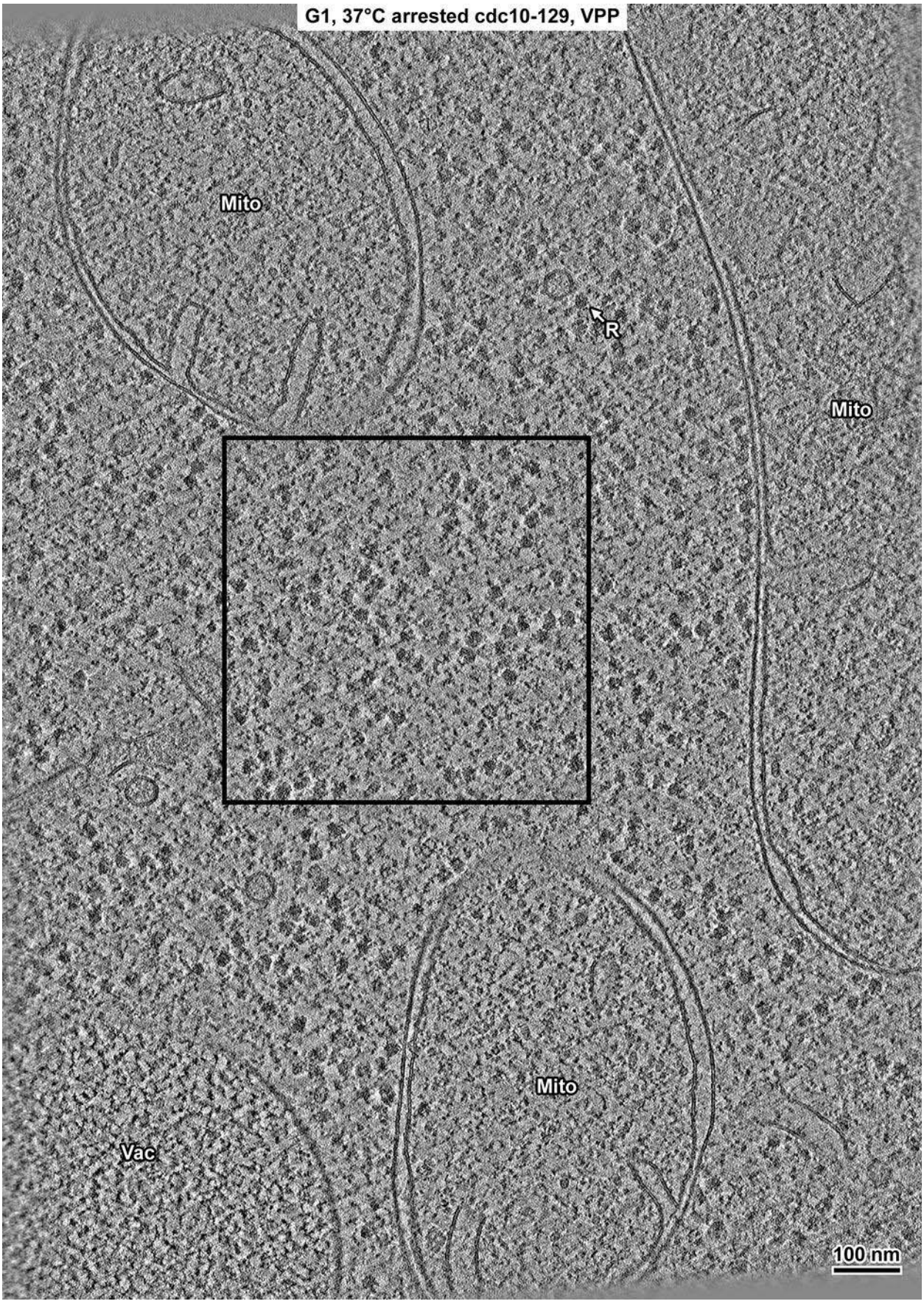

1554

Figure S14. Overview of a G1 cytoplasm cryolamella

Volta cryotomographic slice (12 nm) of a ribosome-rich region of the cytoplasm in a G1-arrested *cdc10-129* cell cryolamella. The vacuoles (Vac), mitochondria (Mito), and a ribosome (R) are indicated. The boxed region was used for Fourier power spectrum analysis in Figures 6 and S28.

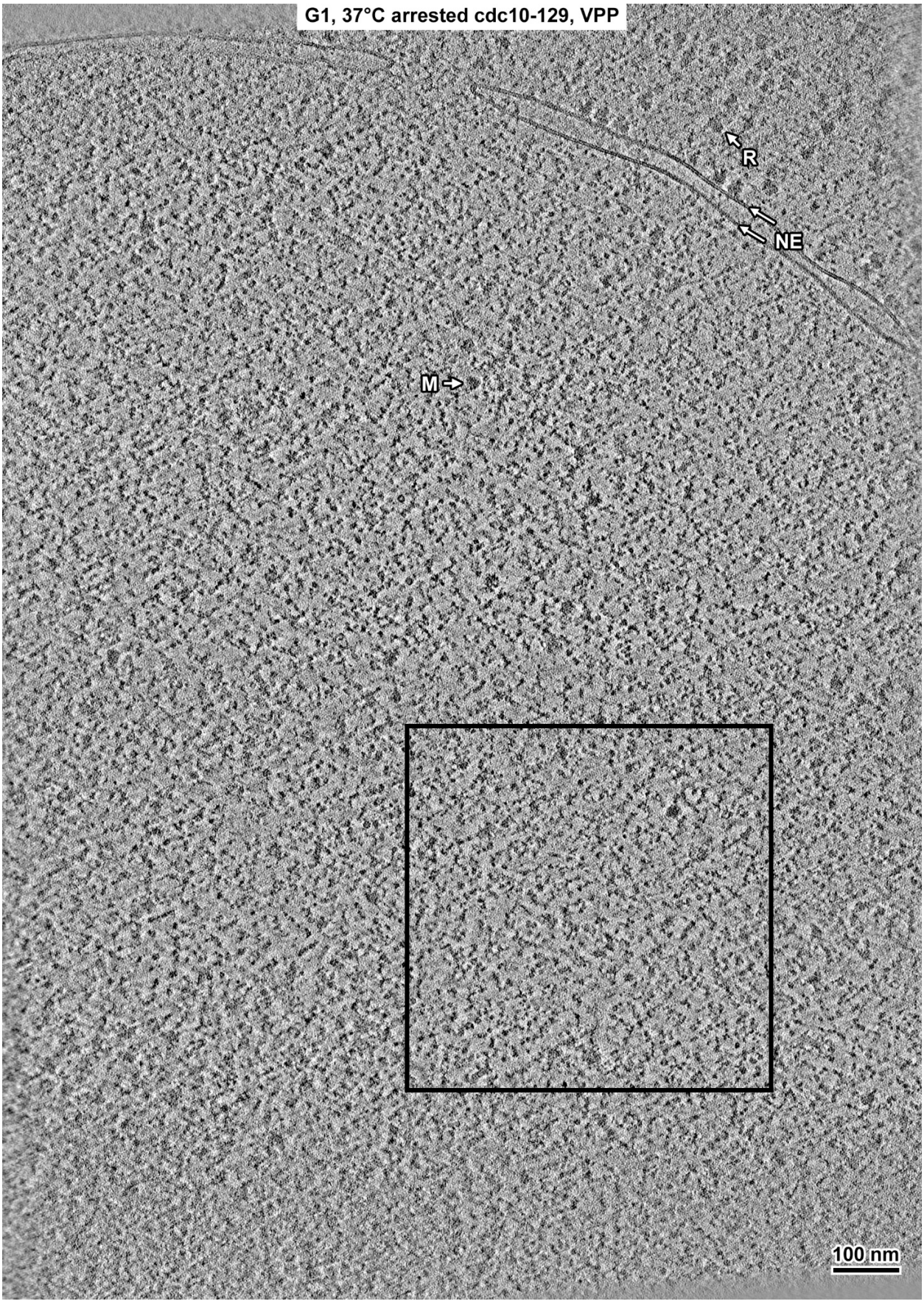

1561

Figure S15. Overview of a G1 nucleus cryolamella

Volta cryotomographic slice (12 nm) of the nucleus in a G1-arrested *cdc10-129* cell cryolamella. Some non-chromatin features are indicated: nuclear envelope (NE), megacomplex (M), and ribosome (R). The boxed region is shown with twofold enlargement in Figure S16, and was used for Fourier power spectrum analysis in Figure 6.

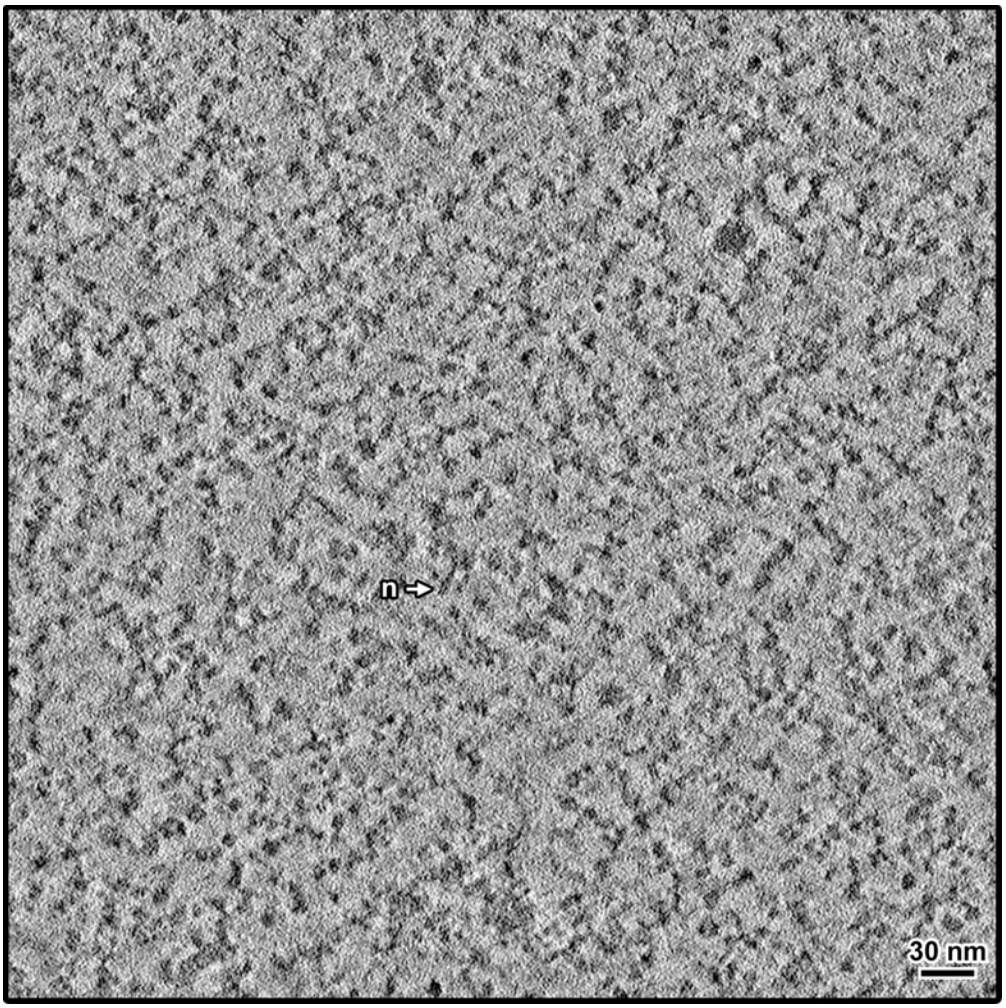

Figure S16. Twofold enlargement of selected region from G1 nucleus cryolamella
A region of a Volta cryotomographic slice (12 nm) of the nucleus in the G1-arrested *cdc10-129* cell from Figure S15, selected for Fourier power spectrum analysis in Figure 6. A nucleosome-like particle (n) is indicated.

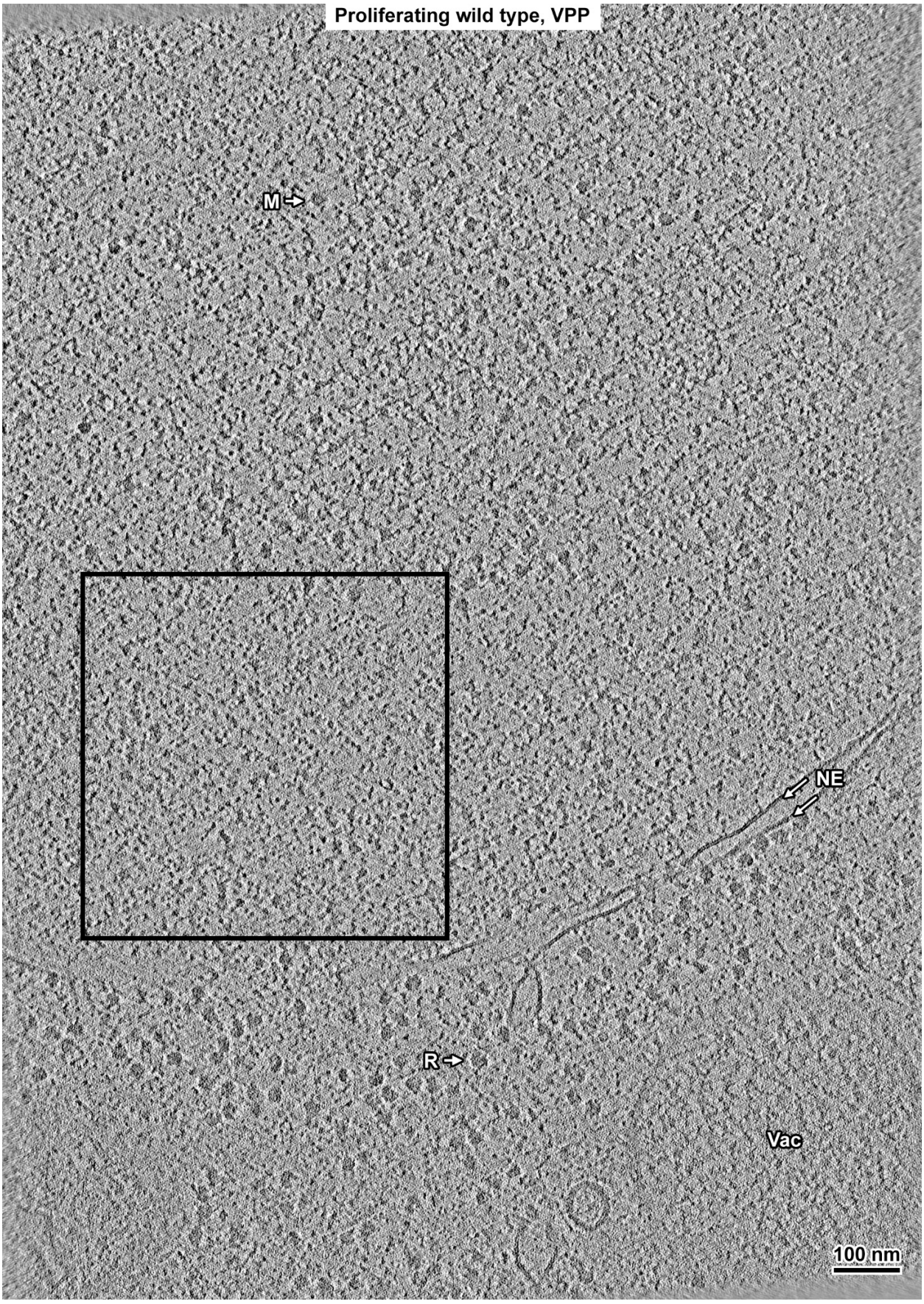

1574

Figure S17. Overview of a proliferating cell nucleus cryolamella

Volta cryotomographic slice (12 nm) of the nucleus in a proliferating cell cryolamella. Some non-chromatin features are indicated: nuclear envelope (NE), megacomplex (M), ribosome (R) and vacuole (Vac). The boxed region is shown with twofold enlargement in Figure S18, and was used for Fourier power spectrum analysis in Figure 6.

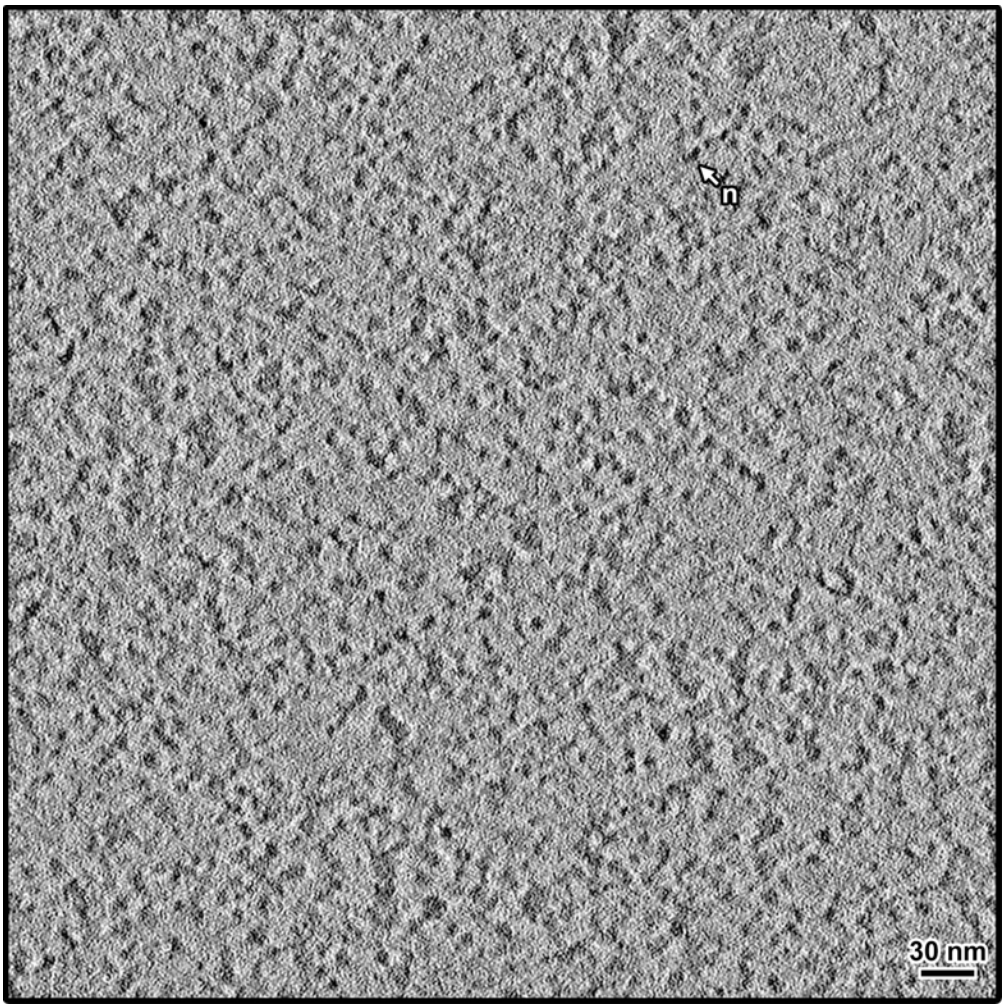

Figure S18. Twofold enlargement of selected region from proliferating nucleus cryolamella

A region of a Volta cryotomographic slice (12 nm) of the nucleus in the proliferating cell from Figure S17, selected for Fourier power spectrum analysis in Figure 6. A nucleosome-like particle (n) is indicated.

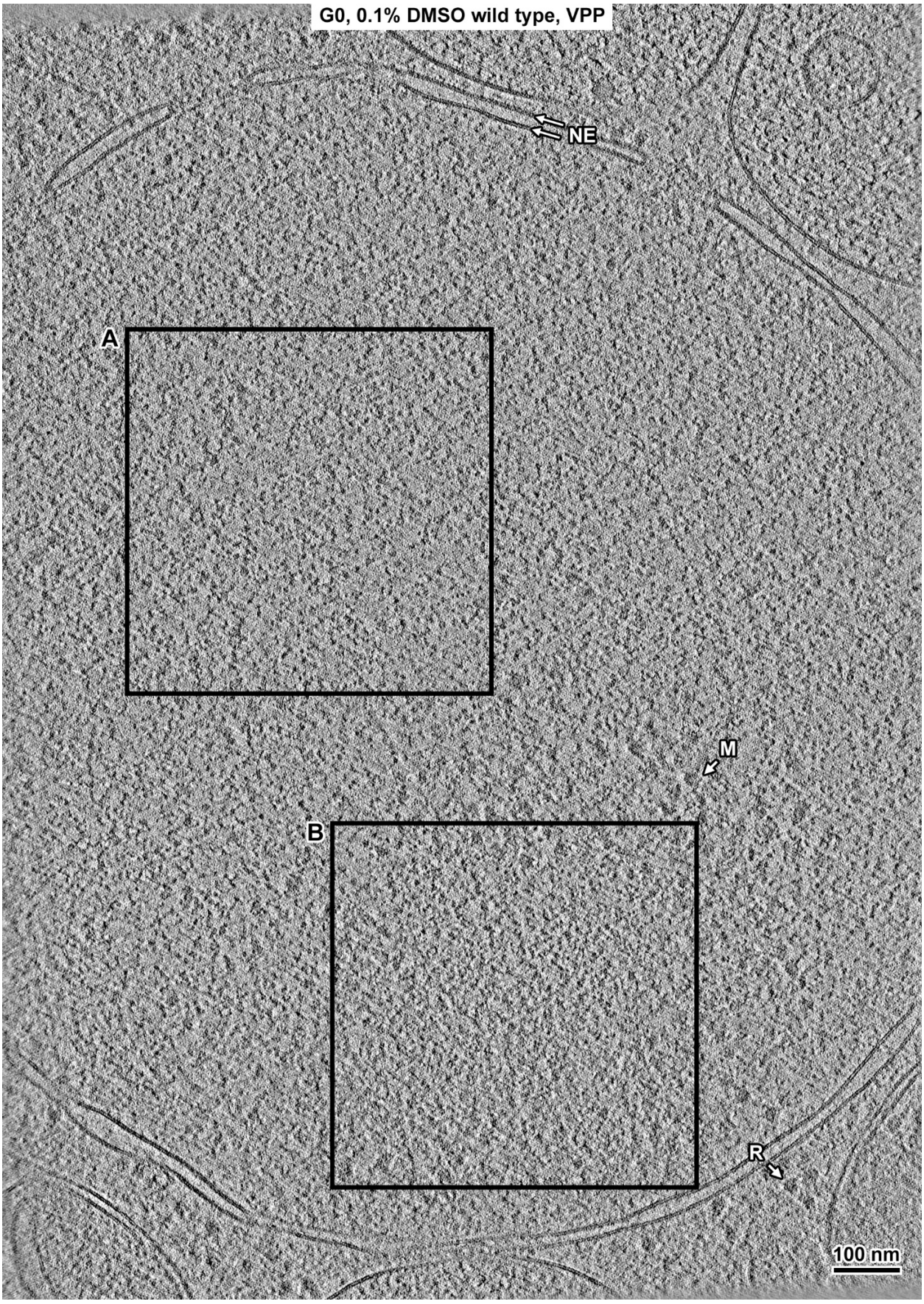

1587

Figure S19. Overview of a G0 nucleus cryolamella

Volta cryotomographic slice (12 nm) of a nucleus cryolamella of a wild-type G0 cell treated with 0.1% DMSO during G0 entry. Some non-chromatin features are indicated: nuclear envelope (NE), megacomplex (M), and ribosome (R). The nucleoplasm boxed region (A) is shown with twofold enlargement in Figure S20, and was used for Fourier power spectrum analysis in Figures 6 and S28. The nucleolus boxed region (B) is shown with twofold enlargement in Figure S21, and was used for Fourier power spectrum analysis in Figure S28.

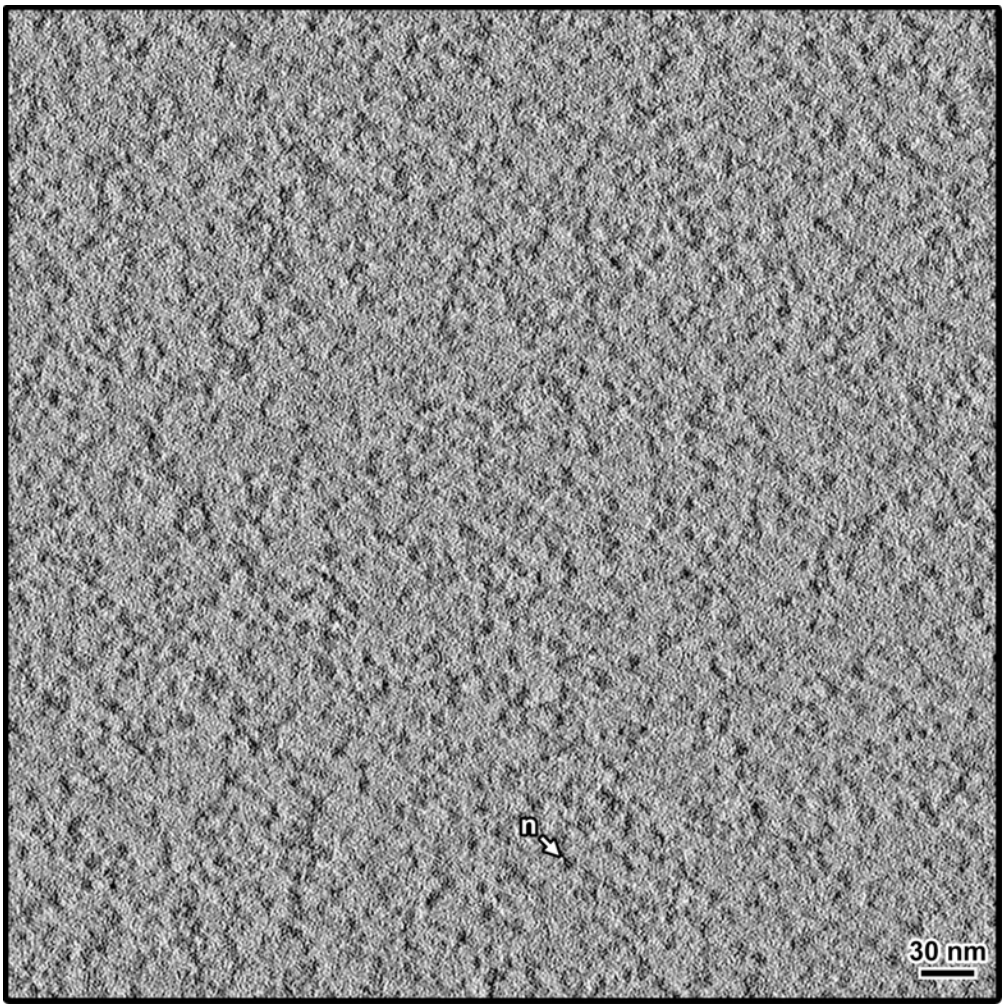

Figure S20. Twofold enlargement of selected nucleoplasm region from a G0 nucleus cryolamella

A region of a Volta cryotomographic slice (12 nm) of the nucleoplasm region of the nucleus in a wild-type G0 cell treated with 0.1% DMSO during G0 entry from Figure S19, selected for Fourier power spectrum analysis in Figures 6 and S28. A nucleosome-like particle (n) is indicated.

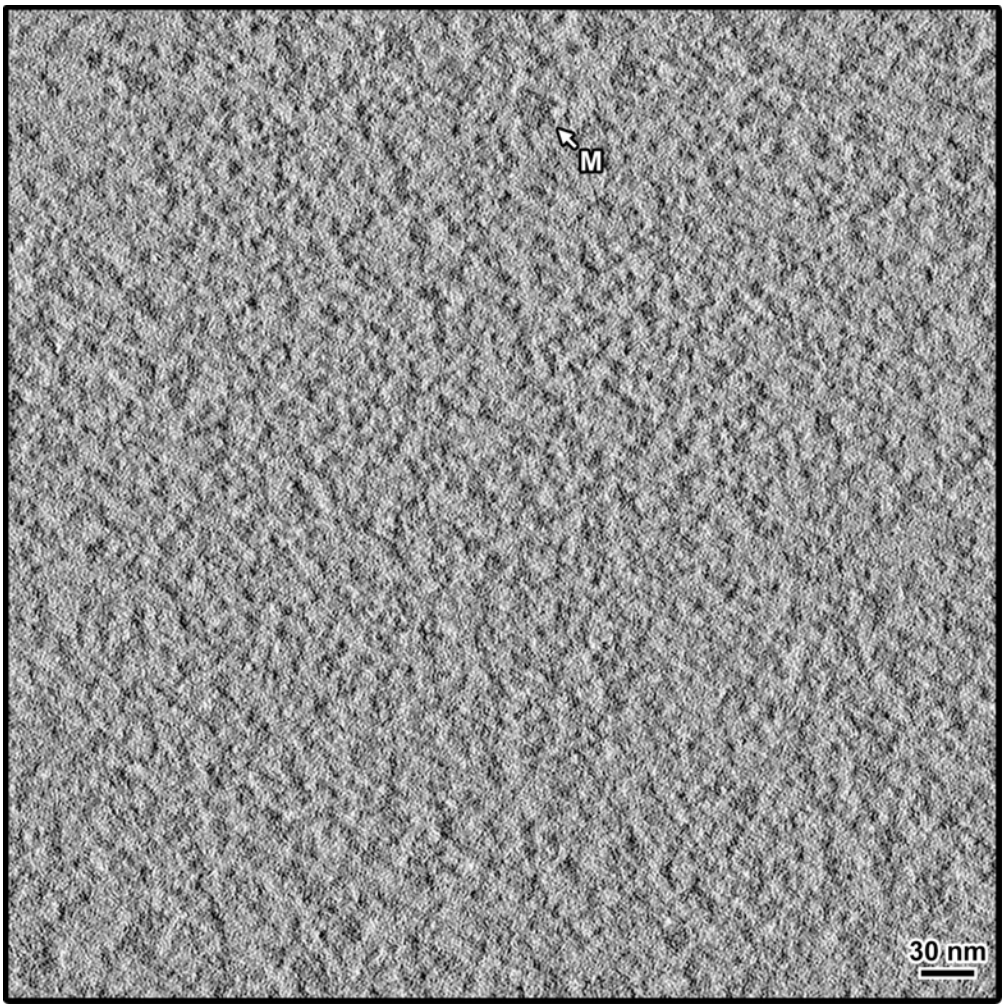

Figure S21. Twofold enlargement of selected nucleolus region from a G0 nucleus cryolamella

A region of a Volta cryotomographic slice (12 nm) of the nucleolus in a wild-type G0 cell treated with 0.1% DMSO during G0 from Figure S20, selected for Fourier power spectrum analysis in Figure S28. A megacomplex (M) is indicated.

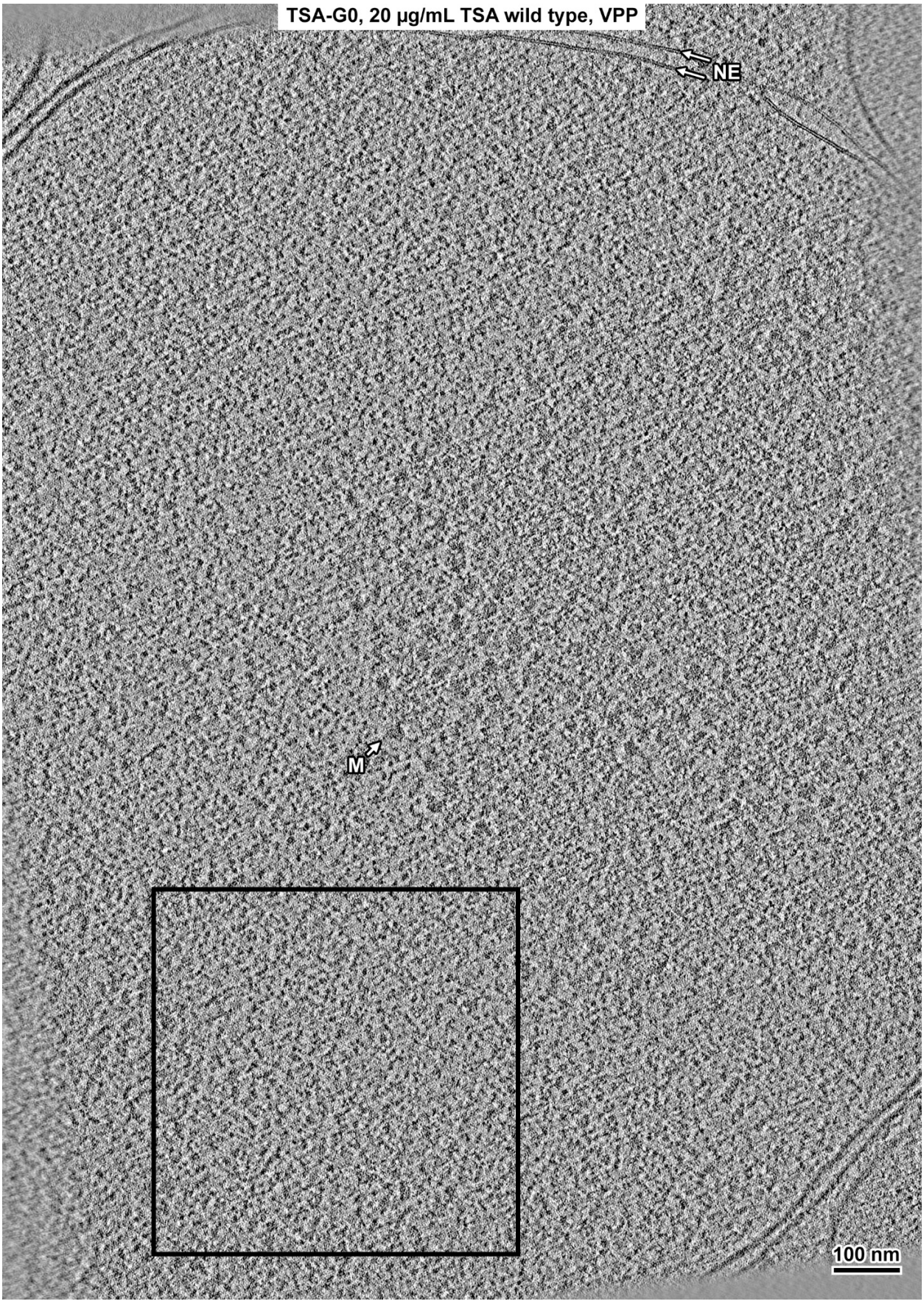

1611

Figure S22. Overview of a TSA-G0 nucleus cryolamella

Volta cryotomographic slice (12 nm) of a nucleus cryolamella of a wild-type G0 cell treated with 20 ng/µL TSA during G0 entry. Some non-chromatin features are indicated: nuclear envelope (NE) and megacomplex (M). The boxed region is shown with twofold enlargement in Figure S23, and was used for Fourier power spectrum analysis in Figure 6.

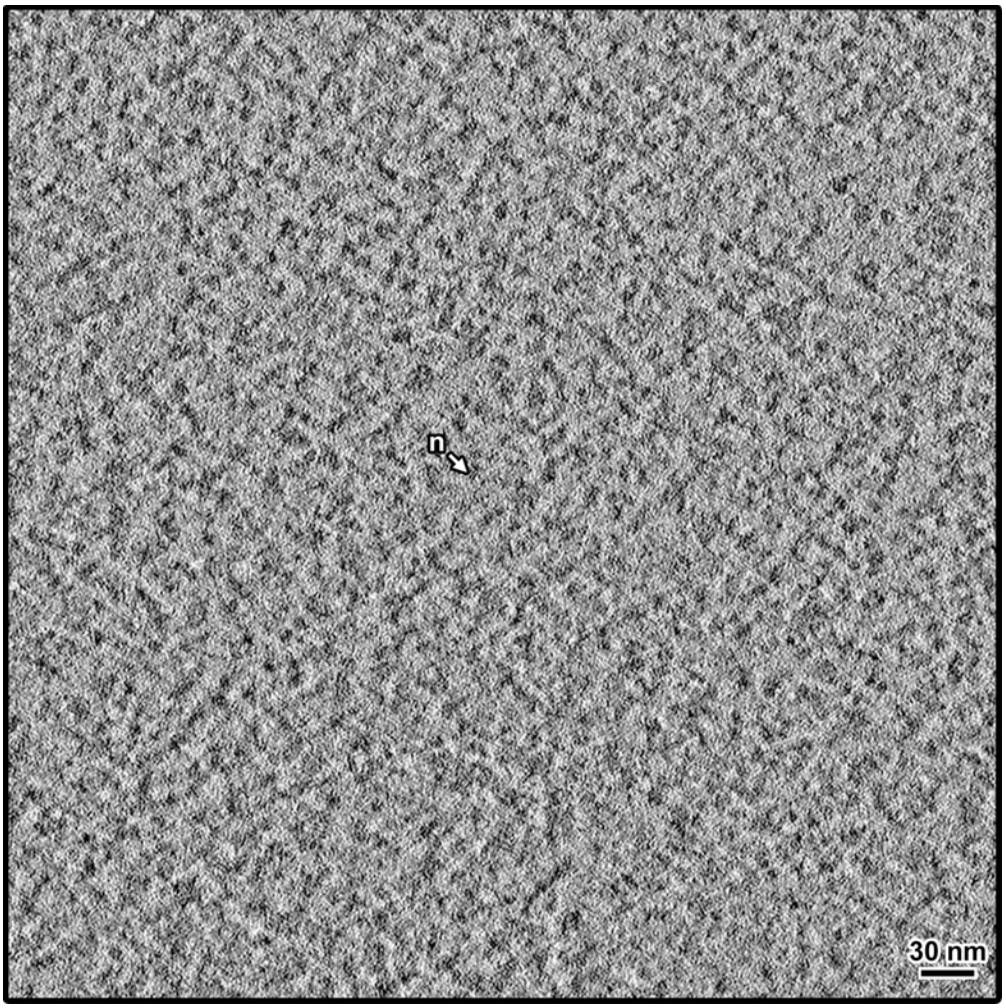

Figure S23. Twofold enlargement of selected region from TSA-G0 nucleus cryolamella

A region of a Volta cryotomographic slice (12 nm) of nucleus in a wild-type G0 cell treated with 20 ng/µL TSA during G0 entry from Figure S22, selected for Fourier power spectrum analysis in Figure 6. A nucleosome-like particle (n) is indicated.

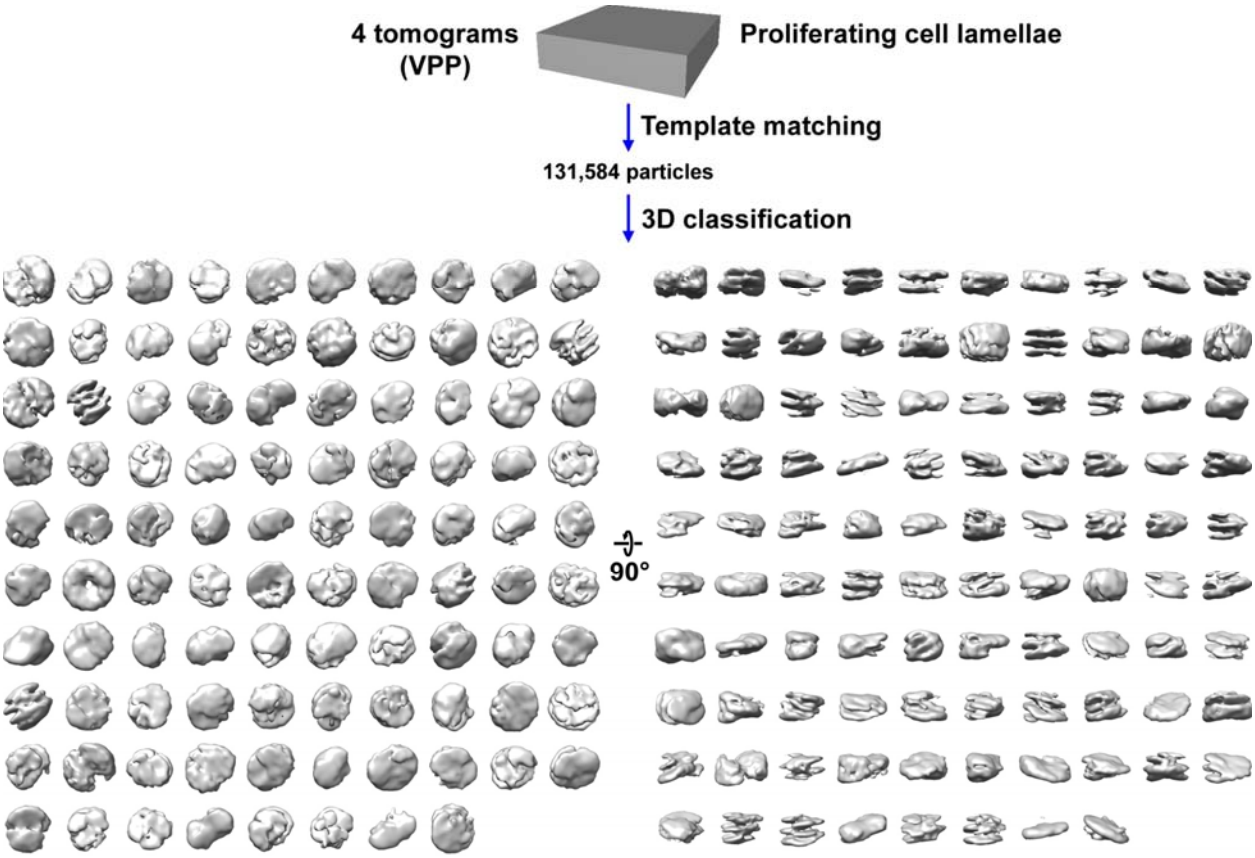

Figure S24. Direct 3-D classification of proliferating cell cryolamellae densities. Tomograms of proliferating cell cryolamellae were template matched using a smooth 5 nm radius 6 nm thick cylindrical reference and a 5.4 nm radius 6.1 nm thick cylindrical mask. Direct 3-D class averaging (2-D classification was bypassed) was done using a smooth 5 nm radius 6 nm thick cylindrical reference and a 5 nm radius 6 nm thick cylindrical mask with a cosine-shaped edge, with 100 classes. None of the class averages (grey) of the nucleosome-like template-matching hits resembled a canonical nucleosome. Two classes have no contributing particles.

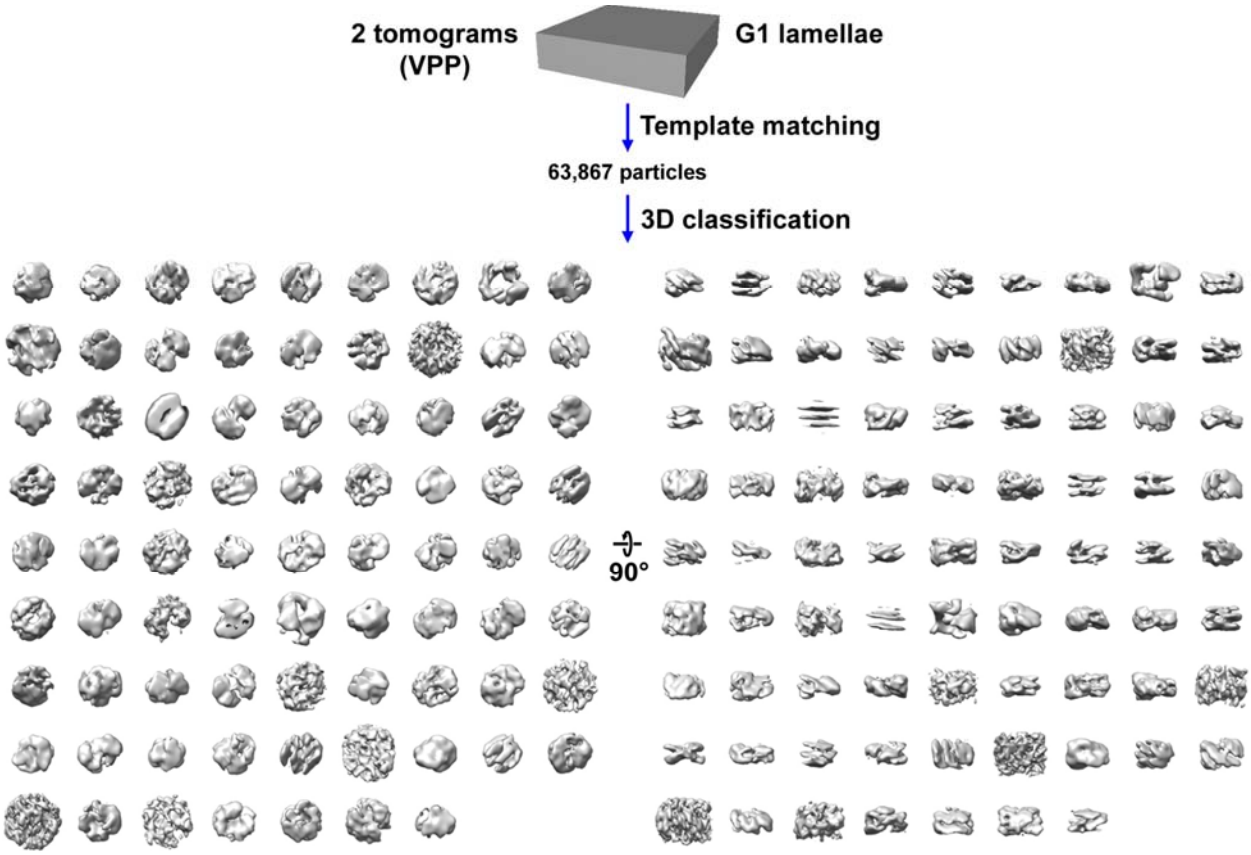

Figure S25. Direct 3-D classification of cdc10-129 G1 cryolamellae densities. Tomograms of *cdc10-129* G1 cryolamellae were template matched using a smooth 5 nm radius 6 nm thick cylindrical reference and a 5.4 nm radius 6.1 nm thick cylindrical mask. Direct 3-D class averaging (2-D classification was bypassed) was done using a smooth 5 nm radius 6 nm thick cylindrical reference and a 5 nm radius 6 nm thick cylindrical mask with a cosine-shaped edge, with 100 classes. None of the class averages (grey) of the nucleosome-like template-matching hits resembled a canonical nucleosome. Twenty-one classes have no contributing particles.

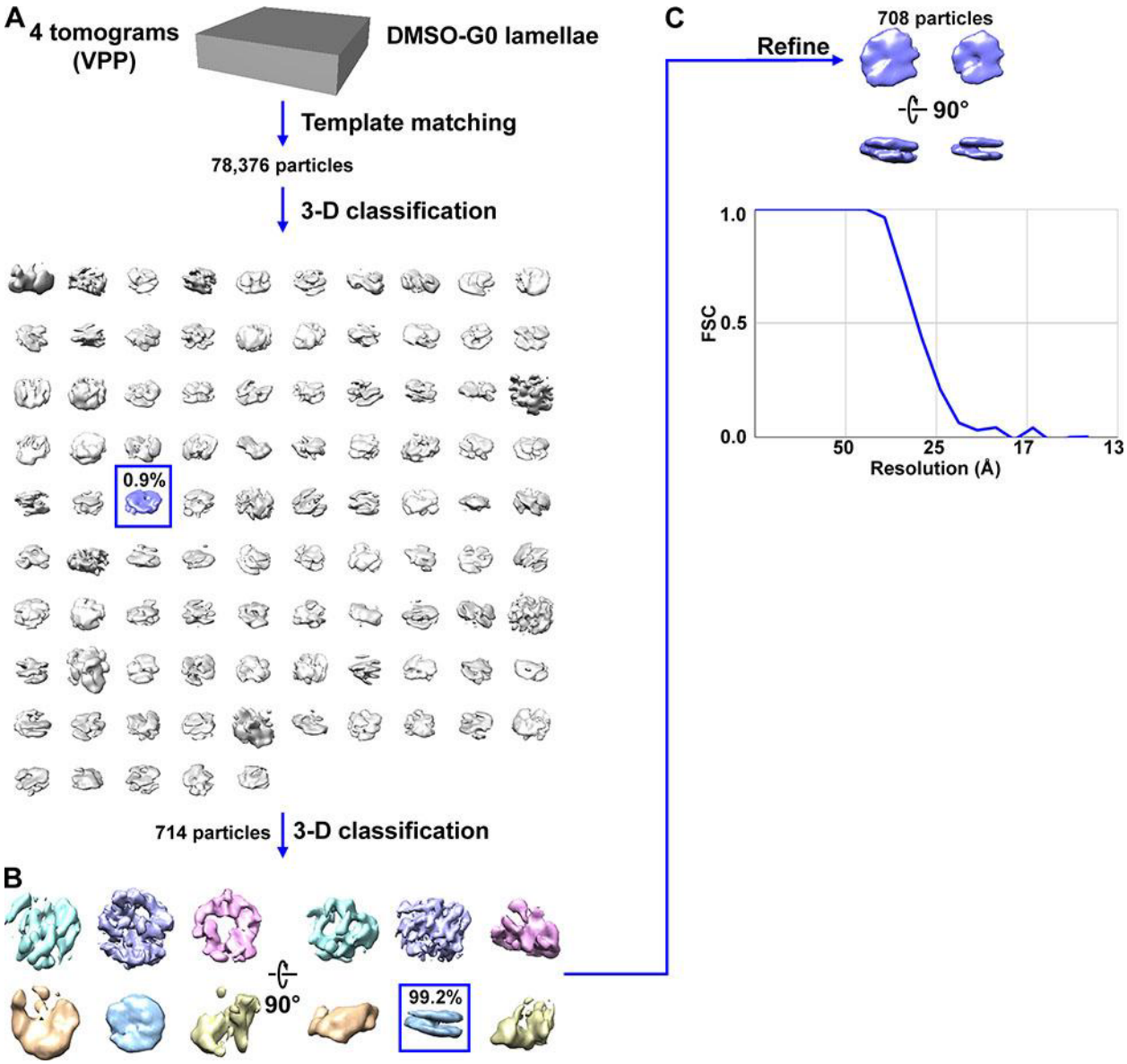

Figure S26. Direct 3-D classification of DMSO-G0 cryolamellae densities. (A) Tomograms of DMSO-G0 cryolamellae were template matched using a smooth 5 nm radius 6 nm thick cylindrical reference and a 5.4 nm radius 6.1 nm thick cylindrical mask. Direct 3-D class averaging (2-D classification was bypassed) was done using a smooth 5 nm radius 6 nm thick cylindrical reference and a 5 nm radius 6 nm thick cylindrical mask with a cosine-shaped edge, with 100 classes. The canonical nucleosome-like class average is shaded blue. Five classes have no contributing particles. (B) The second round of 3-D classification from the canonical nucleosome-like class from panel A, with 10 classes. Four classes have no contributing particles. (C) Refined density of candidate nucleosomes observed in DMSO-G0 cryolamellae. The density views on the left have a contour level of 0.25, the density views on the right have a contour level of 0.50. The resolution is ~28 Å by the FSC = 0.5 criterion.

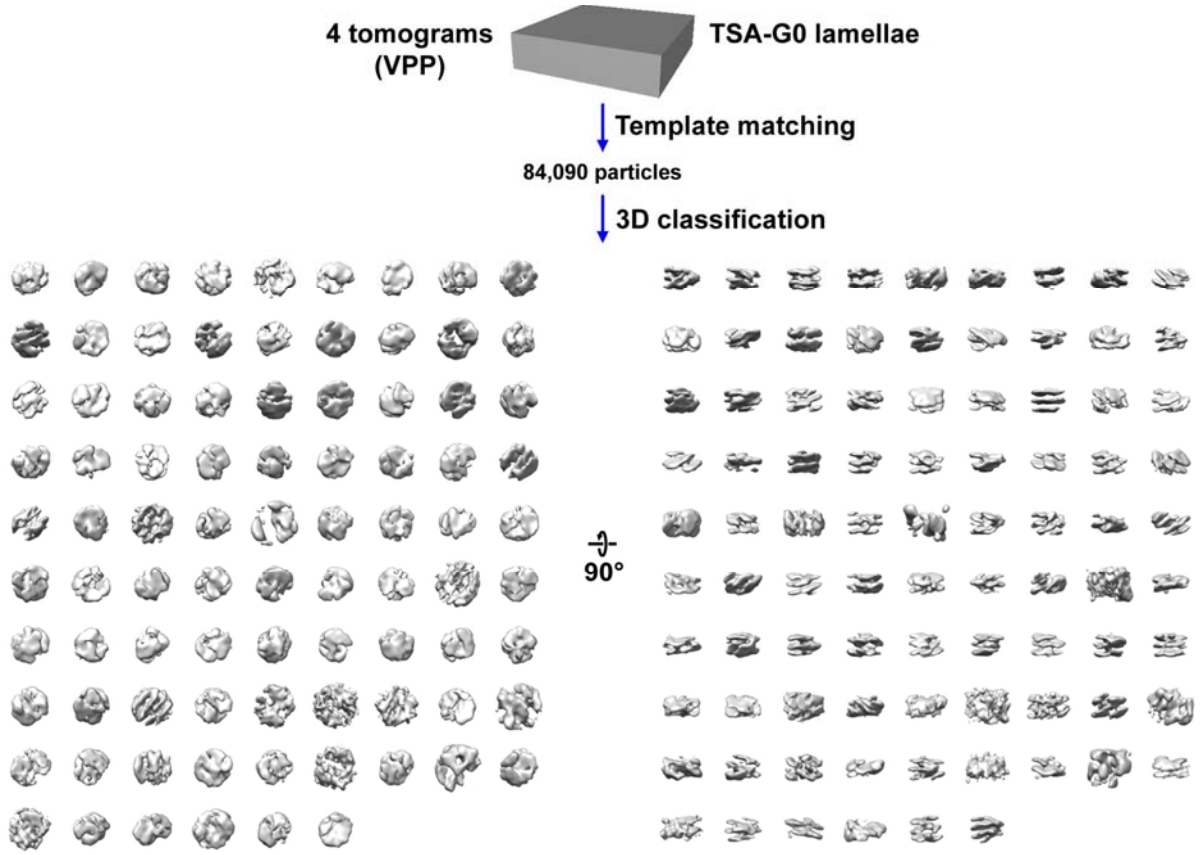

Figure S27. Direct 3-D classification of TSA-G0 cryolamellae densities.
Tomograms of TSA-G0 cryolamellae were template matched using a smooth 5 nm radius 6 nm thick cylindrical reference and a 5.4 nm radius 6.1 nm thick cylindrical mask. Direct 3-D class averaging (2-D classification was bypassed) was done using a smooth 5 nm radius 6 nm thick cylindrical reference and a 5 nm radius 6 nm thick cylindrical mask with a cosine-shaped edge, with 100 classes. None of the class averages (grey) of nucleosome-like template-matching hits resembled a canonical nucleosome. Thirteen classes have no contributing particles.

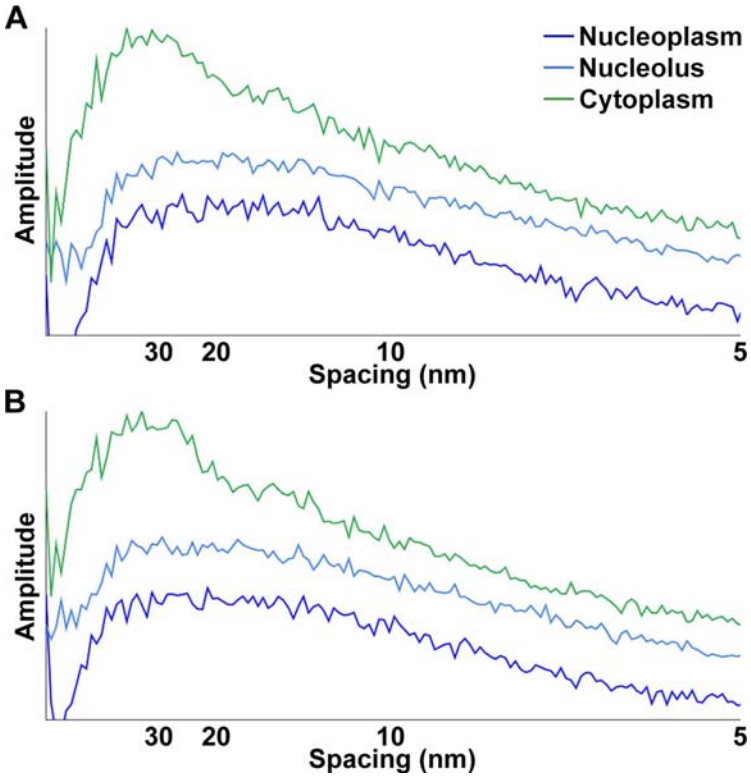

Figure S28. G0 nucleoplasm and nucleolus power spectra are similar to each other, but do not have the 30 nm peak present in the cytoplasm power spectrum. Rotationally averaged 1-D Fourier power spectra of chosen nucleoplasm (blue) and nucleolus (light blue) regions in the G0 tomogram analysed, with the Fourier power spectrum of a ribosome-rich cytoplasm region in a G1 tomogram (green) for comparison. Fourier analysis was done on Volta cryotomographic slices extracted at (A) 12 nm and (B) 30 nm thickness. All power spectra for each thickness are plotted on the same graph, separated with arbitrary offsets for clarity.

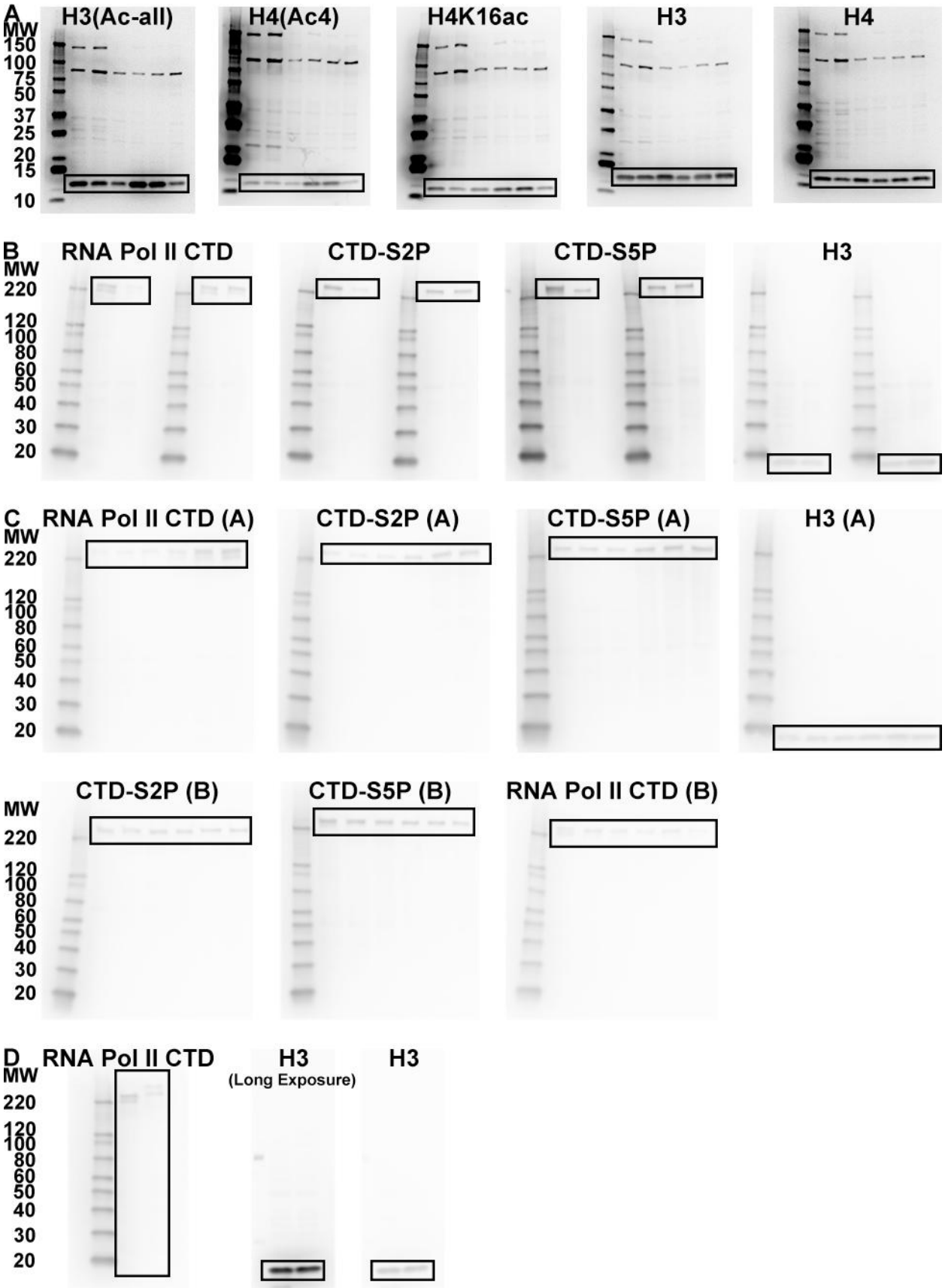

1677

Figure S29. Uncropped immunoblots.
For each immunoblot, the cropped bands are boxed at the bottom. (A) Immunoblots used in Figure 2A. The same molecular weight markers (MW, kilodaltons) were used for all 5 blots. Molecular weights are indicated to the left of the α-H3(Ac-all) blot. The detected high-molecular weight proteins (> 75 kilodaltons) are non-specifically bound by the StrepTactin-HRP conjugate. (B) Immunoblots used in Figures 3B and 3C. Molecular weight markers are different from those in part A, but the same across all 4 blots in this part. Molecular weights are indicated to the left of the α-CTD blot. For each antibody, the left set of lanes was loaded to have equal concentrations of H3, shown in Figure 3B, the right set of lanes was loaded to have equal concentrations of CTD, shown in Figure 3C. (C) Immunoblots used in Figure S4. Molecular weight markers used are the same as those used in part B. Molecular weights are indicated to the left of the α-CTD blot used in Figure S4A and the α-S2P blot used in Figure S4B. (D) Immunoblots used in Figure S1C. Molecular weight markers used for the first blot in this part are the same as those used in part B. Molecular weights are indicated to the left of the α-CTD blot. The GFP immunoblot and one of the H3 loading controls were exposed for 40 seconds during imaging. Both H3 loading controls do not have molecular weight markers. The anti-GFP blots shown in Figures S1C and S10C are already uncropped.

1696 **Table S1. Strains used in this paper**

Strain	Parent	Genotype	Source
MBY99	--	*972 h-*	MB lab
MBY165	–	*cdc10-129*	MB lab
yFS240 (tk-hENT1)	–	*h- leu1-32 ura4-D18 ade6-210 his7-366 pJL218 (his7 adh1:tk) pFS181 (leu1 adh1:hENT1)*	(Sivakumar et al., 2004)
LGSP0001	MBY99	*972 h- rpb1-eGFP-kanMX*	This paper
LGSP0002	MBY99	*972 h- nup97-eGFP-kanMX*	This paper

1697 MB lab = gift from Mohan Balasubramanian lab

1698

1699 **Table S2. Confocal microscopy details**

General	
Instrument	Olympus FV3000
Pinhole	1 Airy unit
X, Y pixel	0.0800 [µm] for DAPI + eGFP, 0.0800 [µm] for DAPI + Alexa Fluor 488, 0.0874 [µm] for eGFP only, 0.0729 [µm] for DAPI only
Z pixel	0.4100 [µm] or 0.500 [µm]
Acquisition	
Objective lens	UPLSAPO 60XO
Objective lens magnification	60×
Objective lens NA	1.35
Scan device	Galvano
Scan direction	One way
Dwell time	2.0 [µs pixel^{-1}]
Sequential mode	Line
Integration type	None
Integration count	0
Zoom	×2.59 for DAPI + eGFP, ×2.59 for DAPI + Alexa Fluor 488, ×2.37 for eGFP only, ×2.84 for DAPI only
DAPI channel settings	
Emission wavelength	461 [nm]
PMT voltage	400 – 550 [V]
C.A.	200 [µm] for DAPI + eGFP, 202 [µm] for DAPI + Alexa Fluor 488, 190 [µm] for DAPI only
Bits/pixel	12 [bits]
Laser wavelength	405 [nm]
Laser transmissivity	0.5 – 0.6 [%]
AOTF/AOM transmissivity	0.3 [%]
Laser ND filter	10 [%]
Detection wavelength	430 – 470 [nm]
eGFP channel settings	
Emission wavelength	510 [nm]
PMT voltage	550 – 750 [V]
C.A.	200 [µm] for DAPI + eGFP, 210 [µm] for eGFP only
Bits/pixel	12 [bits]
Laser wavelength	488 [nm]
Laser transmissivity	0.5 [%]
AOTF/AOM transmissivity	0.3 [%]
Laser ND filter	10 [%]
Detection wavelength	500 – 600 [nm]
Alexa Fluor 488 channel settings	
Emission wavelength	520 [nm]
PMT voltage	500 [V]
C.A.	202 [µm]
Bits/pixel	12 [bits]
Laser wavelength	499 [nm]

Laser transmissivity	0.04 – 3.5[%]
AOTF/AOM transmissivity	0.3 [%]
Laser ND filter	10 [%]
Detection wavelength	500 – 600 [nm]
DIC channel settings	
PMT voltage	205 – 320 [V]
C.A.	200 [µm] for DAPI + eGFP, 202 [µm] for DAPI + Alexa Fluor 488, 210 [µm] for eGFP only, 190 [µm] for DAPI only
Bits/pixel	12 [bits]
Laser wavelength	488 [nm] if eGFP is used, 499 [nm] if Alexa Fluor 488 is used, 405 [nm] if only DAPI is used
Laser transmissivity	0.3 – 2 [%]
AOTF/AOM transmissivity	0.3 [%]
Laser ND filter	10 [%]

1700

1701 **Table S3. Antibodies used.**

Antigen	Primary antibody	Secondary antibody	Dilution	
			primary	secondary
Immunoblots				
H3 C-terminus	ab1791 (Abcam)	7074S (CST)	1:1000	1:5000
H4 C-terminus	ab10158 (Abcam)	7074S (CST)	1:1000	1:5000
Acetyl-H3	06-599 (Merck)	7074S (CST)	1:1000	1:5000
Acetyl-H4	06-866 (Merck)	7074S (CST)	1:1000	1:5000
H4K16ac	ab109463 (Abcam)	7074S (CST)	1:1000	1:5000
Pol II-CTD	ab26721 (Abcam)	7074S (CST)	1:1000	1:5000
Pol II-CTD-S2P	ab5095 (Abcam)	7074S (CST)	1:1000	1:5000
Pol II-CTD-S5P	ab5131 (Abcam)	7074S (CST)	1:1000	1:5000
eGFP	sc9996 (Santa Cruz)	7076S (CST)	1:1000	1:5000
Immunofluorescence				
Acetyl-H3	06-599 (Merck)	A11008 (Thermo)	1:500	1:500
Acetyl-H4	06-866 (Merck)	A11008 (Thermo)	1:500	1:500
H4K16ac	ab109463 (Abcam)	A11008 (Thermo)	1:100	1:500
Pol II-CTD	ab26721 (Abcam)	A11008 (Thermo)	1:1000	1:2000
Pol II-CTD-S2P	ab5095 (Abcam)	A11008 (Thermo)	1:1000	1:2000
Pol II-CTD-S5P	ab5131 (Abcam)	A11008 (Thermo)	1:1000	1:2000
Fibrillarin	NB300-269 (Novus)	A11001 (Thermo)	1:1000	1:2000

1702 CST = Cell Signaling Technology; Thermo = Thermo Fisher Scientific.
1703

1704 **Table S4 PCR primers, 5' → 3'**

Editing	
nup97 5' HA F	ACCTTCTAGCTCAGTTGT
nup97 5' HA R	TTGGTACGACACCTGTGAATAGTTCCTCGCCTTTTGACATTGTC ATTTCTATTTCGCAGC
eGFP-KanMX F	ATGTCAAAAGGCGAGGAAC
nup97 eGFP-KanMX R	AAGTCAAGTAAACATAGAATAAACAACCTTAAAAAAATAACAGT ATAGCGACCAGCATTC
nup97 3' HA F	TTATTTTTTTAAGGTTGTTTATTCTATGTTTACTTGACT
nup97 3' HA R	ACCAAGTGTCGCTATCTCAT
rpb1 5' HA F	TGCGAGTGGAGAAAAGGAT
rpb1 5' HA R	AGTTCCTCGCCTTTTGACATAGATGGGCTAGTAGGGGAA
rpb1 eGFP-KanMX R	GCATTGTCATCTTCACACAACTAGCAGTATAGCGACCAGCATT C
rpb1 3' HA F	CTAGTTGTGTGAAGATGACAATG
rpb1 3' HA R	GCGTTAGTATCGAATCGACAGAAATTTAATTACTACAGACATTT GGTTTT
pFA F	CTGTCGATTCGATACTAACG
rpb1 pFA R	CATCCTTTTCTCCACTCGCATCTATAGTGTCACCTAAATCGTAT
Confirmation	
FN	TGCTTTGTGGTCTTTACGAG
RN	AGGACCTTTGGAGCCTTTTA
RG	ATAAGTTGCGTCCCCTTCA
FK	CCTTATTTTTGACGAGGGGA
5' rpb1-EGFP Validation Primer F	TCTTATTCCCCTACTAGTCCC
5' rpb1-EGFP Validation Primer R	ATAAGTTGCGTCCCCTTCA
3' rpb1-KanMX Validation Primer F	TCTTGTTTTCAAGAACTTGTCATT
3' rpb1-KanMX Validation Primer R	AACGCACAAACCAAACTAC
3' rpb1-BB Validation Primer F	CCGGTACTTGTAGTGATTGG
3' rpb1-BB Validation Primer R	ACGACTCACTATAGGGAGACC
5' rpb1-BB Validation Primer F	GGCTACAATTAATACATAACCTTATGT
5' rpb1-BB Validation Primer R	TCAGATATTCCCTTGCAATCAT
FR	TTTTGGAAACAGACGGCATA
RR	GGAGCATTATAGGTCGGGTA
Sequencing	
FA1	CGGTGGTAAAGGTGGTAAAG
RA1	TCGTTTCTGATAAACCAGGT
RG	CCGTTTCATATGATCTGGGT
Histone-GFP Seq R1.2	CTGACCTACAGGAAAGAGTT
Histone-GFP Seq F2.1	CTGTCCTTTTACCAGACAAC
Histone-GFP Seq F2.2	CTCTTATTGACCACACCTCT
Histone-GFP Seq R2.2	CTTCTTTGCAGGAAGAATCG
Histone-GFP Seq F3.1	TCACATCACATCCGAACATA
FH	GACCATTTGCTGTAATCGAC
RA2.2	CTGGACGAAGACGAAGTAAT
HAB2Del Seq R1	ATTACCCTGTTATCCCTAGC
HAB2Del Seq R2	CAGGAGTACGGATAAAATGC
HAB2Del Seq R3	TATCGAATCGACAGCAGTAT

RK	CCTTATTTTTGACGAGGGGA
RB2	ATTAACCGGGATTCACTGAC
FB1	ATGTCTGCTAAAGCCGAAAA
RB1	AGTCAGCGACATCTGTCTTT
FT1	AAGCAAACAGCAAGAAAGTC
RT1	CTTCTGACAGCAAGGGTATT
FF1	ATGTCCGGTAGAGGTAAAGG
RF1	ACACACGAAAATCCTGTGAT

1705

1706 **Table S5. Lamella Cryo-EM imaging and analysis details.**

EM grids	Quantifoil® R2/2
FIB-milling dual-beam microscope	Helios NanoLab 600 DualBeam
TEM imaging microscope	Titan Krios
Energy	300 keV
Camera: recording mode	K3: super-resolution
Tomography software	SerialEM
Calibrated pixel sizes, unbinned	3.4 Å
Defocus (nominal)	−0.5 or −1 µm
Cumulative dose	120 or 200 e^{-} $Å^{-2}$
Dose fractionation	(1/cosine)^(1/4)
Tilt range: scheme	−70° to +50°, dose symmetric
Tilt increment	2°
Tomogram processing & visualisation	IMOD 4.11
Template matching	PEET 1.15.1
Subtomogram classification & averaging	RELION 3.0.8
Analysis scripts	https://github.com/anaphaze/ot-tools
Figure creation and editing; t-tests	Adobe Photoshop and Illustrator; Google sheets

1707

Table S6. Cryotomogram details.

Tomogram	Strain	State	Fig	Dose (e/Å^2)	Pixel size (Å)	Δf (µm)	Δtilt (°)	VPP	Thick (nm)	Rsd (nm)	Analysis
20230418_006	*972h-*	P		120	3.4	0	2	+	170	0.72	FPS
20230418_007	*972h-*	P	S17, S18	120	3.4	0	2	+	220-290	0.81	FPS
20230418_016	*972h-*	P		120	3.4	0	2	+	205-250	0.72	FPS
20230605_018	*972h-*	P		200	3.4	0	2	+	120	0.53	STA
20230605_021	*972h-*	P		200	3.4	0	2	+	95	0.65	STA
20230605_023	*972h-*	P		200	3.4	0	2	+	160	0.40	STA
20230605_028	*972h-*	P		200	3.4	0	2	+	140	0.60	STA
20220718_ Defocus_009	*cdc10-129*	G1	S13	120	3.4	10-13	2	−	150	0.62	-
20220718_017	*cdc10-129*	G1		120	3.4	0	2	+	110	0.45	FPS
20221019_062	*cdc10-129*	G1		120	3.4	0	2	+	120	0.26	FPS
20221216_020	*cdc10-129*	G1		120	3.4	0	2	+	120	0.42	FPS
20221216_027	*cdc10-129*	G1		120	3.4	0	2	+	165	0.67	FPS
20230125_045	*cdc10-129*	G1	S14	120	3.4	0	2	+	160	0.83	FPS
20230125_050	*cdc10-129*	G1	4, S15, S16	120	3.4	0	2	+	110-175	0.49	STA, FPS
20230125_059	*cdc10-129*	G1		120	3.4	0	2	+	135	0.73	FPS
20230125_063	*cdc10-129*	G1	8	120	3.4	0	2	+	160	0.69	STA, FPS
20220608_ batch32_ts_002	*972h-*	G0	S13	120	3.4	8-9	2	−	135	0.68	-
20221015_048	*972h-*	G0		120	3.4	0	2	+	115	0.83	FPS
20221019_010	*972h-*	G0		120	3.4	0	2	+	155	0.43	FPS
20221019_029	*972h-*	G0		120	3.4	0	2	+	135	0.43	STA, FPS
20230125_003	*972h-*	G0		120	3.4	0	2	+	150-200	0.91	FPS
20230125_015	*972h-*	G0		120	3.4	0	2	+	160	0.75	FPS
20230125_017	*972h-*	G0		120	3.4	0	2	+	135	0.64	STA, FPS
20230125_019	*972h-*	G0		120	3.4	0	2	+	140-185	0.98	FPS
20230125_028	*972h-*	G0	4, 8, S19, S20, S21	120	3.4	0	2	+	135-205	0.58	STA, FPS
20230125_033	*972h-*	G0		120	3.4	0	2	+	145	0.87	FPS
20230125_037	*972h-*	G0		120	3.4	0	2	+	100-130	0.70	STA, FPS
20230106_018	*972h-*	TSA-G0		120	3.4	0	2	+	95-155	0.79	STA, FPS
20230106_019	*972h-*	TSA-G0		120	3.4	0	2	+	145-180	0.98	STA, FPS
20230106_020	*972h-*	TSA-G0		120	3.4	0	2	+	145	0.58	STA, FPS
20230106_022	*972h-*	TSA-G0		120	3.4	0	2	+	140-190	0.87	FPS
20230106_025	*972h-*	TSA-G0	4, S22, S23	120	3.4	0	2	+	140-160	0.56	STA, FPS
20230106_032	*972h-*	TSA-G0		120	3.4	0	2	+	170-205	0.85	FPS
20230106_033	*972h-*	TSA-G0		120	3.4	0	2	+	185	0.45	FPS

P = unsynchronised proliferating. G1 = G1 phase. G0 = G0 after a 24-hour incubation in EMM−N media. TSA-G0 = 24 hour incubation in EMM−N plus 2 µg mL^{-1} TSA. Δf: Nominal defocus used for VPP data; refined defocus used for defocus data. VPP = Volta phase plate was used (+) or not used (-). Thick = lamellae thickness – some

lamellae had a wedge-like profile and therefore a range of thicknesses. Rsd = alignment residual. For “Analysis”, STA = used for subtomogram classification and averaging, FPS = used for Fourier power spectrum analysis. The raw cryo-ET data and a tomogram of each dataset here was deposited in EMPIAR.

SUPPLEMENTAL REFERENCES

Ho, J., Tumkaya, T., Aryal, S., Choi, H. and Claridge-Chang, A. (2019). Moving beyond P values: data analysis with estimation graphics. *Nat Methods* **16**, 565-566. doi:10.1038/s41592-019-0470-3

Sivakumar, S., Porter-Goff, M., Patel, P. K., Benoit, K. and Rhind, N. (2004). In vivo labeling of fission yeast DNA with thymidine and thymidine analogs. *Methods* **33**, 213-9. doi:10.1016/j.ymeth.2003.11.016

White, C. L., Suto, R. K. and Luger, K. (2001). Structure of the yeast nucleosome core particle reveals fundamental changes in internucleosome interactions. *EMBO J* **20**, 5207-18. doi:10.1093/emboj/20.18.5207